Development of a Simulation based Powertrain Design Framework for Evaluation of Transient Soot Emissions from Diesel Engine Vehicles

by

Rahul Ahlawat

A dissertation submitted in partial fulfillment
of the requirements for the degree of
Doctor of Philosophy
(Mechanical Engineering)
in The University of Michigan
2011

Doctoral Committee:

Professor Jeffrey L. Stein, Co-Chair
Assistant Professor Hosam K. Fathy, Co-Chair, Penn State University
Research Professor Zoran S. Filipi
Research Professor Timothy J. Gordon
Professor Jessy W. Grizzle

To my parents

ACKNOWLEDGEMENTS

This dissertation was made possible due to the support, guidance, and encouragement from many people. First of all, I would like to thank Prof. Jeffrey Stein for giving me to opportunity to join his research group, and his guidance and endless support for all these years. I am also extremely grateful to Prof. Hosam Fathy for his mentorship, patience and teaching me how to become a better researcher. I would also like to thank my committee members, Prof. Zoran Filipi, Prof. Tim Gordon and Prof. Jessy Grizzle, for their time and numerous helpful comments and suggestions at various stages of this dissertation.

I would also like to acknowledge the funding agencies that supported my work over the years. These include the Automotive Research Center (ARC), Automated Modeling Lab (AML), Department of Mechanical Engineering, BorgWarner Inc., and A&D Technology. I would also like to thank the current and former members of the AML: Scott Moura, Joel Forman, Ben Pence, Tulga Ersal and Burit Kittirungsi for their advice, support, constructive criticism and friendship. Special thanks to Scott Moura for being a great friend; I will always cherish the time we spent together at Michigan and traveling around the world! The EIL experiments used in this dissertation were conducted in the Auto Lab, and were made possible due to the hard work of a number of individuals including Jonathan Hagena, Ashwin Salvi and Rajit Johri. I would like to thank Rajit Johri for sharing numerous learning experiences over the last eleven years, and the friendship we have fostered since the days of Mini Baja.

My time here in Ann Arbor has been nothing short of extraordinary, not only due to the number of things that I've learned but also because of the number of outstanding people I've met. From almost a religious patronage towards Michigan football to 3am runs to BTB, to the weekly convocations at the Den, these times will always be missed. Though it is impossible to name everyone individually, some of the people deserve a special mention. I would like to thank Awlok Josan for being a true friend and being there for me when I needed help. The time we have spent together as roommates, especially at 115 Adams, will always be remembered. I would also like to express my sincere gratitude towards my friends Danese Joiner, Sidharth Misra, Stefano Di Cairano, Sharath Bachegowda, Kim Khalsa, Laura Brown, Christine Eun, Arnau Tibau, Sean and Nancy McGrogan, Emine Cagin, Tzeno Galchev, Philip Aumüllner, Giulio Ripaccioli, Carmelo Speltino and Raj Pandravada for sharing many wonderful moments with me during these past years. I would also like to thank Dan Lingenfelter for being an exceptional roommate, and taking care of the chores in our house while this document was being written. Also, special kudos to Kim, Dan, Christine and Scott for proof-reading this dissertation without much of a notice.

Finally, I would like to thank my family, my parents Rajender and Manju, and my brother Rohit, for their unconditional love and support that made it possible for me to achieve my educational goals.

TABLE OF CONTENTS

LIST OF FIGURES

Figure

LIST OF TABLES

Table

LIST OF APPENDICES

Appendix

ABSTRACT

Development of a Simulation based Powertrain Design Framework for Evaluation of Transient Soot Emissions from Diesel Engine Vehicles

by

Rahul Ahlawat

Co-Chairs: Jeffrey L. Stein and Hosam K. Fathy

This dissertation presents the development of a modeling and simulation framework for diesel engine vehicles to enable soot emissions as a constraint in powertrain design and control. To this end, numerically efficient models for predicting temporally-resolved transient soot emissions are identified in the form of a third-order dual-input single-output (DISO) Volterra series from transient soot data recorded by integrating real-time (RT) vehicle level models in Engine-in-the-loop (EIL) experiments. It is shown that the prediction accuracy of transient soot significantly improves over the steady-state maps, while the model remains computationally efficient for systems-level work.

The evaluation of powertrain design also requires a systematic procedure for dealing with the issue that drivers potentially adapt their driving styles to a given design. In order to evaluate the implications of different powertrain design changes on transient soot production it is essential to compare these design changes on a consistent basis. This problem is explored in the context of longitudinal motion of a vehicle following a

standard drive-cycle repeatedly. This dissertation develops a proportional-derivative (PD) type iterative learning based algorithm to synthesize driver actuator inputs that seek to minimize soot emissions using the Volterra series based transient soot models. The solution is compared to the one obtained using linear programming. Results show that about 19% reduction in total soot can be achieved for the powertrain design considered in about 40 iterations.

The two contributions of this dissertation: development of computationally efficient system level transient soot models and the synthesis of driver inputs via iterative learning for reducing soot, both contribute to improving the art of modeling and simulation for diesel powertrain design and control.

CHAPTER I

Introduction

> "The exhaust from diesel engines ... has a characteristic pungent and disagreeable smell. I cannot believe that the police will allow any large proportion of diesel-engined vehicles in the streets of, say, London" - Sir Harry Ricardo, 1925[1]

Diesel engines are the preferred prime mover in medium duty vehicles due to their superior fuel economy, favorable low end torque rating, and durability [2]. While the lower fuel consumption, as compared to gasoline engines, is attributed to the overall lean combustion and a better energy release efficiency [3], diesel combustion is not homogenous in nature with parts of the combustion taking place in zones that are oxygen deficient. The complex processes involved, such as turbulent mixing, three-dimensional heterogeneity, and unsteadiness, coupled with the presence of high temperature and high pressure rich zones, lead to conditions that are favorable to the formation of regulated emissions: oxides of nitrogen (NOx) and particulate matter (PM) [4]. Particulate matter has a damaging effect on human health and, along with NOx, is one of the greatest control challenges for diesel engine vehicle emissions.

This dissertation presents the development of a modeling and simulation framework

[1]The smell was attributed to the presence of aldehydes. Quote adapted from [1]

for diesel engine vehicles to enable soot emissions as a constraint in powertrain design and control. The two original contributions of this dissertation are the development of a low-order control-oriented transient soot model capable of predicting temporally resolved transient soot emissions from the exhaust manifold of the vehicle and the synthesis of driver inputs via iterative learning to eliminate the variability in soot evaluation due to differences in driving styles. These tools provide a consistent basis to evaluate the impact of changes in powertrain design and control on transient soot. Such powertrain design and control changes include, but are not limited to, transmission shift quality control, developing supervisory controllers and power management techniques for diesel hybrids, and the sizing of diesel particulate filters (DPF). In this context, a generalized model of powershift transmissions for Engine-in-the-loop (EIL) experiments is also developed and incorporated into this powertrain design framework. Experiments to collect the transient soot data and other vehicle level models enabling this evaluation are also discussed.

1.1 Particulate Emissions from Diesel Engines

Diesel exhaust consists of hundreds of gas-phase, semi-volatile, and particle-phase organic compounds that are produced during combustion [5]. Diesel particulates are defined by the US Environmental Protection Agency (EPA) as "all compounds collected on a pre-conditioned filter in diluted diesel exhaust gases at a maximum temperature of 325 K (125F)", with the exception of condensed water. 'Smoke', on the other hand, is the visible component of particulate matter, denoting an aerosol i.e. suspension of particles in a gas [6]. Thus, particulate matter is a much broader term than smoke. The formation of these particles exhibit dual modes, namely 'nucleation mode' and 'accumulation mode'. While the details of the chemical processes behind the formation of these modes is beyond the scope of this work, some relevant background is presented in Appendix *A*.

The PM collected on a filter is usually separated with an extraction solvent into two fractions [7, 8]. One fraction is a solid carbon material (soot) that cannot be dissolved by an organic solution. It is harmful for human health and influences atmospheric visibility. The other fraction can be dissolved by an organic solution and is called the soluble organic fraction (SOF). This fraction has been adsorbed into the soot or condensed onto the filter, and it is composed of unburned fuel and lubricating oil and their thermally synthesized components [8, 9].

Although particulate matter encompasses both soot and SOF, the terms PM and soot are used interchangeably in this work. The work is intended for evaluating time-resolved mass fraction of particulates as seen out of the exhaust manifold, and not cycle-resolved constituents in the cylinder. Soot constitutes the bulk of the mass of particulates in the exhaust manifold, and experiments done at various speed and load points by Hagena et al. [10] showed that below smoke numbers of around 1.5, which corresponds to a concentration level of 32.4 mg/m^3, soot and PM masses closely agree with each other.

1.1.1 Health and Environmental Effects

Diesel particulate emissions have long proven to have deteriorating health and environmental effects. In outdoor air, diesel particulates contribute to the total concentration of total suspended particulates (TSP). These particles have diameters of the order of 100 nm and are small enough to be inhaled deep into the lungs. When they penetrate the respiratory tract of the human or animal lung, they are deposited in the pulmonary region and result in an inflammatory reaction or can act as carcinogens [5, 11, 12]. A statistical relationship also exists between exposure to diesel exhaust gases and particulates and a tendency towards lung disorders and a higher

daily mortality [9]. In addition to lung disorders they also contribute to bladder cancer [9], cardiovascular diseases such as cardiac arrhythmia, atherogenesis and myocardial infarction [11].

In addition to negative health effects, diesel particulates contribute to soiling, material damage (due to chemical and polluting effects), reduced visibility, and they disturb the radiative balance affecting the climate [9, 11]. Diesel particulates are often identified as 'black smoke' in environmental studies due to their light absorption properties and are universally considered unpleasant and unacceptable.

1.1.2 Legislation

Federal certification standards for smoke opacity levels from on-road heavy-duty vehicles commenced in 1970 in the US. The first diesel particulate standards in the world to cover passenger cars and light-duty trucks were also established in the US in 1980 and were extended to heavy duty engines in 1985. PM is now regulated in most countries and the mass emitted by both light duty (g/km) and heavy duty (g/kWh) diesel engines has decreased by more than two orders of magnitude since the 1970s. Current legislative practices extend to both smoke and particulates, and compliance is necessary during both steady-state and transient operation [5, 6, 13]. A comparison of US and EU standards is presented in Table. 1.1. Although the current standards in both the US and EU are focused on reducing the mass of the particulates (TSP), increasing regulations are also being placed to regulate particulate sizes (PM_{10} and $PM_{2.5}$) [14].

In order to meet the newest regulations for PM, most vehicles will require the use of an exhaust stream diesel particulate filter (DPF). A DPF mechanically removes the particles from the exhaust stream with efficiencies of approximately 97% by mass,

Table 1.1: Comparison of PM Emission Standards [11]

	Passenger Vehicles		**Heavy Duty**	
	PM (mg/km)	Year	PM (g/kWh)	Year
US 2007	6[1]	2007	0.01	2007
US 2010			0.01	2010
Euro 4	25	2005	0.02	2005
Euro 5	5	2009	0.02[2]	2008
Euro 6	5	2014	0.01[2]	2013

and up to 99.9% by particle number [11]. Its use, however, increases back-pressure, resulting in decreased fuel-economy. Eventually the DPF becomes laden with particles and must be regenerated by oxidizing the particles. The surface oxidation of soot in a non-catalyzed DPF requires high temperatures that are not seen during regular passenger car operation. In order to increase the exhaust gas temperature, additional fuel is injected late in the combustion process, and this further results in additional increase in fuel consumption [11, 15]. Also, from the engine combustion standpoint, the improvement in soot comes with an increase in NOx emissions [4, 7, 13]. Therefore, meeting the increasing stringent PM emission regulation without penalizing fuel economy or NOx, is an extremely challenging task.

1.1.3 Motivation for Evaluating Transient Soot from Vehicles

Soot emissions from vehicles have a profound negative impact on health and the environment and hence are regulated. These emissions have also been a concern for military trucks as they serve as sources of thermal and visual signatures in the battlefield, compromising vehicles' safety [2]. Regulation testing, and more importantly, real-world driving, takes place at transient loads. Transient operation involves frequent and sudden changes in engine speed and torque and is characterized by a

[1] Fleet average value

[2] Particle size also regulated

transition between operating states such that quantities of in-cylinder components (air/fuel, exhaust gas recirculation (EGR), residual gas fraction (RGF)) and their mixing processes are not well-controlled [4]. The periods during power outtake increases, such as accelerations, result in a lower air/fuel ratio than the corresponding steady-state value. This decrease is due to turbocharger inertia, thus causing increased soot emissions due to the impaired conditions for oxidation. During these periods, peak values of transient soot emissions can be more than ten times higher than the corresponding steady state values [10, 16, 17]. Moreover, with the advent of diesel hybrid vehicles, engines might be subjected to new transient loads that have not been seen in conventional diesel vehicles, and estimating transient soot accurately in an offline setting is becoming critical for design and development of such systems.

Thus, there exists a need for a methodology to quantify and evaluate these emissions from diesel vehicles. Such tools would enable powertrain supervisory control development and the design of power management strategies for diesel hybrids to account for soot emissions. Accurate estimation would also serve in minimizing the DPF loading and regeneration frequency, thus indirectly reducing the fuel consumption penalty associated with a DPF [18]. Finally, since particle formation during transient operation is not very well understood, due to the complicated physical processes behind soot formation [4, 8], and the dependence on powertrain management, engine subsystems and drive cycle [4], evaluation techniques will provide some insight into these relationships, as least in a statistical sense.

1.2 Evaluation Methodologies for Transient Soot

In order to evaluate soot production over a transient cycle such as the Federal Test Procedure (FTP), one of the three methodologies is commonly adopted:

1. Testing the actual vehicle on a chassis dynamometer

2. Engine-in-the-loop (EIL) experiments

3. Vehicle simulations with transient soot model

The advantages of using an instrumented real-vehicle for testing are that it faces real transient loads and the actual transient soot values are recorded. However, the vehicles are typically only equipped with instrumentation to record tailpipe emission, vehicle motion, driver input and sometimes engine speed. Usually, little information is collected regarding engine operation and the reasons behind observed trends are often inconclusive. If the testing is done by the Environmental Protection Agency (EPA), then the exhaust is passed through a dilution tunnel and soot is recorded on filter paper, thus temporal resolution of soot emissions is not available. Engine-in-the-loop experiments bridge this gap by allowing controlled repeatable tests in a laboratory setting. The experiments are done with a real engine driven by a fast response dynamometer, where the dynamometer is controlled to emulate transient loads as seen in a vehicle. This setting allows complete control over the engine system and is a valuable tool for research and development, though these gains come with a much higher cost of the test cell. It is important to point out that both these approaches require instrumentation to measure vehicle transient soot emissions with high temporal resolution. Commercially available instruments capable of transient soot measurements with sufficient temporal resolution include the differential mobility spectrometer (DMS) [19], cascade impactor operating principle [20, 21], and photo-acoustic soot sensor (PASS) [22]. The latter provides only the mass concentration of the soot, while the former twocan also be used to obtain particle size information [11].

The third way of evaluating transient soot is through offline simulation of vehicle models equipped with a transient soot model. The advantages of this approach are that there is no direct cost associated with conducting the experiments and it allows the user to perform fast offline evaluations as well as enable control systems design.

The major challenge in enabling this approach is that reliable control oriented models of transient soot do not exist in the literature. This work uses EIL experiments to collect the transient soot data and then makes a new contribution by developing a control oriented transient soot model to enable soot evaluation during powertrain design and control.

1.3 Background Research

The foundation of this research is based on the EIL experiments conducted by Filipi et al. [2, 10, 23]. The block diagram of the EIL setup used is shown in Figure 1.1. Driver, transmission, and vehicle models are simulated on a real-time (RT) platform and used to control an AC dynamometer coupled to a 6.0L V-8 direct-injection diesel engine. These models accurately capture the desired dynamics while being numerically efficient to run in real-time [24]. The vehicle level models are forward-looking, hence the driver model issues throttle (α) and brake commands (β) to follow the vehicle velocity on the FTP-75 city cycle. Model causality is selected such that the torque converter model commands speed to the engine, as speed is easier to control than engine torque. The measured engine torque is fed to the torque-converter model to enable closed-loop drive-cycle simulation. The transient soot data are recorded using a differential mobility spectrometer (DMS). Complete details of the EIL setup and RT model are presented in Appendices B and C, respectively.

The vehicle was driven on the FTP-75 cycle using a proportional-integral-derivative (PID) controller based driver model. The vehicle speed trace (for the first 400sec) during the test run is shown in Figure 1.2 and the recorded transient soot for the FTP cycle is shown in Figure 1.3. It can be seen that the vehicle was able to closely follow the drive-cycle. The transient soot data shows numerous spikes associated with acceleration commands. In order to compare the transient soot performance, a

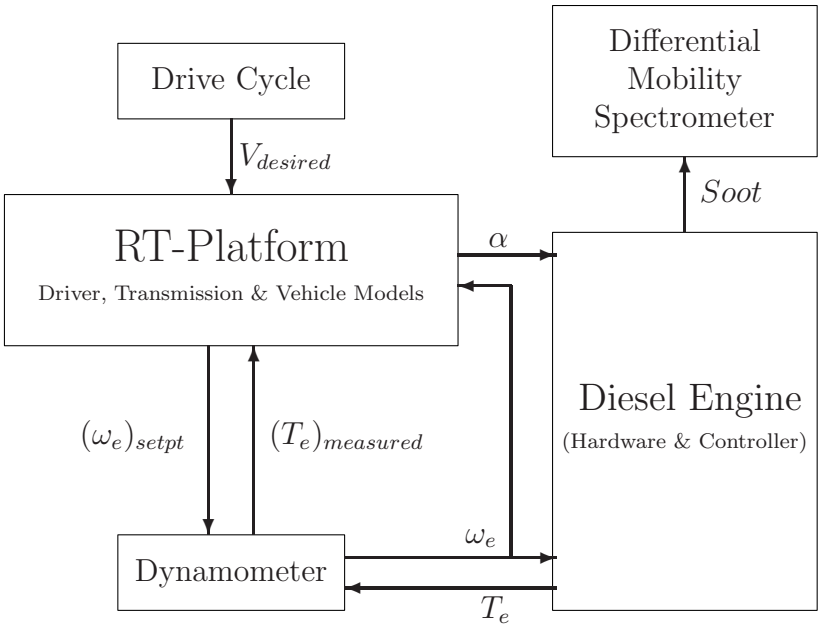

Figure 1.1: Experimental Setup for EIL Testing

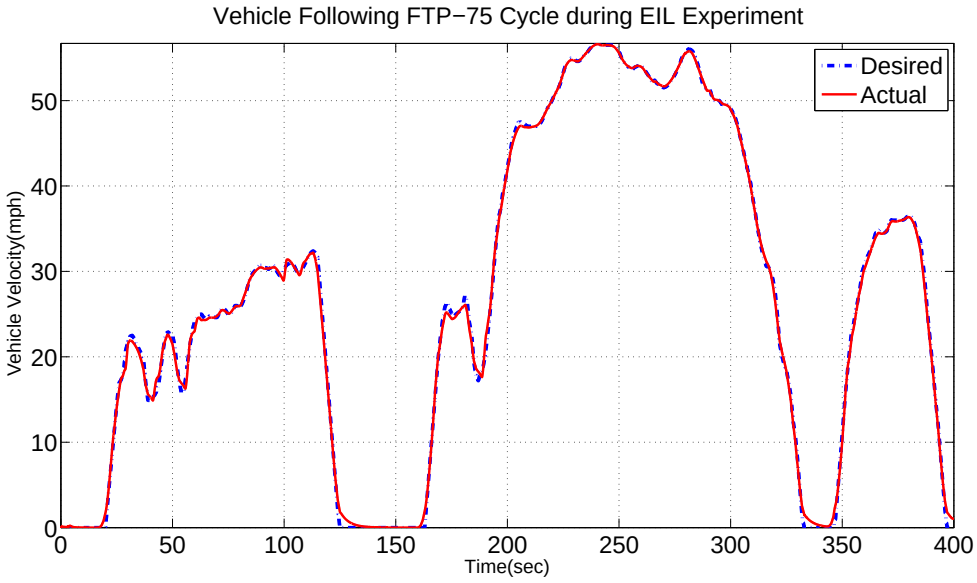

Figure 1.2: Vehicle following the prescribed drive cycle

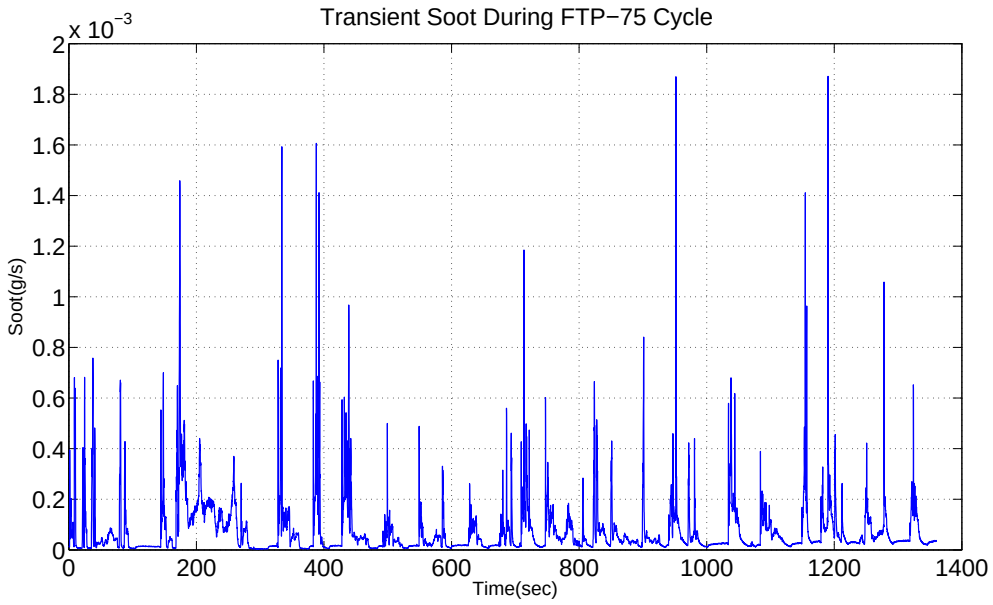

Figure 1.3: Transient soot for the FTP-75 cycle

steady-state soot map was developed by testing the engine under constant load and speed. This map was then used to predict soot for the recorded engine speed and fuel flow rate, and the interpolated values are referred to as quasi-steady-state (QSS) estimates. Figure 1.4 shows the transient soot and QSS estimates for a portion of the FTP cycle, along with the boost pressure and driver throttle command. These experimental results elucidate the two key underlying ideas of this work:

1. Quasi-steady state predictions of transient soot are unable to account for the soot spikes during the cycle. Transient engine operation accounts for 53% of the cumulative soot produced during this cycle [4], and hence represents a significant percentage of engine operation. Therefore, there is a need for transient soot models for systems-level work capable of predicting this effect.

2. The soot spikes are aligned with driver throttle commands, while the boost pressure lags behind due to turbocharger inertia. This is largely due to a greater volume of fuel being injected into the cylinder to create more torque when the driver presses the accelerator pedal, but the extra volume of air entering the

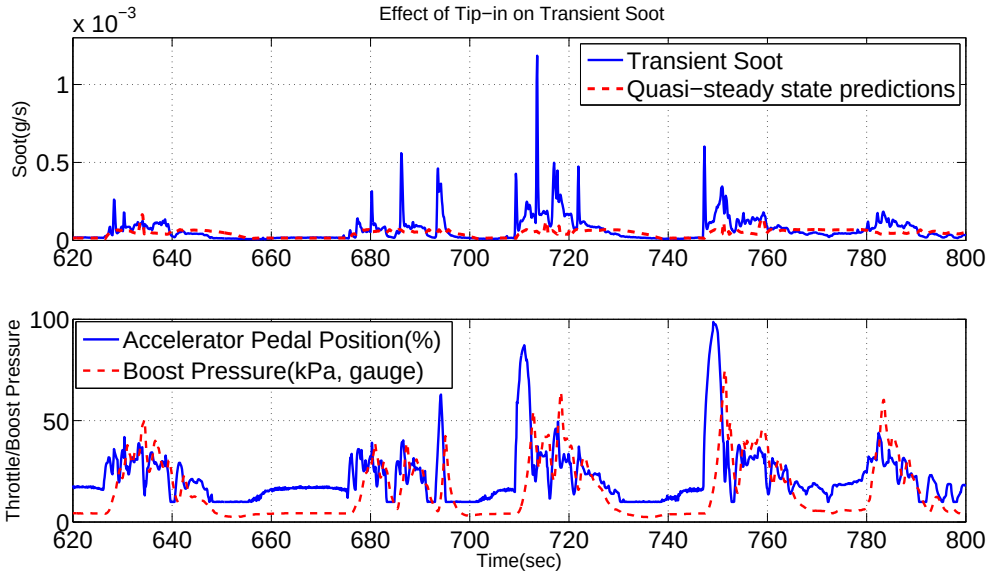

Figure 1.4: Transient soot variation during accelerations

cylinder is delayed due to turbo-lag, reducing the in-cylinder air-fuel ratios and creating soot spikes. Also when different hybrid configurations optimized only for fuel economy were tested on the same engine, better fuel economy results were obtained but the particulate emissions increased 141% and 247% for rule-based and stochastic dynamic programming (SDP) based parallel electric hybrids, respectively [2]. This was attributed to the power management strategy causing greater transient loads on the engine, and operating it more aggressively (high rate of power demand). In conventional vehicles, aggressive driving was also found to increase particulate production by a factor of two when compared to non-aggressive driving [4, 23, 25]. This indicates that the soot produced is a strong function of driving style. Due to this strong driver-vehicle interaction, it is difficult to attribute the soot performance solely to the powertrain. Thus, there exists a need to assess the soot performance on the transient cycle while decoupled from the driver.

1.4 Objectives

This work intends to develop a modeling and simulation framework for diesel engine vehicles to include soot emissions in powertrain design and control. Such a framework is aimed at enabling a fair and unbiased evaluation of temporally resolved mass concentration of soot particles from the exhaust manifold of a diesel engine vehicle undergoing transient operation. It is important to clarify that the scope of this work does not distinguish between cold-start and hot-start emissions, nor takes the effect of ambient conditions into account. In order to achieve this, the first step is to develop a control oriented transient soot model that meets three key criteria. First, it must accurately capture the impact of powertrain transients on the resulting transient soot emissions. Second, it must be simple enough to enable control system design. Third, the model's inputs should ideally consist of quantities that are easy to simulate or control. The causality of the desired model is shown in Figure 1.5.

The evaluation of powertrain design also requires a systematic procedure for dealing with the issue that drivers potentially adapt their driving styles to a given design. In order to evaluate the implications of different powertrain design changes on transient soot production, it is essential to compare these design changes on a consistent basis. This problem is explored in the context of longitudinal motion of a vehicle following a standard drive-cycle repeatedly. The development of an algorithm is proposed that synthesizes the standard driver actuator set (accelerator and brake pedal position) for an automatic transmission vehicle such that soot emissions are minimized, enabling a fair comparison of different powertrain design changes.

Finally, potential changes in powertrain design are highlighted through transmission calibration and control. The transmission models play a critical role in creating high transient loads during gear-shift events, and high-fidelity RT models are sought such

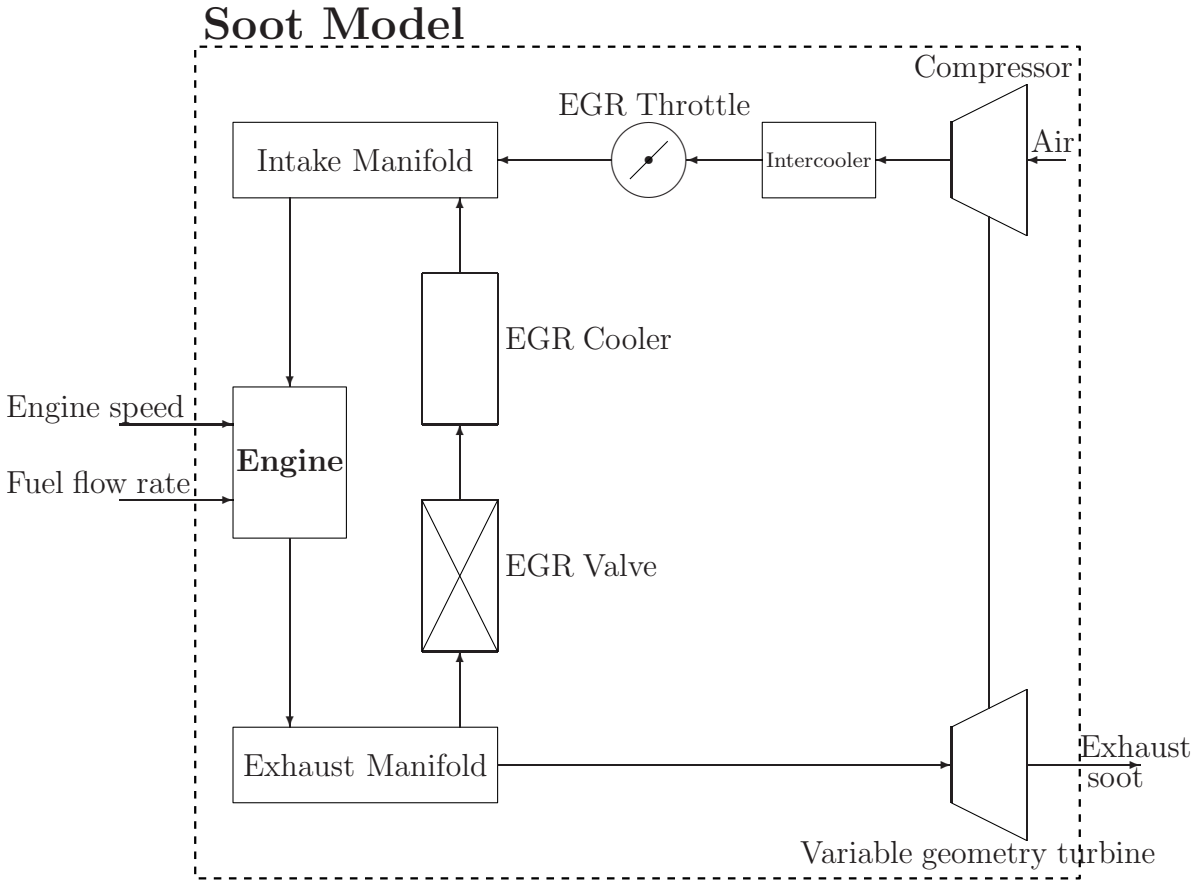

Figure 1.5: Desired Model Causality. Configuration adapted from [26]

that there is an accurate representation of drivetrain transients during EIL experiments. These models are required to run in real-time without requiring any additional numerical procedures such as multiframing or variable time-step solvers, while accurately representing the transient load on the engine, especially during shift events. They should also be able to accommodate a variety of commercially available transmission types for studying the impact of various vehicles/powertrains on transient soot without extensive modifications or parameter identification exercises.

Therefore, to summarize, this dissertation has three objectives:

1. Develop a computationally efficient model to estimate temporally resolved mass concentration of transient soot emissions from the exhaust manifold of a diesel

engine vehicle.

2. Synthesize driver actuator inputs that seek to minimize soot emissions using the transient soot model.

3. Develop high fidelity real-time model of the transmission for calibration and control both for EIL experiments and offline simulation.

1.5 Literature Review

The literature review associated with transient soot modeling and synthesizing driver input trace will be presented separately in the next two subsections.

1.5.1 Transient Soot Modeling

There exist several methods by which soot emissions can be modeled. The methods can be broadly classified into two different categories: physics based and empirical. Physics based models, at least to some degree, use physical principles to model the underlying phenomenon whereas empirical models are primarily data driven relationships. Most of the processes contributing to the formation of soot are extremely complex and are not adequately understood at a fundamental level [7]. Hence, it is not possible to construct models predicting engine operations just from the basic equations. The choice of the model, as always, depends on the objective of the study so that is can possess sufficient fidelity with lowest possible computational cost.

1.5.1.1 Physics Based Models

Physics based models that predict transient soot emissions and can be further classified as thermodynamics based or fluid dynamics based depending upon whether the equations are primarily based on energy conservation (thermodynamic) or a full analysis of fluid motion (fluid dynamics) [7]. Thermodynamics based models can be

further subclassified into zero-dimensional, phenomenological or quasi-dimensional. Zero-dimensional models are the most basic form of thermodynamic models as geometric flow properties are not modeled. Phenomenological methods add more complexity by providing details (that may be empirical) for some relevant phenomenon involved in the process. Quasi-dimensional methods add some specific geometric features like diesel fuel spray shapes to the basic thermodynamic model. In contrast, fluid dynamics models are multidimensional due to the modeling of geometric information of the flow field based on governing flow equations.

Zero-dimensional models of diesel combustion have been successfully used for predicting engine performance and fuel economy [27, 28] but traditionally have not been accurate for predicting soot [29]. Phenomenological models are usually semi-empirical in nature, i.e., they relate empirical observations of phenomena in a way consistent with the fundamental theory, but not necessarily directly derived from the theory. This category of modeling deals with the complexity of soot formation by representing the important species and mechanisms for the soot formation process. Perhaps the most popular (and most cited) phenomenological soot model is the two-step Hiroyasu model [30], which describes the net rate of change of the soot mass as the difference between the soot formation and oxidation processes. The soot formation is considered through a first order reaction of the fuel vapor, while the soot oxidation represents a second order reaction between the generated soot and oxygen available through empirical relationships. For both formation and oxidation processes, the temperature dependencies are described using an Arrhenius function. This model has widely been used though it is only valid in a narrow range of operating conditions [11]. Bayer and Foster [31] developed a crank-angle resolved zero-dimensional model for soot formation and oxidation based on the Hiroyasu model. A number of other variations of Hiroyasu model have been reported [32, 33] that include different

dependencies of the comprising terms for soot formation rate.

Beyond the two step process described in the Hiroyasu model, a more detailed description of soot formation and oxidation is possible using multi-step models, though this comes at a much higher computational cost. The most popular are those based on the works of Fusco et al. [34, 35]. These models describe the relevant processes of fuel pyrolysis, precursor and poly-cyclic aromatic hydrocarbons (PAH) formation, particle inception, surface growth, coagulation, oxidation of the particles, and growth species through an eight step process by considering average in-cylinder conditions. Further modifications to these models have been reported in a vast collection of articles [35–38]. Leung et al. [38] reduced the computational intensity by using only four steps. Other formulations include replacing the second order description of soot oxidation by considering different types of active sites for oxidation [39] and replacing the Arrhenius dependence of the formation with $\phi - T$ (fuel/air ratio and temperature) maps which include chemical kinetic considerations in the formation rate [40, 41]. Another class of phenomenological models consist of mean-value (MV) models where crank-angle resolved models are reduced to cycle-resolved models by using mean values of the states [42–45]. Although their accuracy for transient soot prediction is questionable, Kirchen et al. [46] showed that reasonable estimates can be obtained during a tip-in through a modified temperature representation.

Quasi-dimensional models include modeling of different zones in the cylinder. Warth et al. [47] coupled the base Hiroyasu model with a two-zone thermodynamic model. Tan et al. [8] extended the model to predict both soot and SOF. The influence of air entrainment into the soot formation zone was considered by [31] and the effects of turbulence were included by modeling representative mixing time scales [47] and the spray lift-off length [31]. Li et al. [48] extend the complexity further by describing a

four zone phenomenological soot model. In order to model further complexity, multidimensional models simulate the governing flow equations, often with the help of computational fluid dynamics (CFD). In order to determine spatially and temporally resolved in-cylinder soot distribution, Patterson et al. [49] implemented the Hiroyasu model with the oxidation process described by Nagle et al. [39] in a 3-dimensional CFD simulation. In further extensions to this work [50], the spray model was improved, enabling it to reproduce effects of EGR and multiple injection events. The model proposed by Fusco et al. [34] has also been implemented in CFD, and further improvements are reported in [37, 38, 51].

1.5.1.2 Empirical Models

Empirical models have been used be used in the literature to predict both cycle-resolved and time-resolved soot emissions from diesel engines. The underlying principle of these models is that they are data driven and can range anywhere from tuning the parameters of some of the physics based models to using complete black box models. Accordingly, the computational demand of these models can vary significantly depending upon the nature and structure of the model. Their advantage is that their use does not require a very deep understanding of the underlying mechanisms and these methods can be used for off-line optimization and control strategies. Their chief disadvantage is that they are not reliable for extrapolation beyond the ranges over which they were developed.

The empirical models range from quasi-stationary (QS) models to artificial intelligence based phenomenological models. Quasi-stationary models are based on steady-state maps of soot as a function of engine inputs and can be interpolated to obtain quasi-steady state predictions during simulation [52]. Although these models are simple and easy to implement, they fail to capture transient soot accurately, especially

the spikes during tip-in operations [10, 17, 53]. This is because although the fuel pump responds rapidly to the increased fueling demand after a load or speed increase, the turbocharger compressor air supply cannot match the higher fuel flow instantly, but only after a number of engine cycles owing to the inertia of the turbocharger as there is no mechanical connection between engine crankshaft and turbocharger [17]. In order to account for these transient discrepancies but at the same time maintain the initial goal of a simple and fast estimation, correction coefficients have been applied to the steady-steady soot emissions leading to the development of extended-QS models. These correction coefficients increase the instantaneous emissions at each operating point in the cycle based on the changes in engine operating parameters.

One of the most intuitive ways to correct for transient soot emissions is to include a correction factor based on load increase [54] at any given time-step. A similar correction factor was also used in [55], where transient soot, y, is calculated as

$$y(t) = y_{ss}(t) \cdot \left(1 + c_{load} \frac{(\text{current load change})_{t-1}^{t}}{\text{max load change}}\right) \cdot (\text{speed change})_{t-1}^{t} \tag{1.1}$$

where y_{ss} is the steady-state prediction and c_{load} is the correction coefficient. The value of c_{load} is not assumed to be constant and is varied by dividing the engine operating region into four regimes. In a similar approach, Hausberger et al. [56, 57] presented two different concepts for transient corrections: using multiple regression analysis via a black box compensation function and a multiplicative compensation based on the vehicle driving cycle. While both the models were able to correct for the total soot emissions (and not improve their temporal resolution), the former in some cases increased the temporal error. They also concluded that much less correction is needed for engines certified for Euro 2 due to less active control of the injection angle.

A different approach was adopted by Ericson et al. [58] where correction coefficients were based on air-fuel ratio during transients and a delay model was incorporated to account for the turbocharger lag. Benz et al. [59, 60] pointed out the need for control oriented transient soot models and proposed a nonlinear extended QS emission model derived with a symbolic regression (SR) algorithm. The correction factor for the set-point deviation model was calculated as

$$\gamma_{soot} = (\gamma_{m_{air}}^{\gamma_{m_{air}}^{a}(C_1/\gamma_{\phi_{B90}})^{-\gamma_{P_{rail}}}})^{C_4 \cdot b} \tag{1.2}$$

where γ is the normalized value of the variables, m_{air}, P_{rail} and ϕ_{B90} represent the cylinder air mass when the intake valve is closed, fuel rail pressure, and location of the 90% fuel mass burnt, respectively. The variables a and b were defined as

$$a = \frac{C_2 \gamma_{m_{air}}^{C_3}}{\gamma_{P_{rail}}} + C_6 \tag{1.3}$$

$$b = p_{mf} + \gamma_{\phi_{B90}} + C_7 \tag{1.4}$$

where p_{mf} is the fuel mean pressure. The six variables were identified using experimental data and it was shown that the model accuracy improved during tip-in operations. Eastwood et al. [61] further extended the work to model deviations from QS estimates as a function of deviations of mass air flow (MAF) and manifold air pressure (MAP) from their steady-state counterparts. They were able to predict the transient soot qualitatively given a fine temporal resolution of the inputs, but quantitative accuracy varied with a number of other factors [46, 53]. Khan et al. [62] presented some empirical correlations for engine operating conditions to engine out soot and similar work has been described by Kirchen [11] and Watson [63]. In almost all cases of extended-QS approach, the choice of model structure is largely based on heuristics, and validation is only demonstrated for individual tip-in operations. The

chief disadvantage of these approaches is that all load increases are treated equally. It is a well known fact that due to the unfavorable turbocharger compressor characteristics at low loads and speeds, load changes commencing from high speeds are less severe than the ones commencing from lower engine speeds, owing to higher initial turbocharger boost pressure. Also, during the motoring segments of the transient cycle when the vehicle is coasting or braking, soot emissions from the extended-QS models are either zero or uncorrected. Finally, most of these models require a multitude of inputs, forcing the modeler to include combustion and air-flow dynamics at least to some degree.

Other empirical methods include SISO ARMA model developed by Anand [64] for online prediction of transient soot from experimental data, and black box models based on artificial neural networks (ANN) [65, 66]. Ouladsine et al. [67] demonstrate the use of neural networks for predicting opacity, though transient soot is not predicted. The use of ANN in predicting transient soot is presented by Traver et al. [66] based on characteristic pressure trace variables such as combustion center, maximum heat release rate, or peak pressure generated from steady-state measurements. Another successful transient soot model is presented in [68] using a 4 neuron multi-layer peceptron (MLP) for function approximation. The major disadvantage of such approaches is that a vast number of measurements are needed to identify the parameters. As a combination of empirical and phenomenological modeling, Brahma [69, 70] uses a neural network to parameterize the variation of the Hiroyasu model by introducing a total of 23 model weights. After training the model, it was capable of predicting the soot emissions better than either the soot model without the weighting factors, or a standard neural network. However, the cylinder pressure and available fuel mass are required as model inputs. Also, the accuracy of these models relies on the modeling of underlying phenomenon, which is not well understood at a fundamental level. Johri

et al. [71] have developed a neuro-fuzzy logic based transient emission model that relies on dividing the input space into smaller subspaces and fitting local models. They demonstrated successful fits, although the model still requires a number of different inputs.

1.5.1.3 Summary of Transient Soot Modeling Literature

Many different methodologies are available for the estimation of diesel exhaust soot emissions. Several researchers have successfully coupled single and multizone, as well as CFD simulations, with detailed soot formation and oxidation models. Due to the computational requirements of these approaches, however, there is considerable interest in phenomenological models which only consider the most relevant processes and still allow the prediction of the soot emissions with lower computational costs, albeit with a lesser fidelity. The Hiroyasu model and all of its discussed variants require cycle resolved cylinder pressure as an input while several also require histories of the heat release rate, injection velocity or mass, and formation and oxidation temperatures. Several researchers have commented on the sensitivity of the various soot models to the mixture state description and in almost all cases, the soot model must be parameterized against measured soot emissions. The underlying physical models also face much debate due to the presence of formation and mixing phenomena that are not completely understood. As the complexity of the model is decreased, the calculation time also decreases but at the cost of reduced extrapolative performance. As the interest of this work lies in time-resolved soot from the exhaust manifold (as opposed to cycle resolved soot from the engine), empirical models are very appealing. Existing empirical models can range from steady-state maps to extended quasi-steady state approaches to neural network based models. The methods that are accurately able to predict transient soot over a significant engine operating range require a lot of data and/or a number of engine inputs that are not easy to simulate. Hence, in

seeking a model that is easily identifiable, requires minimum number of inputs, is computationally efficient for systems level work, and estimates transient soot accurately, there is a gap in the literature that needs to be filled.

1.5.2 Synthesis of Driver Actuator Inputs

It has long been established that driving style has a significant effect on vehicle emissions [72, 73]. Holmén et al. [74] did a real world study of 24 drivers driving the same vehicle under the same conditions and used on-board exhaust emission and engine operating data analyzers to record their emission performance. They showed statistically significant differences in CO and NOx emissions between drivers. After analyzing the data they concluded that under the same experimental conditions, the variability associated with individual driving styles, like the intensity, frequency and duration of acceleration events, result in significant variability in exhaust emissions. The changes in soot emissions with driving style are also highlighted in [75–77] in the context of loading of DPFs, as the filter should be able to regenerate under all driving conditions. Clark et al. [25] conducted laboratory experiments with different driver aids and showed that different driving styles (e.g. normal, aggressive, non-aggressive) followed the drive cycle legally, but driver pedal behaviors were quite different, with PM emissions for aggressive driving style being twice as much for the non-aggressive driving style. They developed statistical correlations to compare driver performances and incorporated more robust emissions control strategies. One of the ways to isolate the variability associated with driving style from the evaluation of a drivetrain design is to synthesize driver inputs that produce the best possible performance (minimum soot emissions) from the vehicle. Methods for obtaining such driver input traces are discussed next.

1.5.2.1 Driver Input Trace Determination

Seeking the driver actuator set that maximizes a performance objective, the literature offers techniques roughly belonging to two different categories: trajectory optimization methods and learning based methods. Trajectory optimization techniques can be further classified into direct (e.g. optimal control) and indirect (e.g. non-linear programming (NLP)) methods [78, 79]. Since the desired task is to find the driver input trace that maximizes some performance objective, only the literature belonging to conventional and hybrid vehicles is presented here, with the understanding that for hybrids the problem amounts to finding the optimal power distribution trace instead of driver trace. An example of direct trajectory optimization techniques is the work presented by Hendrikx et al. [80] to calculate the minimum lap time of a vehicle by synthesizing steering and propulsion forces via optimal control. However, due to the inherent non-linearities in vehicle dynamics/powertrain problems and the sufficiency of solution at discrete points under most conditions, NLP techniques are more popular for trajectory optimization. NLP techniques can be further classified into the ones using static optimization methods such as linear programming and sequential quadratic programming (SQP) [81], and the ones using dynamic optimization techniques such as dynamic programming [52, 82]. Propkop [81] parameterized the control inputs for the driver for trajectory planning using predictive online optimization and the solution was then obtained using SQP. Velenis et al. [83] present an analysis for rally racing techniques by parameterization of driver steering, acceleration and braking traces, and solving non-linear optimization for executing a trail-braking maneuver. Gordon et al. [84] solve the trajectory optimization problem for obstacle avoidance using gradient descent (for benchmarking purposes). In the context of hybrid vehicles, Tate et al. [85] demonstrate the use of approximate linear programming for finding the optimal power management strategy.

Because of the simple pointwise nature, static optimization techniques are computationally more efficient but optimize the inputs for an instant in time instead of within a time horizon. Dynamic optimization techniques consider the dynamic nature of the system and are generally more accurate under transient conditions but suffer from the curse of dimensionality, increasing the computational intensity exponentially with inputs/states [52]. As a result, learning based techniques are increasingly being used to construct computationally efficient solutions that are near-optimal. Cao et al. [86] demonstrated the improvement in driver steering control input by updating the fuzzy logic in each iteration, emulating the driver's learning process for a given driving situation. Chen et al. [87] eliminated the driver uncertainty during emission tests by using a robot driver that learns the performance of the vehicle during calibration and then uses the derived fuzzy logic rules to drive the vehicle. Carlsson et al. [88, 89] developed predictive driving strategies emulating foresight information for improving fuel economy in subsequent trips along the same route by learning the road characteristics. Gordon et al. [84, 90] describe a dual-model approach for synthesis of driver steering, braking and acceleration inputs. A sub-optimal set of driver controls is synthesized by iteration between two level of models and applied to obstacle avoidance and high-speed competitive driving.

Such optimal solutions can also be used as driver aids to educate the driver and improve vehicle performance. Van der Voort et al. [91] report such a support tool that included a normative model formulating optimal driver behavior for reducing fuel consumption. Tactical and strategic layers of the model analyze the maneuvers and if the actual behavior deviates from this optimal behavior, it presents advice to the driver on how to change the behavior. It was shown that the use of such a tool can result in over 20% improvement in fuel economy. Additionally, instead of solving for the driver trace some approaches solve the inverse problem of optimizing

the engine/vehicle calibration to driving style (e.g. automatic mode selection) to maximize the performance objective [82, 92].

1.5.3 Transmission Modeling

This subsection presents the literature review for automatic transmission modeling for the purpose of emulating low frequency transient loads on the engine. A general transmission modeling review is presented first, followed by the RT models. Only the modeling of the transmission gearbox is considered here, and other systems, such as torque converter and differential are not discussed.

The automatic transmission model can be divided into three separate components: a compound epicyclic geartrain, torque transmitting friction elements (such as clutches and band brakes), and transmission hydraulics. Since the primary interest is the development of control-oriented models for analyzing low-frequency aspects of transmission's dynamic system behavior, the compound epicyclic gearsets along with the interconnected shafts are modeled as lumped parameter mass-spring-damper systems. Such models do not include effects such as friction between gears and backlash [93]. The compound planetary geartrain has more than one planetary gearsets connected to other gearsets in different arrangements to allow different speed ratios during the transmission's operation. Popular arrangements include modified or extended Simpson [93–99], Ravigneaux [100–102] and Lepelletier [103–105] configurations. Several methods are available in the literature to analyze the kinematics and dynamics of these interconnected geartrains. Leising and Benford [106] developed a lever analogy to represent these relationships by drawing levers proportional to the number of gear teeth. This technique has since been used by many researchers including Tugcu et al. [107], Karmel [108], Lee et al. [109] and Liu et al. [110]. While this method is simple and convenient for analysis of the steady-state behavior, it has limitations for

dynamic analysis. Another graphical tool that is extensively used for modeling the transmission dynamics of compound epicyclic geartrains is the bond graph. Based on the seminal work by Runde [94], this modeling approach has been widely used [93, 95, 96, 99, 111, 112]. Acausal modeling such as the implementation in Modelica has also proven beneficial due to the ease of obtaining the dynamic equations [103, 113]. Finally, deriving the governing equations by the traditional way of using appropriate conservation and constitutive relationships is perhaps the most popular way to deal with automatic transmission models. In this approach, the model is divided into various modes based on the interconnections during specific phases of gear-shifts and equations are derived for each mode individually [100, 101, 114–116].

Friction elements are widely utilized to alter planetary gear configurations for automatic shifting. They consist of (wet) clutches and band brakes. These friction elements primarily determine the automatic transmission's output torque during a shift event and represent very critical components of the transmission model [117, 118]. This necessitates the modeling and simulation of slip-stick friction for torque transmission, while the effects such as clutch drag and viscous friction dynamics are often ignored in control-oriented models [96]. The slip-stick friction models can be categorized as static or dynamic models. The dry friction model proposed by Coulomb, is one of the most famous static models. It models friction torque as a function of speed while slipping (effort source) and becomes multivalued when surfaces are stuck to keep their relative velocity zero (flow source), though still within bounds specified by the Coulomb law [119, 120]. This causal inversion causes problems in model formulation by changing the explicit nature of model formulation, and has been an extensive area of research under the title of 'ideal switching' [121]. To circumvent this problem various alternate models have been proposed. One approach to overcome the discontinuity is to approximate it by a linear region near zero velocity, resulting in the

so called classical model [96, 122]. Although easy to implement, it allows the body to accelerate even though the forces on the body are less than peak stiction force. It also causes numerical stiffness in the model if the linear approximation around zero velocity has a steep slope. One popular way to remove the discontinuity is by using a hyperbolic tangent function instead, though the problems associated with acceleration and numerical stiffness still persist. Karnopp proposed a fixed causality model in 1985 [123] to overcome the lack of verisimilitude at low velocities. This was achieved by introducing a narrow stiction region in which the friction torque does not depend on relative speed but rather on equivalent applied torque to the friction element. Thus, the system is effectively reduced during stiction while the friction force is calculated by an empirical function of slip speed outside this region. Though this method is quite accurate and easy to simulate [96, 122], it requires the derivation of separate set of equations for each possible combination. Hence, the complexity of the friction model increases exponentially with the number of friction elements.

To account for some of the observed dynamic friction phenomena, a modified classical friction model was proposed by Armstrong [119, 120]. It introduces temporal dependencies for stiction and Stribeck effect and the sliding friction is equivalent to a static model with delay. The major disadvantage of this model is that it requires seven parameters to be estimated. One of the most fundamental dynamic models based on Coulomb's friction law is the Dahl model [124, 125]. It is a first-order model that predicts velocity reversal and leads to hysteresis loops but does not capture Stribect effect or stiction. Haessig and Friedland [122] introduced a friction model called the bristle model that captures the behavior of the microscopic contact points between two surfaces. The bristles are represented as stiff springs and the model is numerically inefficient and results in oscillations due to the lack of damping [124]. They then proposed a reduced version of the bristle model, known as the reset integrator

model [122] that is computationally feasible. It models the friction element as spring when slipping and as spring-damper when stuck. The switching between the slip and stick states is dictated by the displacement of the spring. With this model the logical complexity does not increase with the number of friction surfaces, like it did with Karnopp model. It was shown that reset-integrator model approaches Karnopp model as spring stiffness and damping rate go to infinity. The primary disadvantage of this model is numerical stiffness if high damping coefficients and stiff springs are used. Margolis [121] proposed a variation of this model where slip velocity was used as a switching criterion between the two discrete states instead of the spring displacement, and the friction element behaves as a damper when slipping. Another popular dynamic model that models the Stribeck effect as well as varying break-away force and frictional lag is the Lund-Grenoble model (commonly known as the LuGre model) [126]. The difficulties associated with using this model includes a number of parameters to be estimated and numerical stiffness at low velocities. Padthe et al. [125] presented a comparison of Dahl, LuGre and Maxwell-slip model and showed that these models can be classified as generalized Duhem models and can be used to predict hysteresis effect. Other dynamic friction models that are specifically used for clutch friction modeling include artificial neural network based models [118, 127]. This approach was shown to be especially suited in the presence of hydrodynamic effects, as well as predicting time dependent engagement behavior, without adding any significant computational load over static models. However, they require a large amount of test data to be developed and their predictability depends on the nature of the test data. More information on various other friction models in presented in these literature review articles: [118, 119, 124, 128].

The automatic transmission model involves multiple friction interfaces and hence more computationally intensive friction models are generally not suitable for this

application. The most commonly used friction models include implementing every causal combinations of Coulomb friction model [94, 95, 99, 111], Karnopp model [93, 96, 103], and the Margolis model [100]. It is observed that when the equations of motion are derived manually from first principles, use of the Coulomb friction model is preferred. When automated subroutines are used for modeling (such as modelica planetary gear-set models), then the use of a modular friction model is important. The pressure profiles required for the clutches are either specified as feedforward signals or simulated using a transmission hydraulics model [107, 129–131].

1.5.3.1 Real-Time Models

Simulating the automatic transmission in RT is a challenging task as the models may be logically complex or result in numerical stiffness. One way to avoid these issues is to not model clutch friction and use empirical blending functions to model shift dynamics [24, 132]. These models, however, can result in unrealistic shifting behavior at some operating points resulting in loss of fidelity during those shifts. Static friction model such as Karnopp model have been used for RT transmission models, but different techniques are employed to reduce the logical complexity [103, 129]. Kozaki et al. [129] reduce this clutch friction and hydraulics model using surrogation. Otter et al. [103] use event-driven integration method for offline simulation and system description is written as a linear complementary problem (LCP) [133]. They then use this model in RT by modifying the fixed point iteration scheme. Hagiwara et al. [134] demonstrate RT transmission and hydraulic models simulation by multiframing, but the model details are not presented. Klages et al. [100] present the use of dynamic reset integrator model with the RT simulation of Ravigneaux geartrain. The numerical stiffness during simulation is avoided by careful selection of PI gains, while hydraulics were not simulated. While transmission hydraulic models usually are not conducive to RT simulation, Watechagit [135] presents a RT model developed from reducing a

detailed model of transmission hydraulics using activity analysis [136]. The model runs in RT while capturing only the dominant dynamics that determine the clutch pressure behavior.

1.6 Approach

Engine-in-the-loop experiments are first conducted by developing RT drivetrain and vehicle dynamic models that possess sufficient fidelity for transient loading of the engine. The models are then imported on a RT-platform and used to control the engine dynamometer to allow closed-loop EIL experiments. The transient soot data are recorded using a differential mobility spectrometer (DMS) at 10Hz and correlations are drawn between soot spikes and driver input. It is shown that predictions from steady-state maps do not match well with transient data and that driver aggression can significantly impact the transient soot produced from the vehicle.

Next, a control oriented model capable of predicting temporally resolved soot at the exhaust manifold of a diesel engine is developed. The choice of inputs is dictated by signals that are easy to simulate. In this context, the inputs are chosen to be engine speed and fuel flow rate. Boost pressure is not chosen as an input as simulating it involves modeling the intake manifold system (Figure 1.5) that represents exhibits high degree of plant nonlinearity, complex MIMO interactions, and non-minimum phase dynamics [26]. These choice of inputs enable the system identification to be carried out with minimum number of sensor signals. Both of these signals are usually the outputs of the powertrain supervisory control, and this model enables the control system development for soot reduction without simulating the combustion dynamics or much detailed information about the engine subsystem. The experimental data recorded are analyzed for statistical and spectral properties and system identification techniques are then used to fit a model to the inputs and the soot output. A

dual-input single-output (DISO) Volterra series with low parametric complexity is developed and the model is reduced using Proper Orthogonal Decomposition (POD). It is shown that this model can furnish good estimates for vehicle-level work, both qualitatively and quantitatively. The model is then validated on a number of different datasets, and a comparison with steady-state models is presented.

In-order to enable a fair comparison of the powertrains by considering that drivers potentially adapt their driving styles to a given design, an iterative learning process is proposed. It uses the notion that the performance of a system that executes the same task multiple times can be improved by learning from previous executions [137]. A first order proportional-derivative (PD) controller is developed based on physics of soot formation, and the EPA constraint of vehicle following the FTP cycle is implemented using a lower level controller. Total soot is then shown to monotonically decrease with the number of iterations. In-order to compare the performance of iterative learning based algorithm, the problem is also solved using a linear programming (LP) based approach. The system is linearized, sensitivity functions are numerically calculated, and perturbations in driver pedal position are solved for that yield least total soot for the drive-cycle while subjected to various constraints. The process is then repeated iteratively until no appreciable improvement is detected. The results indicate that the iterative learning based driving can give substantially better results, while taking only a small fraction of computations as compared to the linear programming based solution.

Physics based RT transmission model development for EIL experiments is proposed using the dynamic Margolis friction model. Popular commercial power transmission designs are analyzed and it is shown that the majority of them involve an oncoming friction interface and an offgoing friction interface during a gear-shift event that

produces the characteristic shifting dynamics for such transmissions. Hence, a dual-clutch model is proposed that emulates this clutch to clutch shift inherent in powershift transmissions by alternately acting as on-coming and off-going clutches. The different clutch capacities and friction properties of various clutches in the transmission are implemented using gain scheduling. The effective inertia and compliance of the gearset is reflected as a lumped parameter model. It is shown that this formulation does not require any other information about the system and hence can be used as a subfunction in any vehicle system model with a powershift transmission. Volterra series model is then used to capture the effect of gear-shifts from this transmission model on transient soot, and results are compared to the soot obtained using blending function based transmission models.

1.7 Contributions

This work makes three new contributions to the literature:

1. It develops a low order computationally efficient transient soot model based on Volterra series with just two inputs.

2. It provides a consistent basis for evaluating soot emissions, independent of individual driving styles by synthesizing driver inputs using iterative learning based algorithm.

3. It incorporates a generalized framework for RT simulation of powershift transmissions using dynamic friction models while using a fixed integration time step solver. This in turn produces more accurate transient loading on the engine as well as enables transmission design and calibration for reduced soot production.

1.8 Outline

The outline of the dissertation is shown in Figure 1.6. The rest of the dissertation is organized such that Chapter 2 presents the analysis of transient soot data for spectral and statistical properties and develops a dual-input single output Volterra series model. Chapter 3 presents the development of an iterative learning based algorithm and compares the results with the same problem solved using a linear programming (LP) based algorithm. Chapter 4 presents the development of a physics based RT powershift transmission model for EIL experiments. Chapter 5 outlines the future work and draws the conclusions. The physical mechanisms of soot formation are briefly discussed in Appendix A, and the details of Engine-in-the-loop experiments are presented in Appendix B. The real-time vehicle models and their integration to enable EIL experiments is presented in Appendix C, and the model of dynamic wheel slip for RT simulation is discussed in Appendix D. Appendix E discusses data processing and provides the datasets.

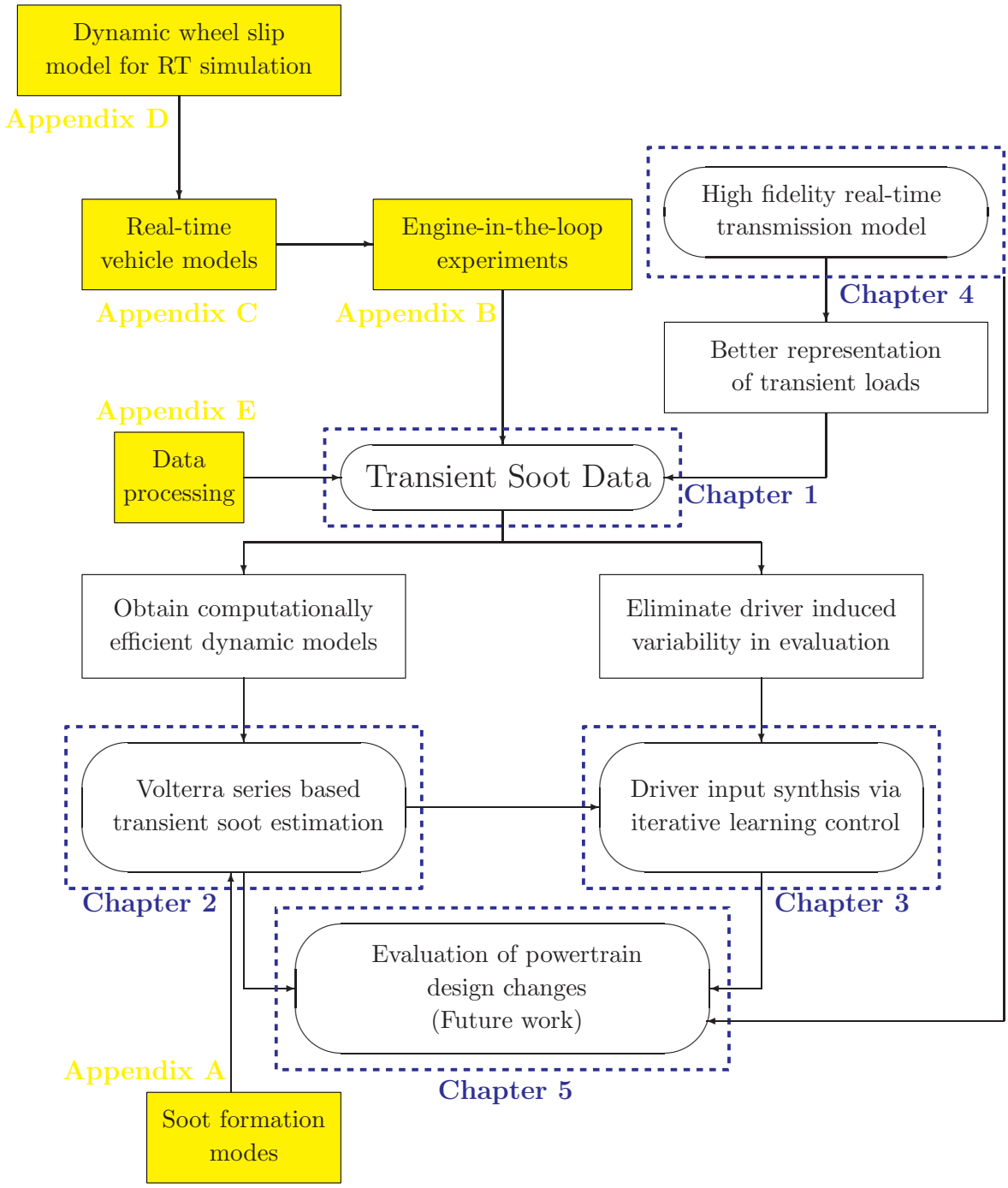

Figure 1.6: Outline of the dissertation

CHAPTER II

Transient Soot Estimation Using Volterra Series

This chapter describes the development of a Volterra series based model for predicting transient soot emissions from a diesel engine with fuel flow rate and engine speed as the two inputs to the model. Engine-in-the-loop experiments presented in the last chapter are used to collect data and then used to construct a third-order dual-input single-output Volterra series to model this system. Parametric complexity of the model is reduced using proper orthogonal decomposition, and the model is validated on various datasets. It is shown that the prediction accuracy of transient soot significantly improves over the steady-state maps, while the model still remains computationally efficient for systems level work.

2.1 Introduction

This chapter presents a Volterra series model for the transient soot emissions produced by a diesel engine, with fuel flow rate and engine speed as the two inputs to the model. The model is intended for the purpose of designing powertrain-level supervisory controllers that minimize transient soot emissions, among other possible objectives. This can be particularly important in the context of hybrid diesel propulsion systems. While such systems offer more flexibility in controlling their engines as compared to the conventional powertrains, optimizing their supervisory control

for fuel economy alone can lead to frequent and sharp load increases, thereby significantly penalizing soot emissions [23]. Our overarching goal, therefore, is to develop a transient soot emission model that meets three key criteria. First, it must accurately capture the impact of powertrain transients on the resulting transient soot emissions. Second, it must be simple enough to enable control system design. Third, the model's inputs should ideally consist of quantities that are easy to simulate or control, such as engine speed and fuel flow rate.

Quasi steady state models based on steady-state emission maps have been used in the literature for control-oriented modeling but they fail to capture transient soot accurately, especially the spikes during tip-in operations [6, 17, 23, 53]. More detailed models exist in the literature that capture transient soot formation by simulating the combustion events using computational fluid dynamics (CFD) [138], phenomenological methods [3, 17, 29, 139], heuristic macro-parameter approaches [140] or using black box models such as artificial neural networks [141]. However, these approaches require a number of inputs to the model often not available to the control engineers involved with vehicle-level control development. Also, simulating combustion can sometimes be prohibitively slow in the context of system work [139].

In this work we seek to develop a model capable of predicting temporally resolved soot at the exhaust manifold of a diesel engine, subjected to the transient loads emulating the operation in a vehicle following the FTP-75 city cycle, with just two inputs: engine speed (ω_e) and fuel flow rate ($\dot{m}$). Both of these signals are usually the outputs of the powertrain supervisory control, and this model will enable the control system development for soot reduction without simulating the combustion dynamics. Although this work is focused on modeling the diesel engine soot emissions during the FTP-75 city cycle, the techniques and analysis presented here can be generalized

to other engines with different inputs and outputs. Experimental data for transient soot are recorded using Engine-in-the-loop (EIL) experiments of conventional and hybrid diesel vehicles. The data are analyzed for statistical and spectral properties and system identification techniques are then used to fit a model to the inputs and the soot output. It is shown that a dual-input single-output (DISO) Volterra series with low parametric complexity can furnish good estimates, both qualitatively and quantitatively. The model is then validated on a number of different datasets, and a comparison with steady-state models is presented.

The rest of the chapter is organized such that section 2.2 briefly describes the test conditions for recording the data and their analysis is presented in section 2.3. Section 2.4 develops the Volterra series model used for the identification of transient soot. Section 2.5 presents the model validation results, and section 2.6 ends the chapter with a summary.

2.2 Data Collection

The transient soot data are recorded using Engine-in-the-loop (EIL) testing, presented in Appendix B. The driver's throttle command (α) is communicated to the engine controller, which is then converted into an equivalent fuel flow rate and commanded to the engine. Thus during the EIL simulation, the engine subsystem is controlled by two exogenous inputs, ω_e^{ref} and $\dot{m}$ (or α). Along with the EIL simulation of the conventional vehicle [2, 24], models for three other powertrain configurations are also implemented: virtually downsized engine (scaling down the torque measurement of the engine to emulate a smaller engine), parallel electric hybrid [142], and series hydraulic hybrid [143]. These different configurations subject the engine to different operating points and transient loads, generating data that cover a wide range on the engine map. A downsized engine results in much harsher transients, series hydraulic

hybrid subjects the engine to a lot of steady-state operation, whereas conventional vehicle and parallel electric vehicles operate the engine at different transient profiles. Multiple runs are made for each configuration in order to have separate datasets for identification and validation.

These experiments were conduced by Hagena [4], and post processed data was made available for this work. A total of 17 datasets were used for identification and validation exercises in this work. All data were recorded with warmed-up engine and ambient conditions were assumed to be constant. The inputs and output for these datasets, along with the post-processing details are presented in Appendix E. Interested readers are referred to [4] for further details.

2.3 Statistical and Spectral Data Analysis

In this section we analyze the recorded data for noise, coherence and cross-correlations. The input ($\dot{m}$ & ω_e) and output ($Soot$) data from EIL testing are sampled at 10Hz for the entire FTP-75 city cycle. This soot data should not be confused with the cylinder's cycle-to-cycle soot emission, which has dynamics of a much faster timescale. The soot data here is the engine's soot emission per unit time, as measured from the exhaust manifold, and has much slower dynamics due to the presence of the turbocharger and the exhaust manifold, and hence a sample rate of 10Hz suffices. The data obtained are first analyzed for high-frequency noise. Figure 2.1 shows the average power spectra for the inputs and the output of a sample dataset. It is observed that each of these signals primarily consist of low frequency components, and are devoid of any significant high frequency noise. There is no pre-filtering to prevent aliasing, because at frequencies near the Nyquist frequency, signals are almost 50dB lower than those in the low frequency range.

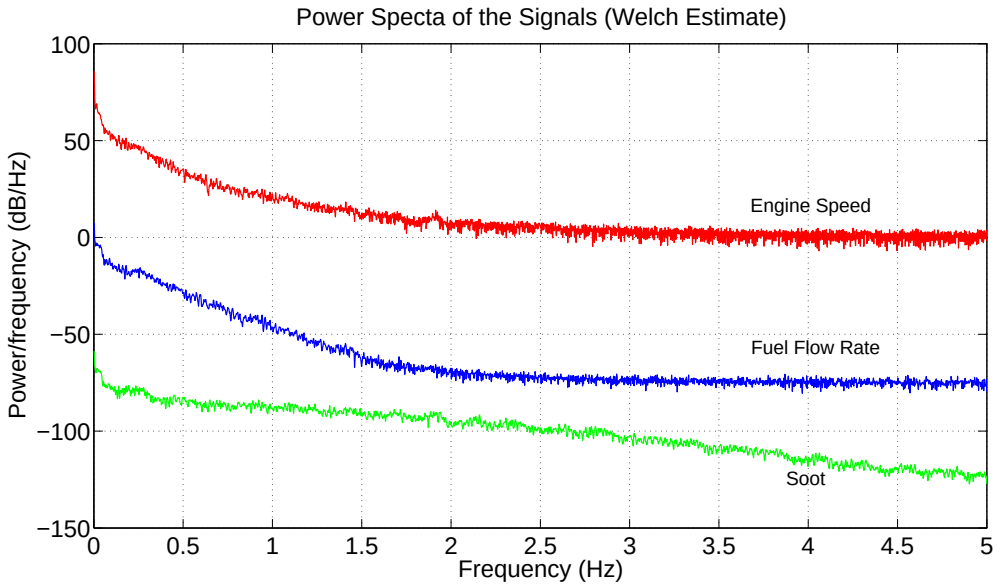

Figure 2.1: Sample signal spectra

Coherence functions can be used to investigate the degree to which a given output can be linearly predicted from all of the system inputs and to determine the frequencies over which a linear model can accurately characterize the system dynamics. Quadratic coherence always takes on a value in the interval $[0, 1]$, with a value close to 1 if there is a linear response between the input and the output, serving as a form of correlation function in the frequency domain [144]. Regions of low coherence indicate insufficient input power in that frequency range, significant system nonlinearities, noise, or contributions from unmeasured inputs [145]. Partial coherence provides an estimate of the linear relationship between one input and one output for multiple-input multiple-output (MIMO) systems. These estimates are equivalent to ordinary coherence estimates after the effects of all other inputs have been removed from both the input and output of interest [145, 146]. Let the output of our system (*Soot*) be represented by Y, and the cross-spectrum between two signals x and y be represented by G_{xy}. Then the partial coherence functions for our system with two inputs and one

output are given by

$$\gamma^2_{\dot{m}Y\cdot\omega_e}(f) = \frac{|G_{\dot{m}Y\cdot\omega_e}(f)|^2}{G_{\dot{m}\dot{m}\cdot\omega_e}(f)\cdot G_{YY\cdot\omega_e}(f)} \tag{2.1}$$

$$\gamma^2_{\omega_e Y\cdot\dot{m}}(f) = \frac{|G_{\omega_e Y\cdot\dot{m}}(f)|^2}{G_{\omega_e\omega_e\cdot\dot{m}}(f)\cdot G_{YY\cdot\dot{m}}(f)} \tag{2.2}$$

where the residual spectrum, $G_{xy\cdot z}$, is defined as

$$G_{xy\cdot z}(f) = G_{xy}(f)\cdot\left[1 - \frac{G_{xz}(f)\cdot G_{zy}(f)}{G_{zz}(f)\cdot G_{xy}(f)}\right] \tag{2.3}$$

These partial coherence functions are plotted in Figure 2.2 for sample signals. Both of these partial coherence plots indicate a lack of strong linear relationships between $\dot{m}$ & *Soot*, and ω_e & *Soot*, for all frequencies. Hence our system warrants the use of a non-linear model structure for identification. Figure 2.3 shows the quadratic coherence estimate between the inputs of the model. Except at very low frequencies, the quadratic coherence estimate is low, indicating low dependence between the inputs, and hence requiring the need of a dual-input single output (DISO) model.

The correlation between the inputs and the output is analyzed next. Figure 2.4 shows the cross-correlation of *Soot* with ω_e, and Figure 2.5 shows the same function for *Soot* and $\dot{m}$, at different time lags. Since the time constants of the system are much smaller than the total drive cycle, only the cross correlations corresponding to the smaller time lags are shown. Both plots indicate that the correlations change for different data-sets (conventional vehicle, downsized engine, parallel electric, and series hydraulic) making them valuable for the validation of the proposed model. Also, since cross-correlations decrease with time, the system exhibits fading memory and hence a finite order model can be used. In terms of time-history, strong correlations are exhibited only around zero lag. Figure 2.6 shows the magnified view of the cor-

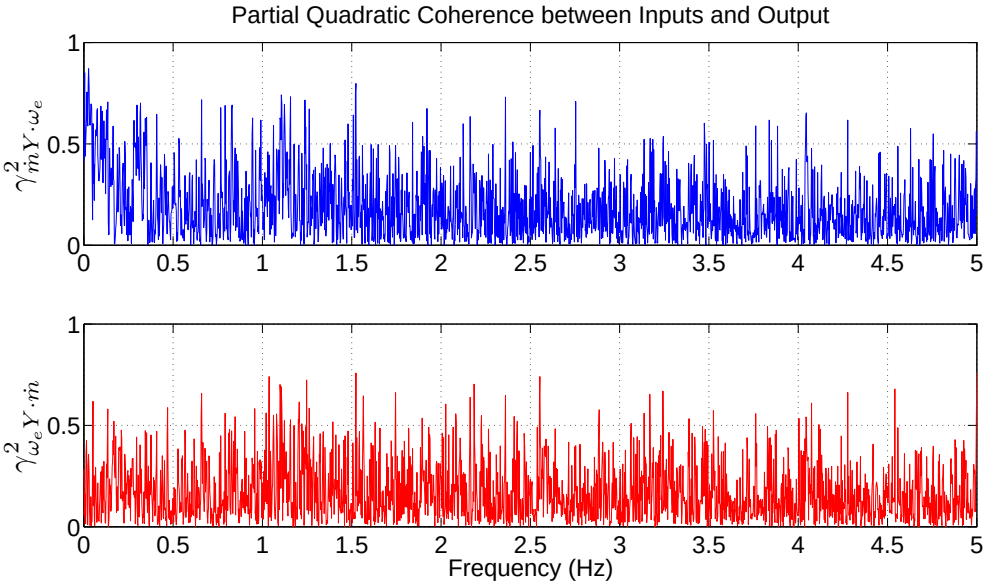

Figure 2.2: Sample coherence spectrum between inputs and output

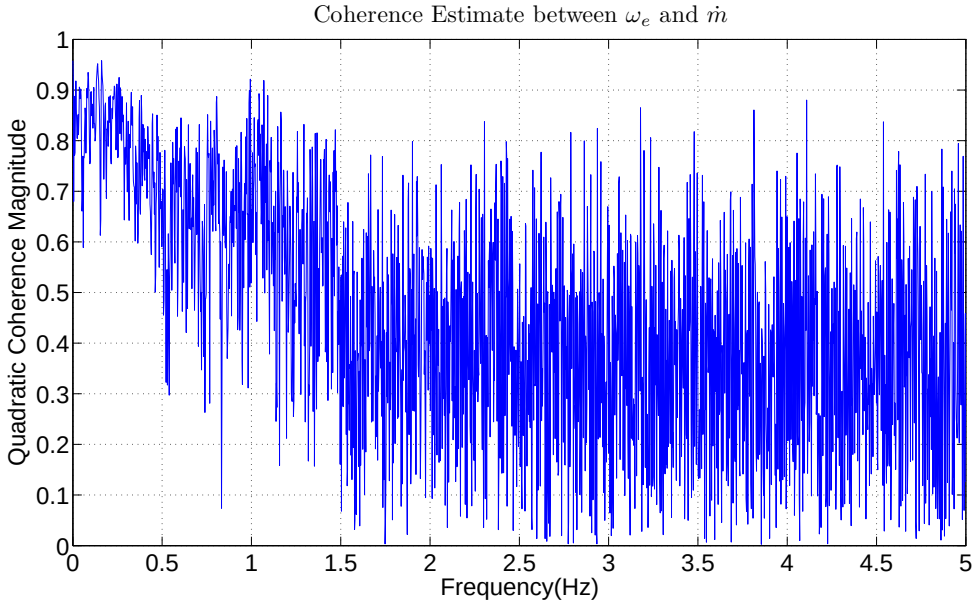

Figure 2.3: Sample coherence spectrum between inputs

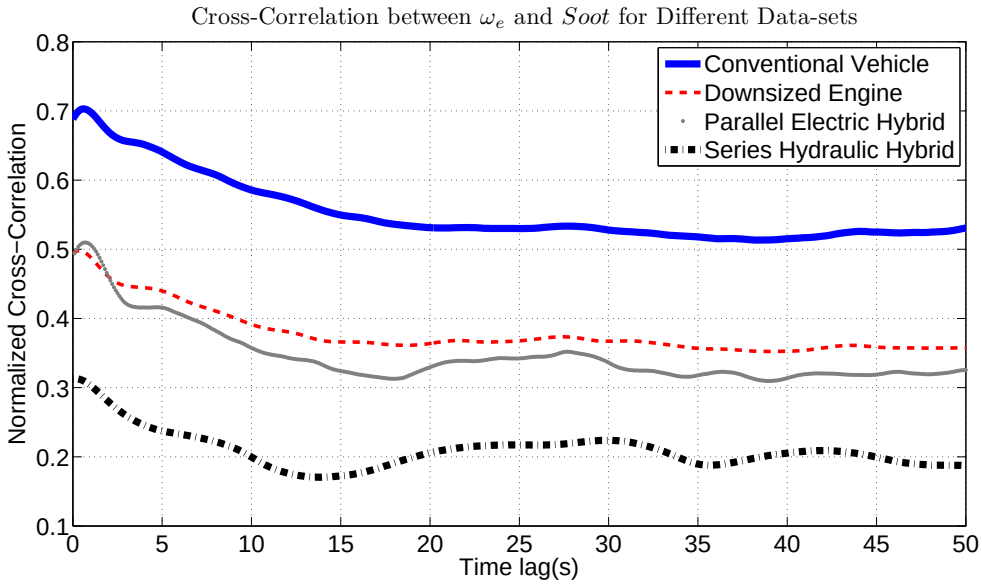

Figure 2.4: Cross-correlations between ω_e and *Soot*

relation coefficients for a sample dataset. The peak correlation of the transient soot with the inputs is not at zero lag but slightly delayed, due to the slower exhaust manifold dynamics. Also, higher correlations are exhibited with the time-lag of less than one second, and hence the inputs in this window will be used for identification.

2.4 Transient Soot Volterra Models

This section presents the development of the proposed transient soot emission model using a Volterra series. Volterra series are non-linear functional series with polynomial basis functions, and can be interpreted as a direct generalization of the linear convolution integral [147, 148]. For a single-input (u), single-output (y) (SISO) system, it can be expressed as

$$y(t) = \sum_{n=1}^{\infty} y_n(t) \tag{2.4}$$

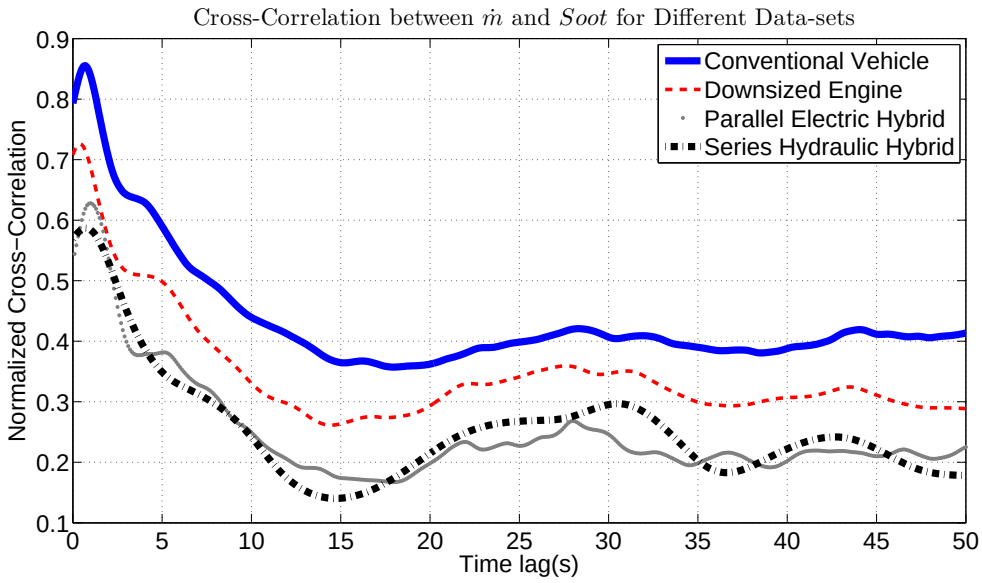

Figure 2.5: Cross-correlations between $\dot{m}$ and *Soot*

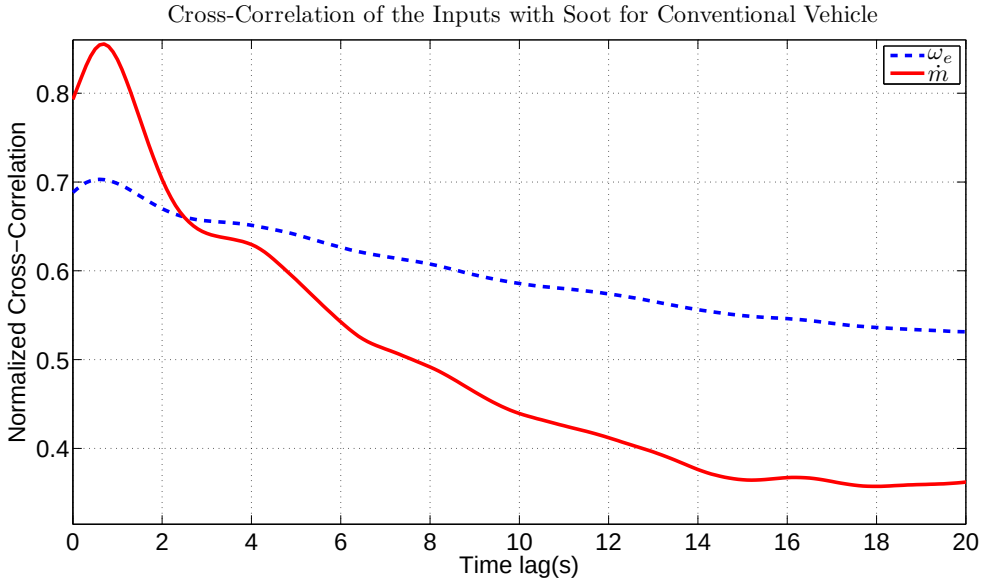

Figure 2.6: Time-lag for Peak Cross-correlations

where $y_n(t)$ is the 'n th-order output' of the system

$$y_n(t) = \int_{-\infty}^{\infty} \cdots \int_{-\infty}^{\infty} h_n^u(\tau_1, \tau_2, \ldots, \tau_n) \prod_{i=1}^{n} u(t - \tau_i) \mathrm{d}\tau_i, \quad n > 0 \tag{2.5}$$

where $h_n^u(\tau_1, \tau_2, \ldots, \tau_n)$ is called the 'n th-order kernel' or 'n th-order impulse response function' [149]. If $n = 1$, this reduces to the familiar linear convolution integral.

A discrete-time equivalent of Equation 2.4 can be expressed as

$$y(k) = \sum_{n=1}^{\infty} y_n(k) \tag{2.6}$$

where

$$y_n(k) = \sum_{-\infty}^{\infty} \cdots \sum_{-\infty}^{\infty} h_n^u(\tau_1, \tau_2, \ldots, \tau_n) \prod_{i=1}^{n} u(k - \tau_i), \quad n > 0, k \in \mathbf{Z} \tag{2.7}$$

Boyd and Chua [150] showed that this discrete time Volterra series can be approximated to the desired accuracy, if the non-linear operator $h_n^u(\cdot)$ is causal, continuous, time-invariant, and has fading memory, and if the inputs are bounded. This is the case for a wide-class of non-linear systems, unless they contain dynamic behaviors such as limit cycles, subharmonics, or chaos [151, 152]. An immediate consequence is that the higher order terms can be neglected in such a way that only the first M Volterra kernels need to be taken into account, where M is the order of the resulting model. Since the desired representation is stable, the elements of $h_n^u(\tau_1, \tau_2, \ldots, \tau_n)$ with $\tau_l > \varepsilon_n (\forall l \in 1, \ldots, n)$ can be ignored [153], and Eqn 2.6 simplifies to

$$y(k) = \sum_{n=1}^{M} \sum_{\tau_1=0}^{\varepsilon_n} \cdots \sum_{\tau_n=0}^{\varepsilon_n} h_n^u(\tau_1, \tau_2, \ldots, \tau_n) \prod_{i=1}^{n} u(k - \tau_i) \tag{2.8}$$

Once the Volterra series is established, the problem at hand reduces to finding the Volterra kernels. The main drawback here is that the kernels are, in principle, non-

parameterized functions whose measurement is possible only if their individual contributions can be separated from the total system response [154]. If the elements of all the Volterra kernels, $\mathbf{h} = [h_1, h_2, \ldots, h_m]^T$ where $m = \left(\frac{(\varepsilon_n + M + 1)!}{(\varepsilon_n + 1)!M!} - 1 \right)$, are treated as individual parameters to be estimated, and the Volterra model is linear in these parameters, classical estimation algorithms can be applied. This approach, however, can make the model over-parameterized. Hence orthonormal basis functions such as the Laguerre functions [154–156] and Kautz functions [153], as well as generalized orthogonal basis (GOB) functions [157] are often selected to expand the Volterra kernels, and to reduce the parametric complexity. However, the use of these basis functions requires some knowledge of the poles of the system, and implementing them for higher-order MISO systems is quite exhaustive. In this work we treat the elements of Volterra kernels as individual parameters, and reduce the parametric complexity using proper orthogonal decomposition (POD) [120, 136]. For the given input traces, the Volterra series input polynomials, $\prod_{i=1}^{n} u(k - \tau_i)$, are expanded using orthogonal basis vectors. Since these orthogonal basis vectors are a linear combination of the Volterra input polynomial vectors, their coefficients are also the same linear combination of the elements of the Volterra series kernels. Based on energy considerations, a reduced subspace can be constructed for these orthogonal bases, and the model's projection onto this reduced subspace reduces the number of parameters to be estimated. Linear regression is then used to calculate these coefficients from the experimental data.

A third-order dual-input, single output (DISO) Volterra-series was established for the identification of the transient soot. The order of the model was kept low to avoid fitting noise, and the time-history of less than one second was used based on the cross-correlation results presented in Section 3. The two inputs ($\dot{m}$ & ω_e, represented here as u_1 & u_2 for use of compact notations in Eqns. 2.9-2.11) were normalized by their maximum permitted values to get $\bar{u}_1, \bar{u}_2 \in [0, 1]$. As a result, the higher order

terms can be neglected and soot is approximated as the sum of the first three orders of the output. The three orders of the output for this DISO system are calculated as shown in Eqns. 2.9-2.11, where the superscript of the Volterra kernel represents the input associated with the kernel.

$$y_1(k) = y_1^{u_1}(k) + y_1^{u_2}(k) = \sum_{n_1=1}^{2} \sum_{\tau=0}^{\varepsilon_n} h_1^{u_{n_1}}(\tau) \bar{u}_{n_1}(k-\tau) \tag{2.9}$$

$$\begin{aligned} y_2(k) &= y_2^{u_1u_1}(k) + y_2^{u_1u_2}(k) + y_2^{u_2u_2}(k) \\ &= \sum_{n_1=1}^{2} \sum_{n_2=n_1}^{2} \sum_{\tau_1=0}^{\varepsilon_n} \sum_{\tau_2=0}^{\varepsilon_n} h_2^{u_{n_1}u_{n_2}}(\tau_1,\tau_2) \bar{u}_{n_1}(k-\tau_1) \bar{u}_{n_2}(k-\tau_2) \end{aligned} \tag{2.10}$$

$$\begin{aligned} y_3(k) &= y_3^{u_1u_1u_1}(k) + y_3^{u_1u_1u_2}(k) + y_3^{u_1u_2u_2}(k) + y_3^{u_2u_2u_2}(k) \\ &= \sum_{n_1=1}^{2} \sum_{n_2=n_1}^{2} \sum_{n_3=n_2}^{2} \sum_{\tau_1=0}^{\varepsilon_n} \sum_{\tau_2=0}^{\varepsilon_n} \sum_{\tau_3=0}^{\varepsilon_n} h_3^{u_{n_1}u_{n_2}u_{n_3}}(\tau_1,\tau_2,\tau_3) \bar{u}_{n_1}(k-\tau_1) \bar{u}_{n_2}(k-\tau_2) \bar{u}_{n_3}(k-\tau_3) \end{aligned} \tag{2.11}$$

Assuming the elements of each kernel are individual parameters, this results in a model with 470 parameters. In order to reduce the number of these parameters to be estimated, the Volterra input polynomials in Eqns. 2.9-2.11 are arranged in the columns of $\mathbf{A}$, with different rows corresponding to the data at different time samples. The columns of $\mathbf{A}$ are then mean centered and normalized by the standard deviation to scale the matrix and obtain $\bar{\mathbf{A}}$. Singular value decomposition is then performed to obtain the orthogonal matrices $\mathbf{U}$ and $\mathbf{V}$, and the matrix of singular values $\mathbf{\Sigma} = diag(\sigma_1, \sigma_2, \ldots, \sigma_n)$ with $\sigma_1 \geq \sigma_2 \geq \ldots \geq \sigma_n \geq 0$, as

$$\bar{\mathbf{A}} = \mathbf{U}\mathbf{\Sigma}\mathbf{V}^{\mathbf{T}} \tag{2.12}$$

The columns of the matrix $\mathbf{V}_{470\times470}$ form an orthogonal basis of the state space for the traces of Volterra input polynomials, and the squares of the singular values

provide a measure of how much signal energy is captured by each of these basis vectors. Let $\bar{\mathbf{h}} = [\bar{h}_1, \bar{h}_2, \ldots, \bar{h}_{470}]^T$ be the vector of the coefficients of the orthogonal basis vectors, representing linear combinations of the elements of the Volterra kernels $\mathbf{h} = [h_1, h_2, \ldots, h_{470}]^T$. Then, a reduced model is derived by considering only the first r dimensions of this vector, spanned by the first r columns of matrix $\mathbf{V}$, and denoted by $\mathbf{V_r}$. The new basis vectors are then calculated by projecting the system's model onto this subspace (Galerkin projection) as

$$\mathbf{\Phi} = \mathbf{A}\mathbf{V_r^T} \tag{2.13}$$

It was observed that the first 5 principal components captured 99.9% of the system's energy (Figure 2.7). Since this result is input dependent, additional modes were included to increase model confidence, and r was chosen as 25. Let Y denote the time trace of the transient soot recorded during experiments, $\bar{Y}$ the model estimate, and $\bar{\mathbf{h}}_\mathbf{r} = [\bar{h}_1, \bar{h}_2, \ldots, \bar{h}_r]^T$ the vector containing the r coefficients of the reduced model, then $\bar{Y} = \mathbf{\Phi}\bar{\mathbf{h}}_\mathbf{r}$, and the least-squares optimal solution for model identification, $\hat{\mathbf{h}}_\mathbf{r}$, is calculated as

$$\hat{\mathbf{h}}_\mathbf{r} = \arg\min_{\bar{\mathbf{h}}_\mathbf{r}} \|Y - \mathbf{\Phi}\bar{\mathbf{h}}_\mathbf{r}\|_2 \tag{2.14}$$

2.5 Model Validation Results

This section presents the validation of the model based on Volterra series, and compares the results with steady-state maps. Since 17 datasets of processed data were available for this work, identification of the model was performed using some datasets, and model validation exercises were carried out on the others. Model estimates for the validation datasets were obtained by projecting the Volterra input polynomials of the respective sets onto $\mathbf{V_r}$, and then multiplying them with the vector of new coefficients ($\hat{\mathbf{h}}_\mathbf{r}$) obtained during identification. A sample of the Volterra

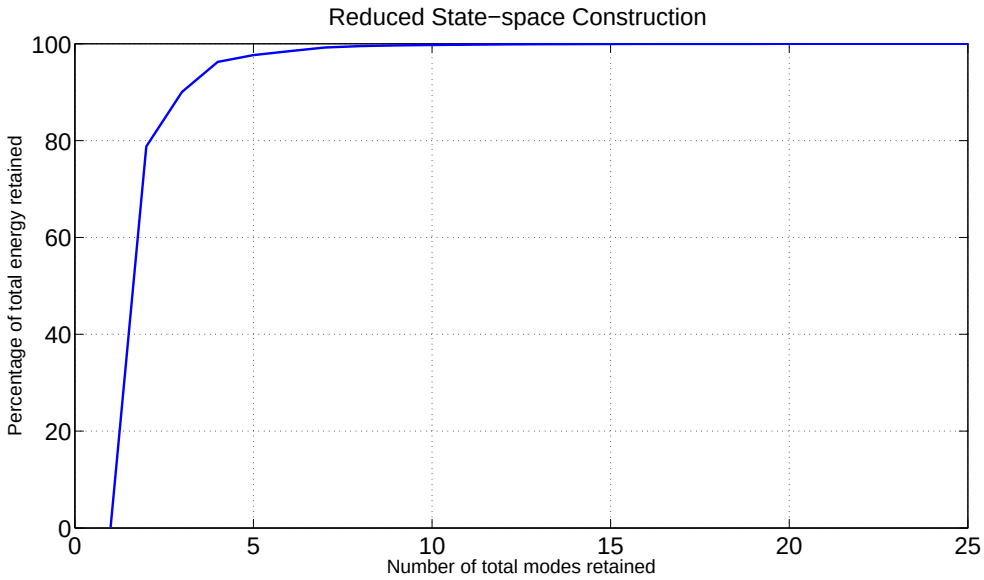

Figure 2.7: Energy based analysis for number of modes

series predictions is shown in Figure 2.8. It is observed that the identification done with highly transient datasets (conventional vehicle, downsized engine, parallel electric hybrid) improved the prediction accuracy during tip-in operations over steady-state maps. This is intuitive as when the driver presses the throttle in a drive-by-wire system, greater volume of fuel is injected into the cylinder to create more torque but the boost pressure lags behind due to turbocharger inertia, reducing the in-cylinder air-fuel ratios. The controller monitors this, and it limits the amount of fuel injected, nevertheless instantaneous excursions of air/fuel ratio and residual exhaust gas are quite probable. Additionally, the momentum of the incoming charge and the swirl intensity are reduced. This impedes the mixture preparation, and increases the heterogeneity of the mixture resulting in an overshoot in particulate and gaseous emissions [4, 17, 23]. None of these effects are captured by the steady-state maps because they are not memory based, and hence fall short of accurate soot predictions during transients.

The predictions were, however, biased for the steady-state operation. This disparity

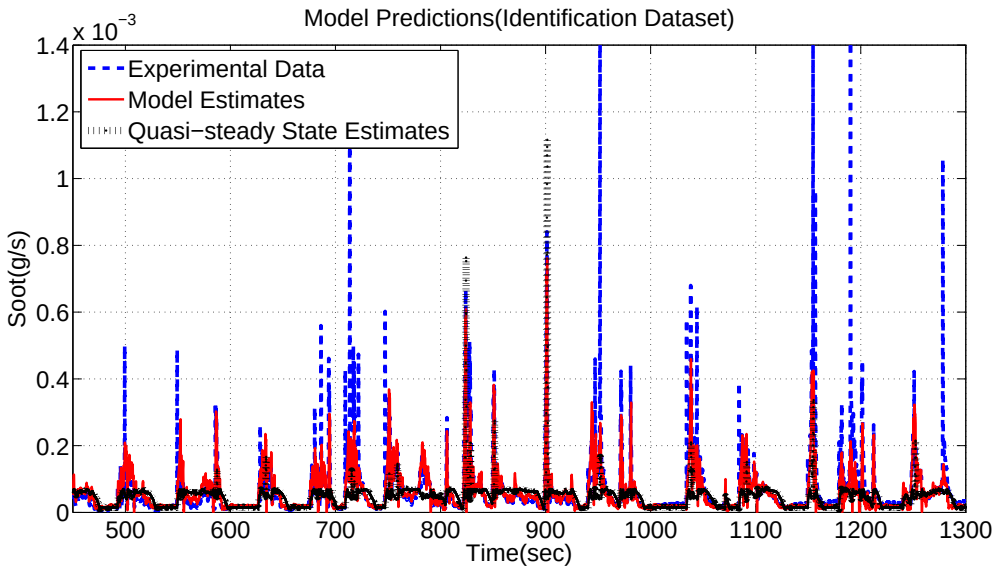

Figure 2.8: Volterra estimates for the identification dataset

can be explained by considering the physics of soot formation. As summarized in Appendix *A*, particle formation due to nucleation is predominant at low-load steady-state operations resulting in smaller spectral diameter of the particles. At transient loads, aggregation mode also contributes to the particle formation of bigger diameters [4, 23]. Since this Volterra series is identified using only FTP-75 data that contains limited amount of steady-state information, the predictions were slightly inaccurate. When identification was done using the data-set predominantly containing steady-state data (series hydraulic hybrid dataset), the bias at steady-state predictions was eliminated. In this case the accuracy over transient predictions deteriorated due to the lack of a sufficiently rich model during identification.

This problem was circumvented using datasets rich in both transient and steady-state information for identification. For this purpose, the conventional vehicle dataset was augmented by that of the series hydraulic hybrid, and coefficients were obtained that resulted in the least total error for both of these datasets. The improvements in steady state predictions are shown in Figure 2.9. Validation was then performed on different

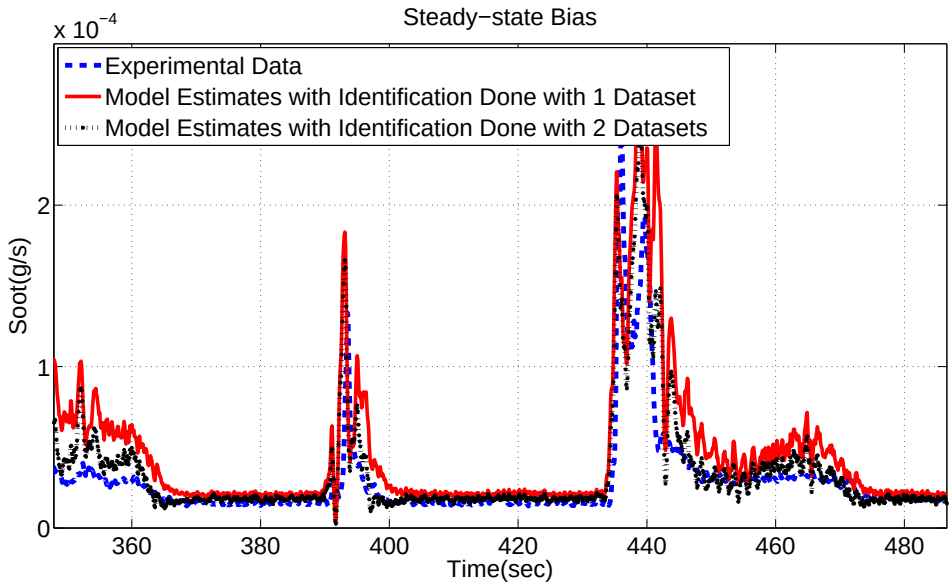

Figure 2.9: Steady-state bias for Volterra estimates

datasets, including electric and hydraulic hybrids with different control strategies, all producing different time traces of the inputs. Figure 2.10 shows the results for the validation of downsized engine data-set for part of the FTP-75 city cycle. The model estimates are compared with experimental data and quasi-steady state predictions obtained by using steady-state maps at the same inputs. As seen from the graph, the prediction accuracy with Volterra series improves substantially over the steady-state map during transients, whereas both the models match the experimental data at quasi steady-state operations.

2.5.1 Residual Analysis

A more structured approach to model validation can be adopted by the statistical analysis of the residuals [144], defined as $R = Y - \bar{Y}$. If the model captures all the dominant dynamics of the system, the residuals should closely resemble white noise. Figure 2.11 shows the autocorrelation of the residuals for a validation dataset. Also plotted is the 99% confidence interval for the autocorrelation of white noise

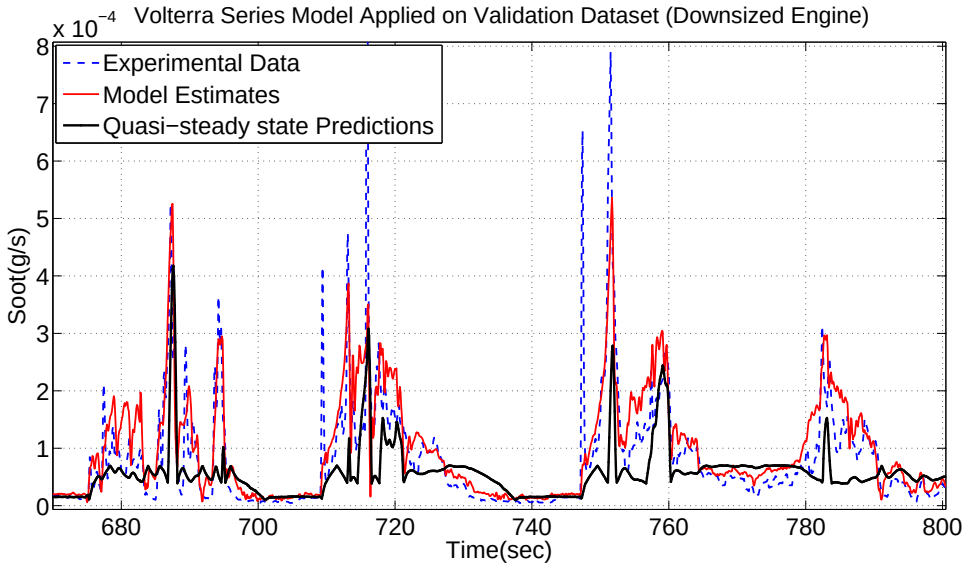

Figure 2.10: Volterra Estimates for the Validation Dataset

containing an equal number of samples $(13,601)$. The results are presented for low values of time lags as the time constants of the system are much smaller. Figure 2.12 shows the cross-correlation of the residuals with the inputs. Results show very weak correlations between the residuals and the input at low lags, indicating the presence of some unmodeled dynamics. Figure 2.13 elucidates this point by looking at the cross spectra of the residuals from Volterra series and that from quasi steady-state predictions. It can be seen that although there are some low frequency components present in Volterra series residuals, they are far less than those present in quasi steady-state residuals. This explains the difference in their performance in predicting soot during tip-in operations. The difference in their performance at 0Hz is attributed to the presence of noise and steady-state bias (Figure 2.9).

The selection of datasets for identification and validation was largely dictated by their dynamic content. Figure 2.14 shows the Volterra series based model's L_2 error norms, as well as the percentage reduction in these error norms over the results obtained using quasi-steady-state predictions. The choice of the identification dataset is shown

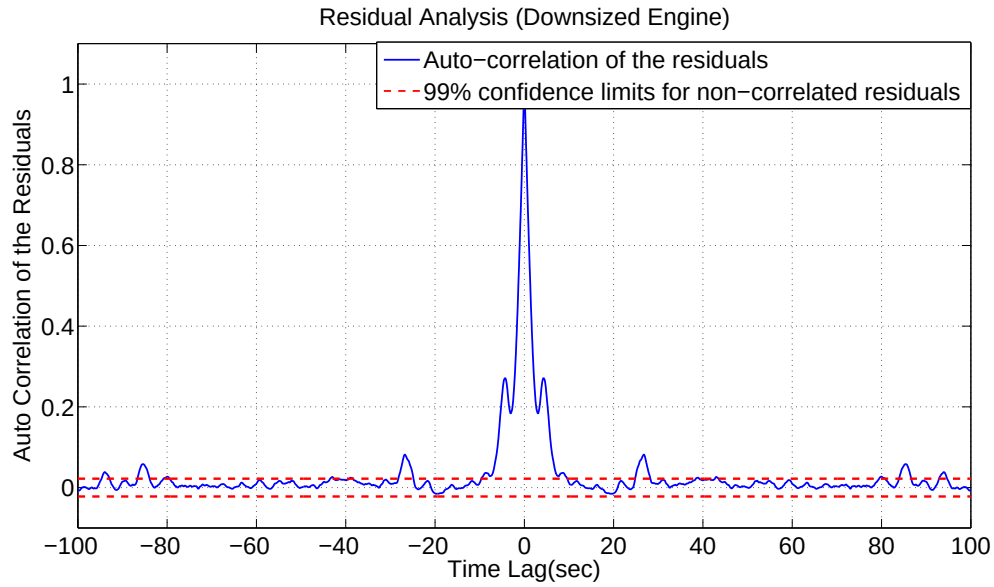

Figure 2.11: Autocorrelation of the residuals

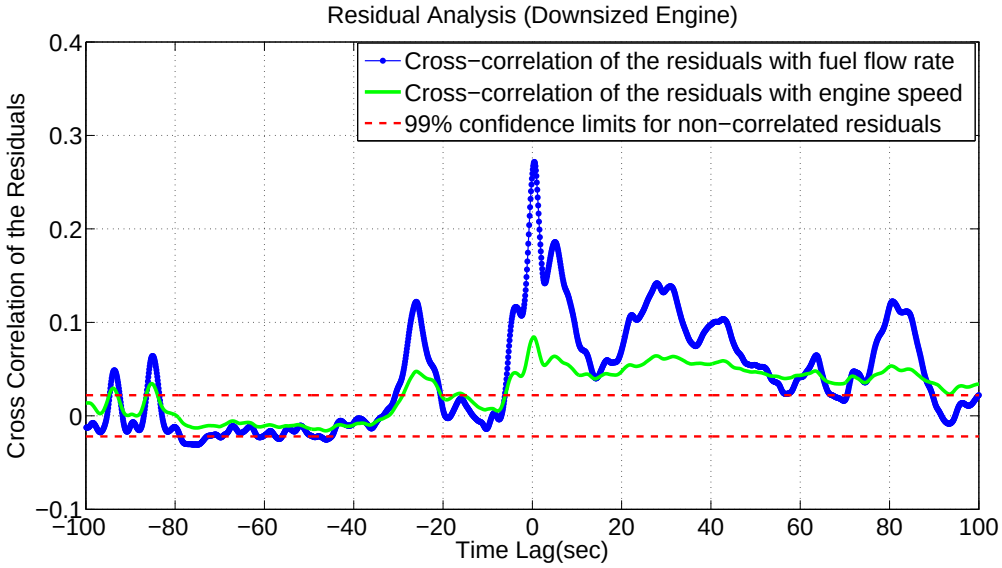

Figure 2.12: Cross-correlation of the residuals

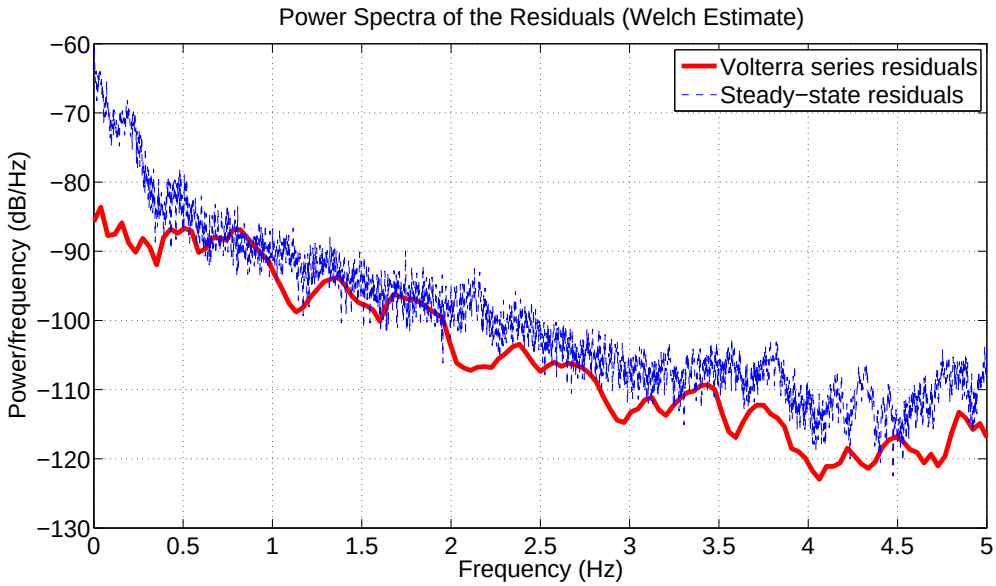

Figure 2.13: Cross spectra of the residuals (downsized engine)

first in every row, and the different columns present the validation results, with the diagonal entries representing the performances on the identification datasets. If the Volterra series error norm reduces over that of the quasi steady-state predictions, the entry is shown in green. If the error norm increases, the entry is shown in red and the model is not considered validated. It can be seen that with the exception of datasets 8 and 13, the model can be identified successfully using any of the datasets. These two datasets are unable to validate or identify soot as compared to the other datasets. This discrepancy can be introduced by a number of factors affecting the experiments, such as the lack of control of air humidity or an error in DMS calibration prior to the test run. Since the model works well with the other 15 datasets, irrespective of the choice of identification and validation datasets, it is assumed that these two datasets are erroneous. The improvements for the other 15 datasets depend on the content of transient information in the identification dataset. Identification done with rich transient datasets, while still augmenting them with series hydraulic hybrid dataset, demonstrate greater improvements. In this dissertation, datasets 1 and 15 (conventional vehicle and series hydraulic hybrid, respectively) are used for identification.

The percentage reductions in L_2 error norms for this choice are shown in Figure 2.15. As expected, the identification datasets show substantial improvements. All validation datasets, with the exception of datasets 8 and 13, produce improvements as well.

L2 Error norm																		
		Validation																
		Data1	Data2	Data3	Data4	Data5	Data6	Data7	Data8	Data9	Data10	Data11	Data12	Data13	Data14	Data15	Data16	Data17
SS error norm		0.010981036	0.010910806	0.022786848	0.020946244	0.02391803	0.027567079	0.027567079	0.007101664	0.021890795	0.009496225	0.027532386	0.013901001	0.00801268	0.013980573	0.006002766	0.007732403	0.004109274
ID	Data1 + 15	**0.008(26.9%)**	0.009(16.7%)	0.018(20.8%)	0.017(20.9%)	0.014(41.2%)	0.02(27.1%)	0.02(27.1%)	0.009(-21.4%)	0.017(20.2%)	0.008(19.6%)	0.026(4.9%)	0.013(6.3%)	0.01(-24.3%)	0.011(20.3%)	0.002(59.4%)	0.006(21.1%)	0.003(26.7%)
	Data2 + 15	0.009(20.1%)	**0.009(20.8%)**	0.017(24.2%)	0.018(16.1%)	0.017(28.2%)	0.022(20.9%)	0.022(20.9%)	0.009(-26.5%)	0.018(16%)	0.008(11.2%)	0.024(13.4%)	0.013(7.5%)	0.01(-25%)	0.011(22.6%)	0.002(66%)	0.005(29.4%)	0.003(29.8%)
	Data3 + 15	0.01(12%)	0.009(16.4%)	**0.013(41%)**	0.019(10.4%)	0.02(17.2%)	0.025(7.7%)	0.025(7.7%)	0.01(-44.5%)	0.023(-6.8%)	0.01(-7%)	0.026(6.7%)	0.013(5.8%)	0.017(-109.4%)	0.006(58.9%)	0.006(0.1%)	0.004(54.2%)	0.004(-4.6%)
	Data4 + 15	0.009(16.9%)	0.01(10.6%)	0.02(11.6%)	**0.014(32.5%)**	0.009(61.9%)	0.019(31.9%)	0.019(31.9%)	0.007(-2.8%)	0.017(24.1%)	0.009(9.7%)	0.027(0.9%)	0.013(3.9%)	0.01(-21.5%)	0.012(12.4%)	0.004(37.6%)	0.007(6.9%)	0.003(27.5%)
	Data5 + 15	0.01(12.7%)	0.01(6%)	0.021(9.4%)	0.015(26.8%)	**0.005(79.3%)**	0.019(32.1%)	0.019(32.1%)	0.006(17.7%)	0.018(17.7%)	0.008(16.5%)	0.031(-12.7%)	0.014(0.6%)	0.009(-14.8%)	0.013(10.4%)	0.004(38.3%)	0.008(0.8%)	0.003(35.4%)
	Data6 + 15	0.009(21.4%)	0.01(8.5%)	0.019(14.4%)	0.015(29%)	0.008(67.8%)	**0.018(35.7%)**	0.018(35.7%)	0.008(-8.9%)	0.015(29.3%)	0.008(13.3%)	0.028(-0.7%)	0.014(2.6%)	0.01(-21.1%)	0.012(12.8%)	0.003(42.4%)	0.007(3.4%)	0.003(20.9%)
	Data7 + 15	0.009(21.4%)	0.01(8.5%)	0.019(14.4%)	0.015(29%)	0.008(67.8%)	0.018(35.7%)	**0.018(35.7%)**	0.008(-8.9%)	0.015(29.3%)	0.008(13.3%)	0.028(-0.7%)	0.014(2.6%)	0.01(-21.1%)	0.012(12.8%)	0.003(42.4%)	0.007(3.4%)	0.003(20.9%)
	Data8 + 15	0.01(10.3%)	0.01(9%)	0.019(15.9%)	0.016(24.3%)	0.008(67.5%)	0.019(29.3%)	0.019(29.3%)	**0.005(24.9%)**	0.019(12.6%)	0.008(11.2%)	0.032(-14.9%)	0.014(1%)	0.01(-20.4%)	0.011(17.8%)	0.003(53.2%)	0.006(17.2%)	0.003(31.1%)
	Data9 + 15	0.009(16.7%)	0.011(1.5%)	0.02(12.1%)	0.015(26.9%)	0.011(54.6%)	0.018(33.9%)	0.018(33.9%)	0.01(-37%)	**0.015(32.9%)**	0.009(7.8%)	0.026(7.2%)	0.014(-1.3%)	0.009(-12.8%)	0.013(10.1%)	0.003(43.6%)	0.008(0.3%)	0.003(18.7%)
	Data10 + 15	0.008(23.8%)	0.009(14.2%)	0.019(17.8%)	0.016(25.9%)	0.009(63.1%)	0.019(31.6%)	0.019(31.6%)	0.007(0.1%)	0.018(19.7%)	**0.007(29.5%)**	0.029(-6.7%)	0.013(4.4%)	0.01(-19.2%)	0.012(16.8%)	0.003(54.6%)	0.007(12.5%)	0.003(25.2%)
	Data11 + 15	0.017(-50.6%)	0.017(-57.2%)	0.023(-1.6%)	0.022(-7.1%)	0.025(-3.4%)	0.026(4.2%)	0.026(4.2%)	0.018(-157.8%)	0.024(-7.7%)	0.019(-96.7%)	**0.019(32.7%)**	0.018(-30.5%)	0.012(-54.3%)	0.011(22.2%)	0.004(37.2%)	0.007(10.6%)	0.006(-56.6%)
	Data12 + 15	0.009(16.2%)	0.009(16%)	0.017(23.6%)	0.02(3.8%)	0.023(2.8%)	0.026(6.7%)	0.026(6.7%)	0.011(-53.1%)	0.023(-2.9%)	0.01(-4.2%)	0.024(13%)	**0.013(9.2%)**	0.01(-23.7%)	0.011(22.8%)	0.002(62.2%)	0.006(27.7%)	0.003(33%)
	Data13 + 1	0.008(24.9%)	0.009(14.2%)	0.024(-4.1%)	0.017(19.5%)	0.015(35.6%)	0.02(25.9%)	0.02(25.9%)	0.009(-27.2%)	0.017(21.8%)	0.008(19.4%)	0.027(2.1%)	0.013(5.6%)	**0.003(60.6%)**	0.018(-26.7%)	0.008(-31.7%)	0.012(-54.3%)	0.003(30.2%)
	Data14 + 1	0.009(19.2%)	0.01(12.9%)	0.014(38.9%)	0.02(6.8%)	0.02(18.1%)	0.026(6.1%)	0.026(6.1%)	0.01(-37.4%)	0.023(-5%)	0.009(1.3%)	0.03(-10.7%)	0.013(4.1%)	0.019(-136%)	**0.005(64.5%)**	0.008(-25.5%)	0.004(43.5%)	0.004(-3.3%)
	Data15 + 1	0.008(26.9%)	0.009(16.7%)	0.018(20.9%)	0.017(20.9%)	0.014(41.2%)	0.02(27.1%)	0.02(27.1%)	0.009(-21.4%)	0.017(20.2%)	0.008(19.6%)	0.026(4.8%)	0.013(6.3%)	0.01(-24.3%)	0.011(20.3%)	**0.002(59.4%)**	0.006(21.2%	0.003(26.7%)
	Data16 + 1	0.008(24%)	0.009(16.1%)	0.016(31.6%)	0.018(14.6%)	0.017(29.3%)	0.023(17.9%)	0.023(17.9%)	0.009(-25.9%)	0.02(8.9%)	0.008(12.4%)	0.027(0.3%)	0.013(6%)	0.014(-77.3%)	0.007(46.8%)	0.004(27.7%)	**0.003(56.8%)**	0.003(21.8%)
	Data17 + 1	0.008(27.1%)	0.009(16.5%)	0.02(12.2%)	0.017(21.1%)	0.014(39.9%)	0.02(28%)	0.02(28%)	0.009(-20.6%)	0.017(23.2%)	0.007(22.1%)	0.026(6.4%)	0.013(6.8%)	0.007(12%)	0.013(5.4%)	0.004(33.7%)	0.008(-0.7%)	**0.002(53.1%)**

Figure 2.14: Use of different datasets for identification

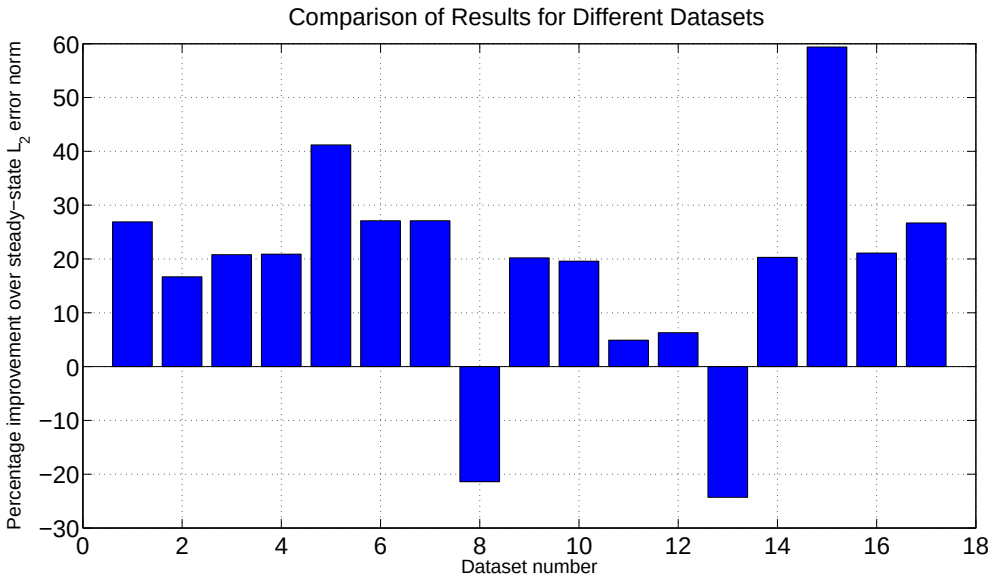

Figure 2.15: Performance comparison of different datasets

Figure 2.16 shows the results of improvements for the different configurations (identification and failed datasets not included). It can be seen that the model estimates are about 17%, and 21% more accurate than the quasi steady state predictions for conventional vehicle and downsized engine, respectively. Improvements are much higher for the hybrids, 41% for the parallel electric and 27% for the series hydraulic, as engine tip-in becomes more frequent. Overall, the models estimate soot both qualitatively and quantitatively better than steady-state maps by just using a 25 parameter third-order model, thus being computationally efficient and conducive to controls work.

2.6 Summary

This work presented the development of black-box transient soot models using Volterra series with only two inputs ω_e and $\dot{m}$. Based on the data, a third-order 25 parameter discrete-time Volterra series was developed, and validated. It was shown that the model estimated the transient soot significantly better than the steady-state

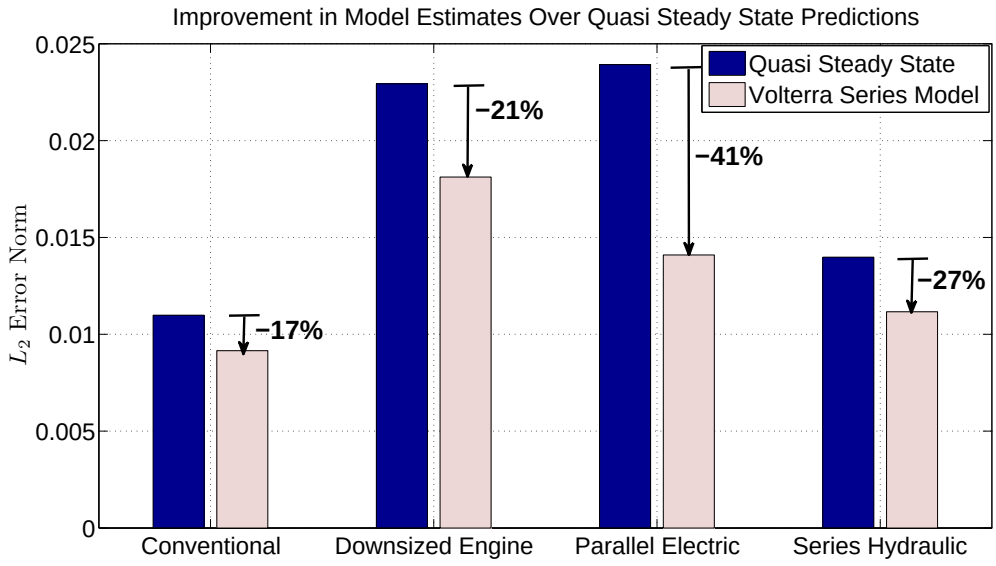

Figure 2.16: Reduction in L_2 Error Norms for Volterra Models

maps, both qualitatively and quantitatively, while still remaining computationally efficient. Development of this model, thus provides a valuable tool required for the offline powertrain control system development of conventional and diesel hybrid vehicles.

CHAPTER III

Iterative Learning Based Driver Input Synthesis

This chapter presents the synthesis of driver inputs for reducing diesel soot emissions using iterative learning control. Transient soot emissions from diesel engine vehicles are extremely sensitive to driver aggressiveness. Using closed-loop tracking controllers to model the driver for evaluating emissions over a prescribed drive cycle introduces driver-model induced variability in the results. This work develops an algorithm producing driver input traces that significantly reduces the soot emissions for a given cycle, thus providing a consistent basis for evaluating the influence of powertrain design changes on soot emissions. Possible improvements are first explored using conventional optimal techniques and results are obtained using linear programming. It is then shown that a first-order PD-type iterative learning control based algorithm can deliver better performance than linear programming, substantially reducing the total soot emissions at a fraction of the computational cost.

3.1 Introduction

In this chapter we seek to develop an algorithm for obtaining a driver input trace that produces minimum soot emissions from a diesel engine vehicle, while following the FTP drive cycle within EPA speed constraints. Transient soot produced by a turbo-charged diesel engine is extremely sensitive to the rate at which power is de-

manded from the engine [23, 55]. This high rate of power demand results in aggressive driving style. In the context of the longitudinal motion of an automatic transmission vehicle, the driver is primarily responsible for issuing throttle and brake commands. A more aggressive driver actuates a greater number of tip-in operations during which a greater volume of fuel is injected into the cylinder. The boost pressure lags behind due to turbocharger inertia, increasing the heterogeneity of the mixture, and resulting in an overshoot in particulate and gaseous emissions [10, 17]. When assessing these transient emissions for offline calibration and control system development, driver models are used to enable closed-loop simulation. Such driver models, when used for vehicle level analysis, often use a tracking controller with compensatory action with or without cycle preview [158, 159], and the gains of the controller are tuned to match the desired aggressiveness of the driver [2, 24]. However, there exists an infinite choice of controller gains capable of keeping the vehicle within EPA speed constraints, but each one producing significantly different soot emission results. Moreover, there is no intuitive way to scale these gains when porting the driver model to a different vehicle and/or powertrain configuration. This variable nature of driving greatly influences soot emission results [87]. To eliminate this driver model induced variability in emission evaluations and to enable an unbiased comparison of different powertrain designs, development of an algorithm for synthesizing driver inputs is proposed. This driving algorithm produces time traces of a standard driver actuator set: accelerator pedal and brake pedal positions, such that the performance objective (soot reduction) is maximized.

Seeking the driver actuator set produced by a trained driver, the literature offers techniques roughly belonging to two different categories: trajectory optimization techniques and learning based methods. Optimization based techniques can be further classified into the ones using static optimization methods such as sequential quadratic

programming (SQP) [81], and the ones using dynamic optimization techniques such as dynamic programming [52, 82]. Because of the simple pointwise nature, static optimization techniques are computationally more efficient but optimize the inputs for an instant in time instead of a time horizon. Dynamic optimization techniques consider the dynamic nature of the system and are generally more accurate under transient conditions. However these suffer from the curse of dimensionality, which exponentially increases the computational intensity with inputs and states [52]. Learning based techniques are computationally very efficient but generally do not guarantee optimality of the solution. Cao et al. [86] demonstrated the improvement in driver steering control input by updating the fuzzy logic in each iteration. Chen et al. [87] eliminated the driver based uncertainty during emission test results by using a robot driver that learns the performance of the vehicle during calibration and then uses the derived fuzzy logic rules to drive the vehicle. Additionally, instead of solving for a driver trace some researchers solve the inverse problem of optimizing the engine/vehicle calibration to driving style (e.g. automatic mode selection) to maximize the performance objective [82, 92].

In this work we reduce the soot emissions by developing the driving algorithm using iterative learning control (ILC). In order to compare the performance of the ILC based algorithm, the problem is also solved using a linear programming (LP) based approach. In this LP approach, the starting driver trace is produced by a PI controller that closely follows the FTP-75 cycle. The system is linearized, sensitivity functions are numerically calculated, and perturbations in driver pedal position are solved that yield the least total soot for the drive-cycle while subjected to various constraints. The process is then repeated iteratively until no appreciable improvement is detected. Then iterative learning control based driving algorithm is used to achieve the same task. A first order proportional-derivative (PD) controller is developed based on the

understanding of processes contributing to high soot formation, and the EPA constraint is implemented using a lower level controller. Total soot is then shown to monotonically decrease with the number of iterations. The results indicate that the ILC based algorithm outperforms the linear programming based solution while taking only a small fraction of computations. Improvements are only shown for the first 400sec of the FTP-75 city cycle but the numbers are quite representative of the entire cycle. Also, the techniques presented in this paper are general enough to be applied to various other performance objectives and powertrain configurations.

The rest of the chapter is organized such that the next section presents the engine, drivetrain and vehicle modeling details for this work. The following sections then describe the process of obtaining the optimal driver trace using linear programming, followed by the development of a driving algorithm based on iterative learning control. The final section outlines the summary and important conclusions of this chapter.

3.2 System Modeling

The block diagram of the system using a driving algorithm is shown in Figure 3.1. The driving algorithm is responsible for issuing driver accelerator and brake pedal positions. The solid and dashed lines indicate the flow of signals in the time domain, and the iteration domain, respectively. The soot performance for a given cycle is accounted by the driving algorithm only in the next iteration of simulation. The vehicle speed feedback for following the prescribed cycle may take place in the time or iteration domain depending upon the driving algorithm strategy. Once the algorithm converges, the iteration domain feedback disappears, thus making it a purely feedforward strategy for a given vehicle to follow a specific cycle. Hence, an implicit assumption in this work is that the system remains trial invariant.

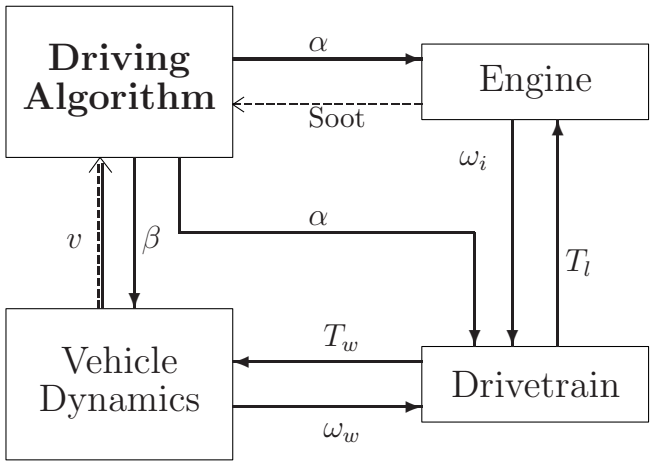

Figure 3.1: Model Structure for Vehicle Simulation

The modeling details of various vehicle level components are presented in Appendix C, and the variables in the block diagram correspond to those in Figure $C.5$. The soot emissions are modeled using Volterra series as presented in Chapter 2. This section presents the engine modeling details.

3.2.1 Engine Modeling

The engine model consists of three main components: a fuel control module, an engine torque map, and a transient soot model. The fuel control module is modeled as a PI controller that decides the fuel demand depending on the engine speed, the idle speed set-point, and the driver demand. The amount of fuel injected into the engine is controlled in a manner that is consistent with the driver pedal position except when engine conditions are such that the idle controller is necessary. Under these conditions, the idle controller engages and overrides the driver pedal position. The engine torque map takes fuel demand, as dictated by the fuel control module, and engine speed as inputs, and outputs the engine torque. The steady state engine map used for this purpose is shown in Figure 3.2. This engine torque is then used

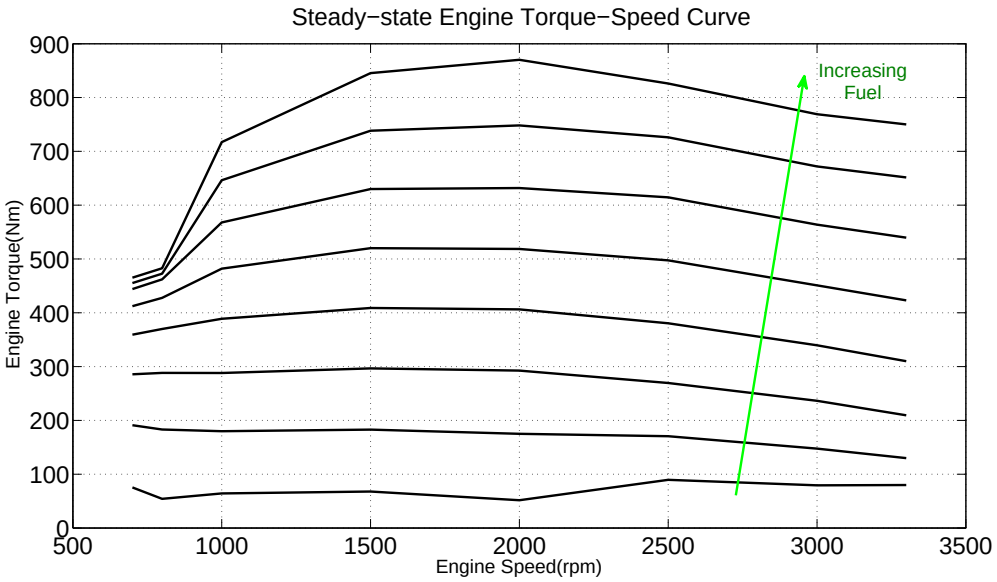

Figure 3.2: Steady-state engine map

to obtain the engine speed by accounting for the load torque, and the engine and impeller inertia [160].

The transient soot model uses inputs and produces output at 10Hz, whereas the complete vehicle model is integrated at a much higher frequency. Therefore, the inputs to this model are down-sampled and the outputs are held constant using zero-order hold (ZOH) to match the integration time-step.

3.3 Driver Trace Determination Using Linear Programming

This section presents the derivation of optimal driver trace using linear programming. The drivetrain and vehicle dynamics models in the simulation have 5 independent states, and the soot model (discrete time model at 10Hz) requires the past 10 input values (accelerator pedal position), and 10 engine state points (engine speed). Hence the number of input-state pairs does not computationally render this problem to the use of dynamic programming. Moreover each simulation runs in approximately

real-time and without parametrization of the driver input trajectory, it is too computationally intensive for static optimization methods. Hence, an iterative solution based on linear programming is proposed here. An initial solution set is obtained by the use of a PI tracking controller to closely follow the FTP-75 cycle. The linear programming (LP) problem is then defined to solve for small perturbations to this initial driver input such that the sum of perturbations in soot is minimized, while subjected to the EPA speed constraint. For the successful following of an FTP drive cycle, the EPA requires vehicle speeds to remain within 2 mph of the highest and lowest speeds within 1sec of the current time instant (EPA §86.116 − 90). This constraint limits the perturbations in the vehicle velocity and, hence, the perturbations in the driver command. For the linearization assumption to be valid, the permitted perturbation in the driver command is limited to 1%. Also, the negative perturbations in soot are limited such that a negative soot solution is not possible. The number of variables to be optimized are reduced by using ZOH in the driver input for 0.2sec. Figure 3.3 and 3.4 show the effect of using ZOH on various simulation variables. It can be seen that this approximation does not introduce any significant error in the problem. Therefore using this assumption, the problem of finding the optimal input set for the first 400sec of the FTP cycle reduces to a 2001 variable LP problem. Let the driver input be denoted by u, vehicle velocity by v, upper and lower EPA speed bounds at any instant of time as v_u and v_l respectively, and soot by y. Hence, the LP problem is stated as

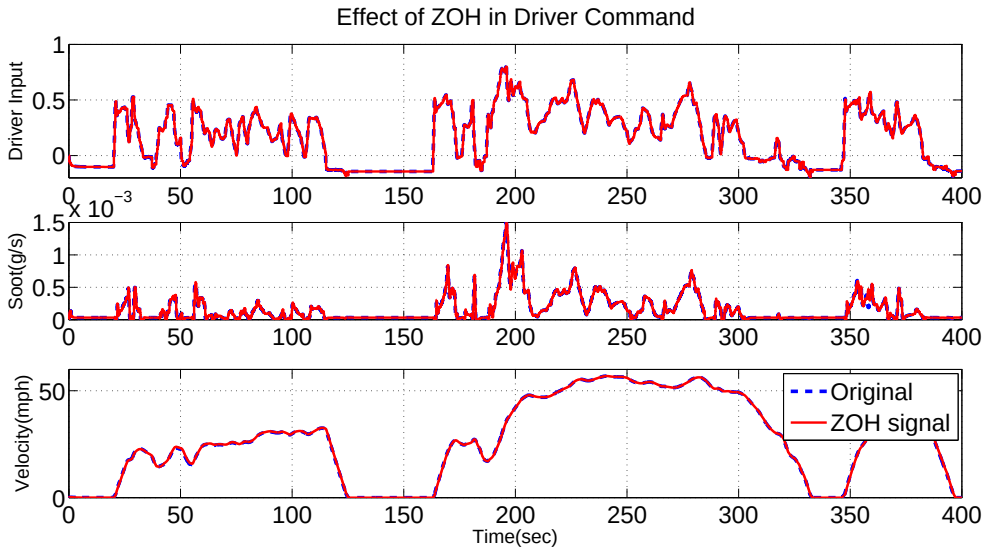

Figure 3.3: Effect of ZOH on simulation variables

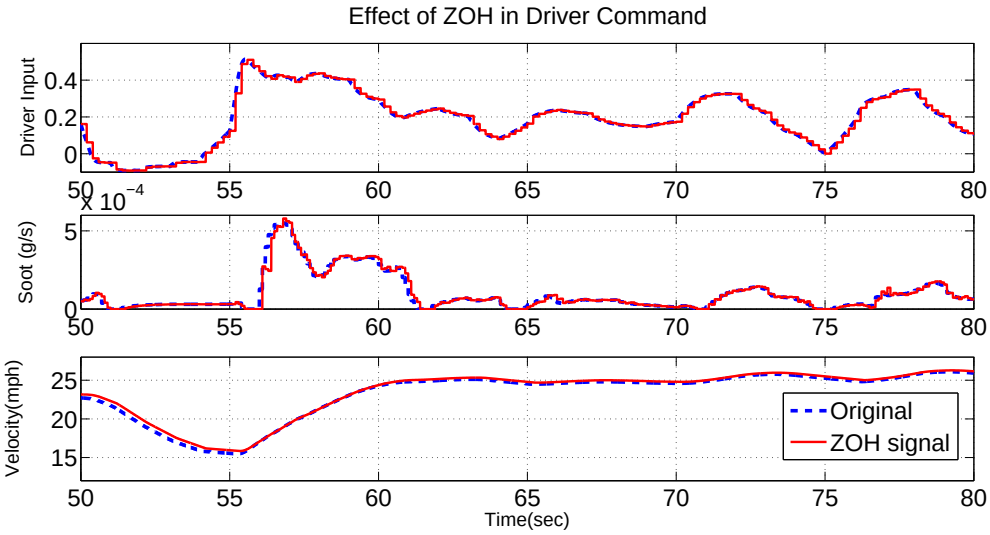

Figure 3.4: Effect of ZOH on simulation variables (magnified)

$$\min_{\mathbf{x}} \mathbf{f}^{\mathrm{T}}\mathbf{x} \tag{3.1}$$

$$\text{subject to :} \qquad \delta\mathbf{v_l} \leq \delta\mathbf{v} \leq \delta\mathbf{v_u}$$

$$-0.01 \leq \delta\mathbf{u}(i) \leq 0.01 \quad i \in [1, 2001]$$

$$\text{and} \quad -\mathbf{y} \leq \delta\mathbf{y}$$

$$\text{where,} \quad \mathbf{f}(i) = 1 \; \forall \, i \in [1, 2001], \text{ and } \mathbf{f}(i) = 0 \; \forall \, i \in [2002, 6003]$$

$$\mathbf{x} = [\delta y_0 \, \delta y_{0.2} \, \ldots \, \delta y_{400} \, \delta u_0 \, \delta u_{0.2} \, \ldots \delta u_{400} \, \delta v_0 \, \delta v_{0.2} \, \ldots \, \delta v_{400}]^{\mathrm{T}}$$

$$\delta\mathbf{v_l} = \mathbf{v_l} - \mathbf{v}, \text{ and } \delta\mathbf{v_u} = \mathbf{v_u} - \mathbf{v}$$

It is assumed that periods of engine idling exceeding 4sec resets all the vehicle states, and hence inputs are not calculated for idling after 2sec of vehicle rest until 2sec before vehicle motion. This further reduces the problem space, although the mathematical notation in this section does not reflect this assumption for brevity. Sensitivity of vehicle velocity and soot to changes in driver input is calculated numerically by perturbing only one input by 0.1% at an instant of time, and recording the change in outputs at each subsequent instant. Therefore, the variables satisfy the equality constraint

$$\mathbf{A_{eq}}\mathbf{x} = \mathbf{b} \tag{3.2}$$

$$\text{where} \quad \mathbf{A_{eq}} = \begin{bmatrix} \mathbf{I} & -\mathbf{S^T} & \mathbf{0} \\ \mathbf{0} & -\mathbf{R^T} & \mathbf{I} \end{bmatrix} \tag{3.3}$$

$$\mathbf{b}(i) = 0 \quad \forall \, i \in [1, 2001] \tag{3.4}$$

$$\mathbf{S} = \begin{bmatrix} \frac{\partial y_0}{\partial u_0} & \frac{\partial y_{0.2}}{\partial u_0} & \cdots & \frac{\partial y_{400}}{\partial u_0} \\ \frac{\partial y_0}{\partial u_{0.2}} & \frac{\partial y_{0.2}}{\partial u_{0.2}} & \cdots & \frac{\partial y_{400}}{\partial u_{0.2}} \\ \vdots & \vdots & \ddots & \vdots \\ \frac{\partial y_0}{\partial u_{400}} & \frac{\partial y_{0.2}}{\partial u_{400}} & \cdots & \frac{\partial y_{400}}{\partial u_{400}} \end{bmatrix} \tag{3.5}$$

$$\mathbf{R} = \begin{bmatrix} \frac{\partial v_0}{\partial u_0} & \frac{\partial v_{0.2}}{\partial u_0} & \cdots & \frac{\partial v_{400}}{\partial u_0} \\ \frac{\partial v_0}{\partial u_{0.2}} & \frac{\partial v_{0.2}}{\partial u_{0.2}} & \cdots & \frac{\partial v_{400}}{\partial u_{0.2}} \\ \vdots & \vdots & \ddots & \vdots \\ \frac{\partial v_0}{\partial u_{400}} & \frac{\partial v_{0.2}}{\partial u_{400}} & \cdots & \frac{\partial v_{400}}{\partial u_{400}} \end{bmatrix} \tag{3.6}$$

Since the system is causal the sensitivity of the output trace to the change in input at any given time would be zero for all times preceding that instant. Therefore, $\frac{\partial v_p}{\partial u_q} = 0$ and $\frac{\partial y_p}{\partial u_q} = 0 \; \forall \, q > p$. Also, since the system has fading memory [161], it is assumed that outputs after 50sec are not affected by a perturbation in the input at a given instant of time. Thus, $\frac{\partial v_p}{\partial u_q} = 0$ and $\frac{\partial y_p}{\partial u_q} = 0 \; \forall \, p - q > 50$. This assumption simplifies the problem structure further and allows multiple sensitivity function evaluations during a single simulation run. Another implicit assumption in formulating this as a linear programming problem is that the model remains continuous during perturbation i.e. no new gear shift events take place during the perturbation.

This problem was solved using Simplex algorithm to minimize the sum of total soot, and iterated with the previous solution as the starting point for the sensitivity evaluation. During each iteration, the solution of the LP problem was used in the original non-linear problem to calculate the improvement in total soot and check for possible constraint violations. If constraints were found to be violated at any instant of time, the LP problem was re-solved with tightened constraints at that instant of time. The

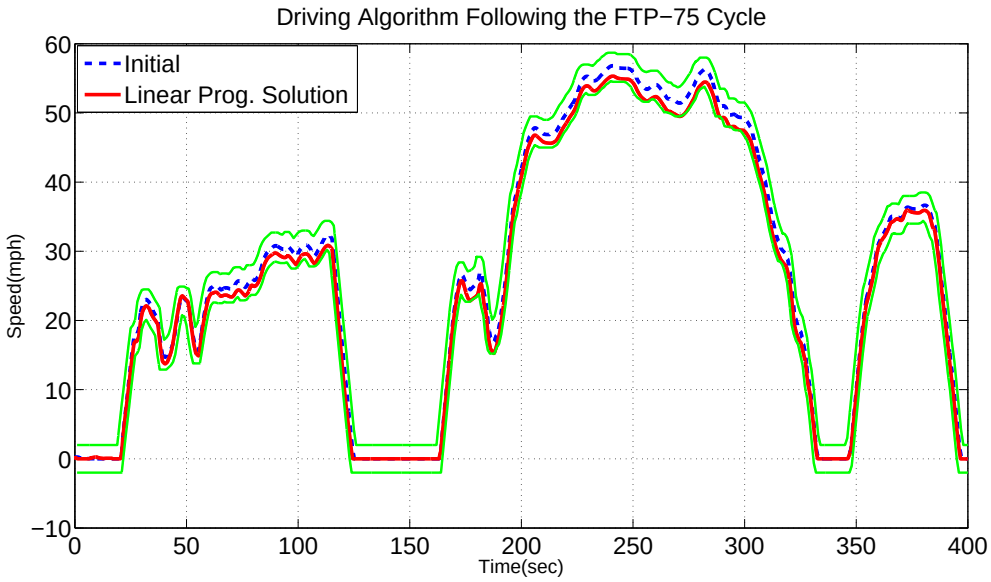

Figure 3.5: LP solution for min soot problem

iterative process of LP was continued until three consecutive iterations yielded less than one percent improvements .

This process resulted in total soot reduction of 8.63%. The resultant vehicle velocity trace is shown in Figure 3.5, with the EPA speed bounds marked. The improvement with different iterations is shown in Figure 3.6, and Figure 3.7 shows the transient soot profile for the solution. From Figure 3.5, it can be seen that the solution, for a large part, lies on the lower velocity bound. This solution suggests that lower vehicle velocity, which in turn implies lower engine speed, will result in least soot. This is true as lower engine speeds will see fewer combustion cycles per second. However, the bulk of soot contribution is from transient components, where during tip-in operations greater volume of fuel is injected into the cylinder to create more torque, but the turbocharger inertia prevents boost pressure from rising instantaneously. This reduces the in-cylinder air-fuel ratios, and the momentum of the incoming charge and the swirl intensity are reduced. This impedes the mixture preparation, and increases the heterogeneity of the mixture resulting in an overshoot in the soot emissions [17, 23,

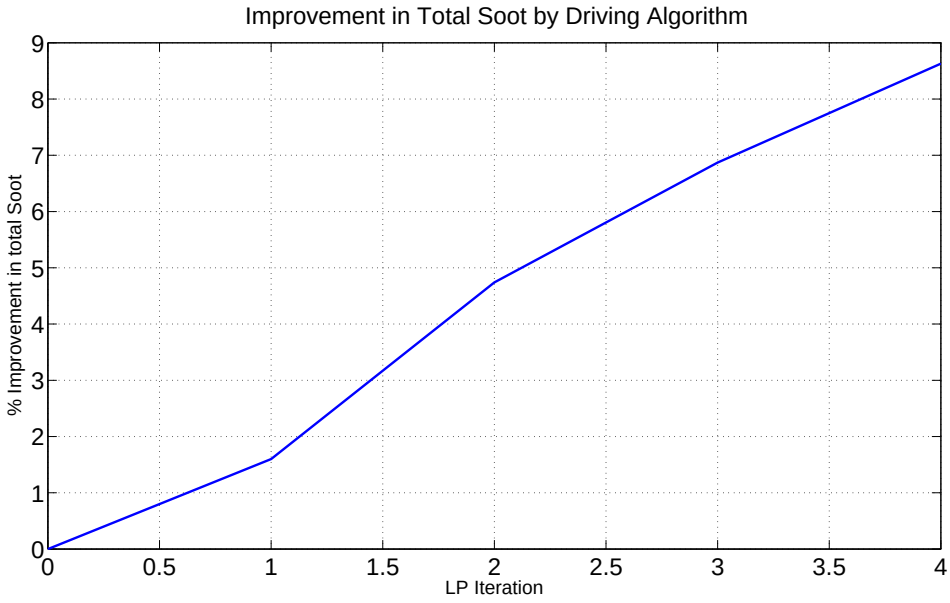

Figure 3.6: Reduction of total soot with iteration

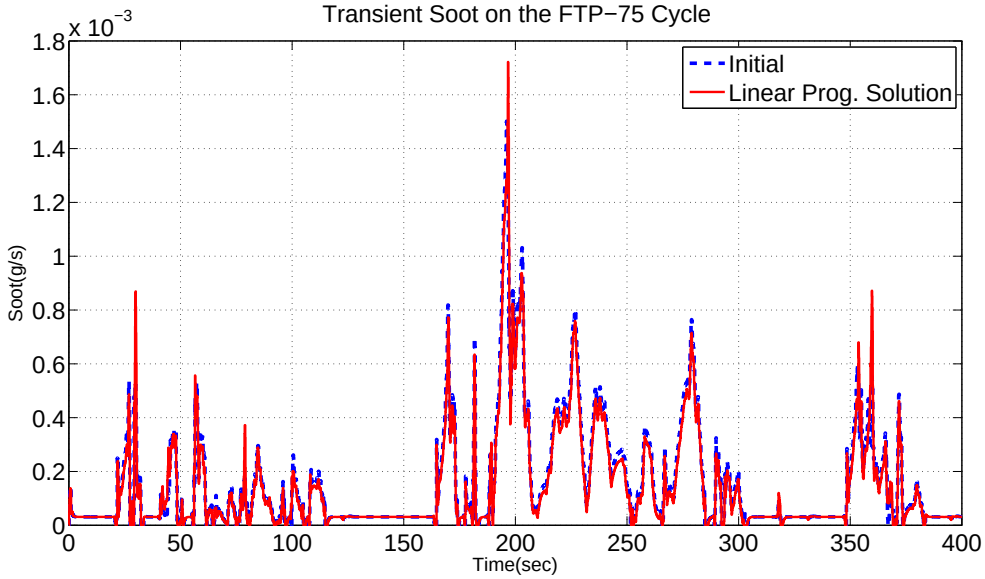

Figure 3.7: Reduction of transient soot for minimum soot problem

161, 162]. The Volterra series used for estimating soot here [161] is able to capture this effect. However, when the sensitivity functions are calculated by perturbing the input by 0.1%, it did not result in any appreciable change in engine acceleration, hence not capturing acceleration induced soot spikes in the LP problem. This problem is circumvented by defining an alternate problem: minimizing the sum of positive vehicle accelerations. Let us first define a function $\kappa(\cdot)$ as

$$\kappa(x) = \begin{cases} x & \forall\, x \geq 0 \\ \\ 0 & \forall\, x < 0 \end{cases} \tag{3.7}$$

Let $\dot{v}$ denote the vehicle acceleration, then the alternate LP problem can be redefined with a different $\mathbf{x}$ and $\mathbf{A_{eq}}$ as,

$$\min_{\mathbf{x}} \mathbf{f}^{\mathrm{T}}\, \kappa(\mathbf{x}) \tag{3.8}$$

$$\mathbf{x} = [\delta\dot{v}_0\, \delta\dot{v}_{0.2}\, \ldots\, \delta\dot{v}_{400}\, \delta u_0\, \delta u_{0.2}\, \ldots \delta u_{400}\, \delta v_0\, \delta v_{0.2}\, \ldots\, \delta v_{400}]^{\mathrm{T}}$$

$$\text{where} \quad \mathbf{A_{eq}} = \begin{bmatrix} -0.2\mathbf{I} & \mathbf{0} & \mathbf{B} \\ \mathbf{0} & -\mathbf{R^T} & \mathbf{I} \end{bmatrix} \tag{3.9}$$

where B is the lower triangular Toepliz matrix,

$$\mathbf{B} = \begin{bmatrix} 1 & 0 & 0 & \dots & 0 \\ -1 & 1 & 0 & \dots & 0 \\ 0 & -1 & 1 & \dots & 0 \\ \vdots & \vdots & \vdots & \ddots & \vdots \\ 0 & 0 & 0 & \dots & 1 \end{bmatrix} \tag{3.10}$$

The improvements in total soot with each iteration of LP are shown in Figure 3.8. After 5 iterations a total soot reduction of 13.4% was achieved. Figure 3.9 shows the vehicle speed trace for this solution. This solution tries to minimize the number and amount of positive accelerations by cutting corners within the speed bounds, and avoiding steep accelerations. As a result, transient soot is substantially reduced compared to the initial driver input set. The comparison of soot traces is shown in Figure 3.10. The solution is still computationally expensive due to hundreds of simulation runs required for calculating sensitivity matrices during each iteration, but can provide us with a systematic procedure for reducing soot by altering the driving style for any given vehicle-powertrain configuration.

3.4 Synthesis Using Iterative Learning Control

This section presents the synthesis of driver inputs using iterative learning control. ILC is based on the notion that the performance of a system that executes the same task multiple times can be improved by learning from previous executions [137]. Therefore, it produces a feedforward control that tracks a specific reference or rejects a repeating disturbance by using the error information from previous iterations, whereas non-learning controllers would yield the same error on each pass [137, 163]. This methodology has several advantages over well designed feedback and feedforward controllers. Feedback controllers introduce lag in transient tracking,

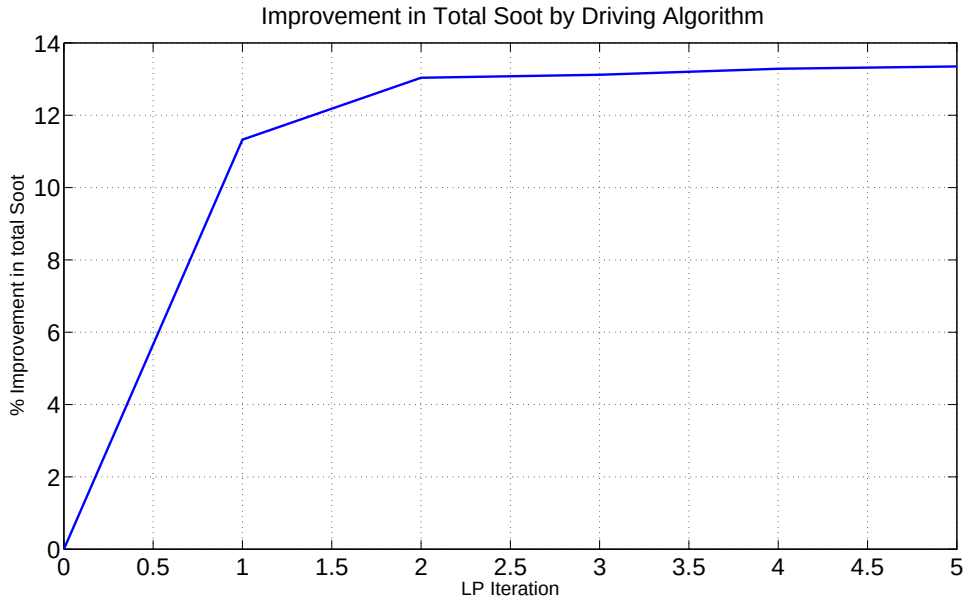

Figure 3.8: Improvement in total soot with LP

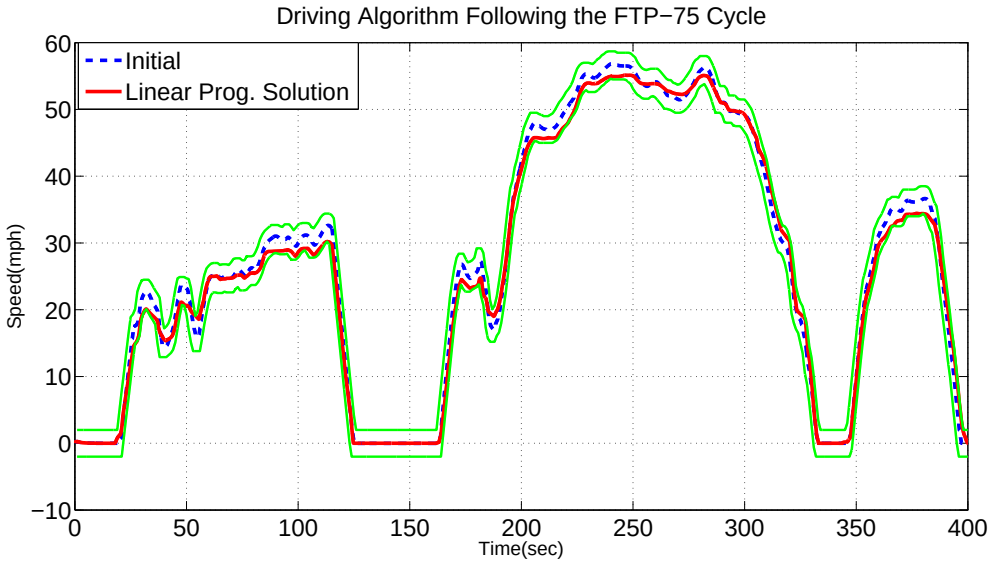

Figure 3.9: LP solution for minimum acceleration problem

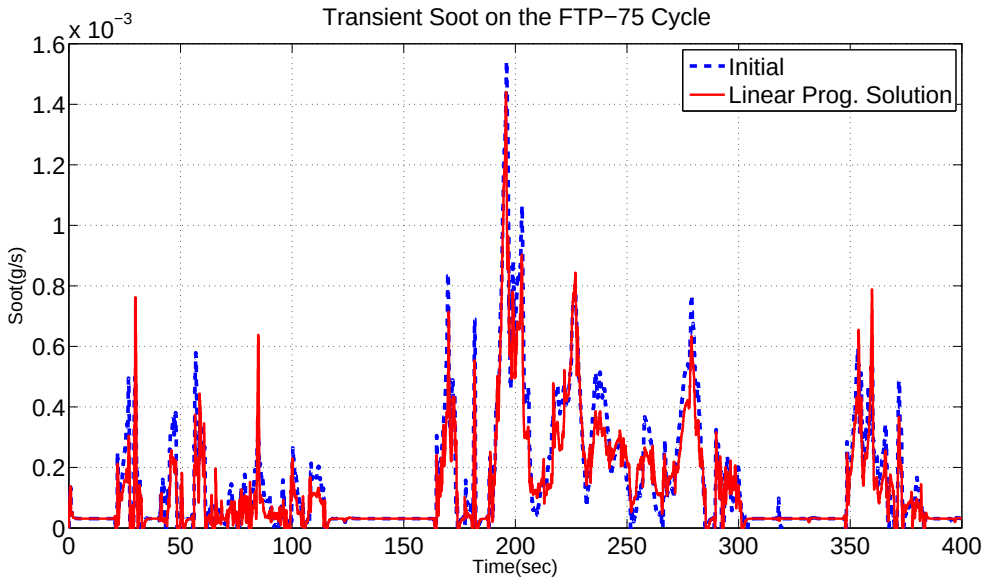

Figure 3.10: Soot trace comparison

while feedforward controllers can eliminate this lag for measurable signals, but fail to accommodate the variations or uncertainties in the system model, and perform well only to the extent the system is known [137, 164]. ILC is an open loop scheme that combines the benefits of feedback and feedforward control by having a feedback loop on the control signal in the iteration domain.

ILC requires that the system is trial invariant and resets to the same initial conditions after each iteration [163]. Thus ILC can readily be applied to time-varying and non-linear systems as long as they remain trial invariant. Let e be the error signal to be reduced, and u the control input with subscripts denoting the time index and superscripts denoting the iteration index, then a widely used first-order linear ILC algorithm can be defined as

$$u_k^{j+1} = u_k^j + L(q) * e_{k+1}^j \tag{3.11}$$

where $L(q)$ is the learning function and q is the forward time-shift operator $qx_k =$

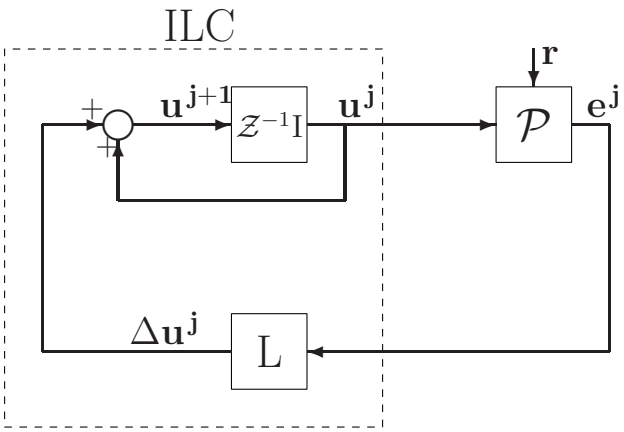

Figure 3.11: Feedback loop in the iteration domain

x_{k+1}. Let us define one trial delay operator, $\mathcal{Z}^{-1}$, as

$$u_k^j = \mathcal{Z}^{-1} u_k^{j+1} \tag{3.12}$$

Then the block diagram for Equation 3.11 can be drawn as shown in Figure 3.11 [163]. The trial invariant plant, $\mathcal{P}$, produces error, e_k^j, when tracking a trial invariant signal r. The learning law consists of a linear mapping (linear ILC) from the error to the change in control input. The control input for the next iteration, u_k^{j+1}, is obtained by adding this change in control input to the input from the previous iteration. Thus, ILC represents feedback in the iteration domain with a built-in integrator. Also, since error signal from only one previous iteration is utilized, this is a first order ILC. The block diagram in Figure 3.11 is labeled using lifted systems representation, where signals are vectorized (lifted) to include values at all instants of time and feedback in the iteration domain takes the form of a MIMO controller.

The purpose of the ILC is to find $\mathbf{u}^* = \lim_{j\to\infty} \mathbf{u^j}$, such that $\lim_{j\to\infty} \mathbf{e^j} = \mathbf{0}$, if there exists an input that can give perfect tracking. If this is not the case, the algorithm converges to $\mathbf{u}^*$, where $\mathbf{u}^*$ is the solution of the optimization problem

$$\mathbf{u}^* = \arg\min_{\mathbf{u}} \|\mathbf{e}\|^2 \tag{3.13}$$

where $\|\cdot\|$ is a suitable norm [165]. Therefore, the ILC problem is analogous to iterative optimization techniques as it relies on underlying repetitive process to minimize an objective function, except it can also use the data collected during the online trials [166]. Thus, ILC derives the output by learning the best possible inverse of the system dynamics for a given trajectory [167] and requires much less computational power as the feedforward signal is calculated off-line [168].

In order to find the driver input trace that produces the least soot emissions over the FTP cycle, the problem is formulated in the ILC framework. Since soot, $y_k \in [0, \infty)$ and the objective is to minimize soot, the soot output is regarded as the error. Volterra series model [161] is used for predicting the soot and the ILC technique is applied in pure simulation, although the proposed method can readily be applied to a vehicle on chassis dynamometer. As with the LP approach, the driver input trace obtained from a PI controller closely following the FTP cycle is used as the control input in the first iteration. Since there is a clear correlation between the control input (driver pedal position) and the error (soot), this problem can be tackled using a PD-type ILC. PD-type is one of most widely used learning functions, particularly for non-linear systems [137, 167, 169]. Let $Q(q)$ represent the $Q - filter$, K_p the proportional gain, and K_d the derivative gain, then ILC law for our system can be expressed as,

$$u_k^{j+1} = Q(q) * [u_k^j + K_p \cdot y_{k+1}^j + K_d \cdot \kappa(y_{k+\lambda+1}^j - y_k^j)] \tag{3.14}$$

where $\lambda = \dfrac{T_{soot}}{T_{veh}}$, T_{soot} being the update period for the soot model (0.1sec) and T_{veh} the integration time-step for the vehicle model (0.004sec). The integral term is not used for the learning function because ILC has a natural integrator action from one trial to

the next. The gains are tuned based on physical insight into the system. Higher engine speeds produce more soot (more combustion cycles per sec), and hence reducing soot through proportional gain requires less accelerator actuation and therefore the gain is negative. The derivative gain reduces the spikes in soot emissions and is active only when there is an increase in soot emissions. This gain is also negative, as more benign accelerations would reduce these spikes. Since transient soot is responsible for the bulk of the soot produced, magnitude of K_d is chosen to be much higher than K_p. The soot spikes from the simulation data are defined using the parameter λ. Since the complete model is integrated at 250Hz while the soot model is updated at 10Hz, this parameter in the ILC law is necessary to update the input that would actually affect the soot output. The described ILC formulation thus works on 10001 control input points (u) for the first 400sec of the FTP cycle, one for each integration time step. Also, since the gains are chosen based on physical principles, the formulation is quite robust to the change in model parameters as long as the system remains trial invariant.

The control input for the next iteration is calculated by the convolution of this updated input with the Q-filter. Q-filters are employed to determine which frequencies are emphasized in the learning process as there will be frequencies for which the system model is inaccurate. It helps to achieve monotonic convergence by disabling learning at high frequencies and provides the benefits of added robustness and high frequency noise filtering [137]. For a given Q-filter, when filter type and order are specified, the bandwidth of the filter can also be used as a tuning parameter. While learning gains influence the rate of convergence, the Q-filter influences the converged error performance. Increasing the Q-filter bandwidth decreases robustness but improves performance, whereas decreasing the bandwidth has the opposite effect [137].

In our work, a zero-phase non-causal FIR Gaussian lowpass filter [137, 170] with the

bandwidth of 10Hz is used. Since the goal is to lowpass filter the signals used in feedforward update, zero phase lag must be introduced. Also, since the update is done in between the iterations when signal information is available for all times, the non-causal nature of the filter does not pose any problems. Let the input calculated from learning for a continuous time system, but before being filtered, be represented by $\widetilde{u}^{j+1}(t)$, i.e. $\widetilde{u}^{j+1}(t) = [u^j(t) + L(s) * e^j(t)]$, $t \in [t_0, t_0 + T]$ where T is the total cycle (simulation) time, and let s be the Laplace operator, then $Q(s)$ can be defined by the integral transform

$$\begin{aligned} u^{j+1}(t) &= Q(s) * \widetilde{u}^{j+1}(t) \\ &= \int_{t-T}^{t+T} \Gamma(t,\tau)\widetilde{u}^{j+1}(t)\,\mathrm{d}\tau \end{aligned} \tag{3.15}$$

Since in this investigation we use a Gaussian filter, the kernel $\Gamma(t,\tau)$ is chosen as the Gaussian distribution function

$$\Gamma(t,\tau) = \frac{1}{\sigma\sqrt{2\pi}} \cdot e^{-\frac{(t-\tau)^2}{2\sigma^2}} \tag{3.16}$$

where the standard deviation parameter σ can be specified to get the desired bandwidth. To implement this filter in discrete time, the integral transform of Equation 3.15 is implemented as a non-causal digital filter using moving weighted average of data points in the feedforward signal vector [170]. Therefore, for our system the filter takes the form

$$
\begin{aligned}
u_k^{j+1} &= Q(q) * \widetilde{u}_k^{j+1}, \qquad k \in \left[p+1, \frac{T}{T_{veh}} - p\right] \\
&= \frac{\gamma_0 \widetilde{u}_k^{j+1} + \sum_{i=1}^{p} \gamma_i (\widetilde{u}_{k-i}^{j+1} + \widetilde{u}_{k+i}^{j+1})}{\gamma_0 + 2\sum_{i=1}^{p} \gamma_i}
\end{aligned} \tag{3.17}
$$

Hence, $(p+1)$ number of filter coefficients are used, obtained from the Gaussian distribution function in Equation 3.16. The only requirement is $2p \cdot T_{veh} \ll T$. Since ILC reduces the driver accelerator actuation, the constraint of following the drive cycle must be implemented explicitly. For this purpose, a lower level variable structure PI controller is implemented to follow the velocity profile ϵ mph within the EPA constraints, where ϵ is a very small velocity. The controller becomes active when the vehicle velocity comes closer than ϵ to the speed bounds. It then alters the ILC produced driver control input to keep the speed within the constraints. The gains are tuned such that during the simulation, the transient response does not overshoot ϵ, thus following the speed constraint at all times. Let K_p^c and K_i^c be the constraint controller gains, then the structure of the controller is defined as

$$
\text{PI Controller} : \begin{cases} K_p^c = 0, K_i^c = 0 \quad \text{if} \quad v_l + \epsilon \leq v \leq v_u + \epsilon \\ \\ K_p^c \neq 0, K_i^c \neq 0 \quad \text{if} \quad v_l + \epsilon \geq v, \text{ or } v \geq v_u + \epsilon \end{cases}
$$

The control input is bounded as well, $u \in [-1, 1]$, and the bounds are implemented using saturation functions with anti-windup loops.

The results for the ILC based driving algorithm are presented in Figs. 3.12-3.16. With approximately 40 iterations, an improvement of 18.8% was seen after which no sub-

stantial improvement was detected. This improvement is about 8% higher than one of the most intuitive solution: vehicle follows exactly the lower EPA speed constraint using a PI controller. Attempts were made to incorporate further improvements in the results by increasing the period over which soot spikes are defined, but it did not result in any substantial improvement. Figure 3.13 shows the vehicle speed trace on the FTP cycle and Figure 3.14 shows a magnified view of the first speed hump. It can be seen that the solution tries to minimize both the positive vehicle acceleration as well as the vehicle speed. As a result, minor speed humps are avoided and acceleration is much more gradual on longer speed humps. This is partly achieved by a head start when possible. Also, since part of the objective is to reduce soot through speed reduction, a large part of the lower speed constraint is active. Figure 3.15 and Figure 3.16 show the soot trace and driver actuation comparison, respectively. The traces with ILC show reduced transient soot for most of the cycle, resulting in an overall substantially lower soot. There are, however, a few instances where transient soot is actually increased. For example, when due to decreases in accelerator pedal position the shift logic downshifts, and hence more acceleration is required to follow the drive cycle or the constraint controller is actively trying to keep the vehicle speed within the constraints. In spite of these few unexpected soot increases, the ILC based driving algorithm gives very good performance with just 40 simulation runs. Comparison to other intuitive solutions, such as the one that calculates the minimum acceleration path for the FTP cycle within EPA speed limits independent of the vehicle and uses a PI controller to follow vehicle on that speed path, is left for future work.

3.5 Summary

This chapter presented the synthesis of driver inputs to reduce transient diesel soot emissions in an offline setting using iterative learning control. The soot reduc-

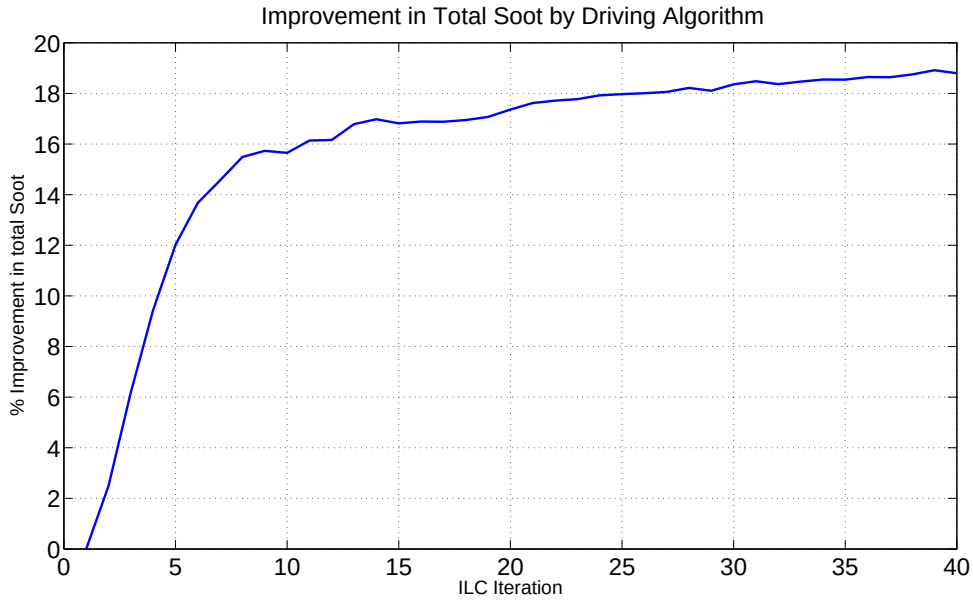

Figure 3.12: Soot reduction with ILC iterations

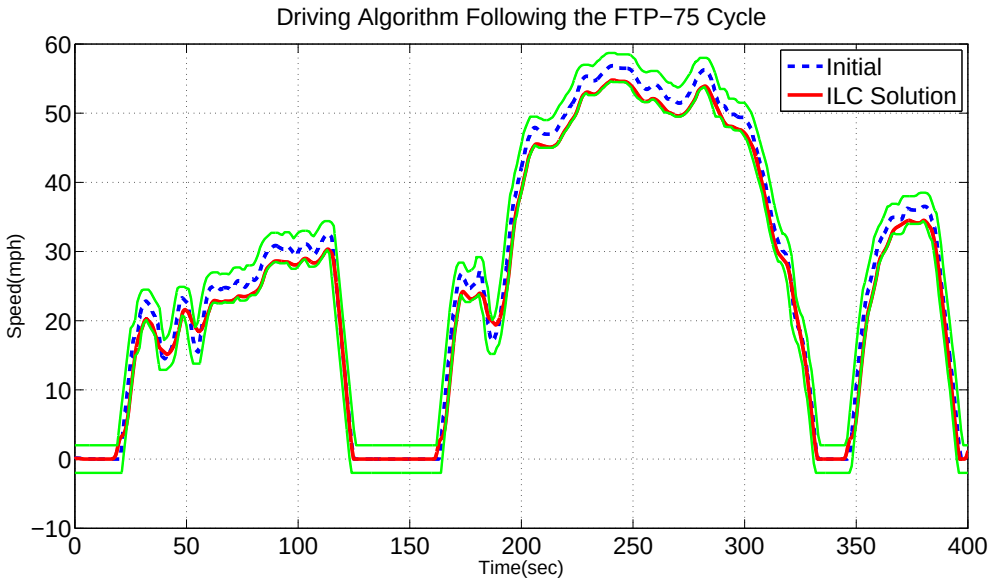

Figure 3.13: Vehicle velocity trace for ILC solution

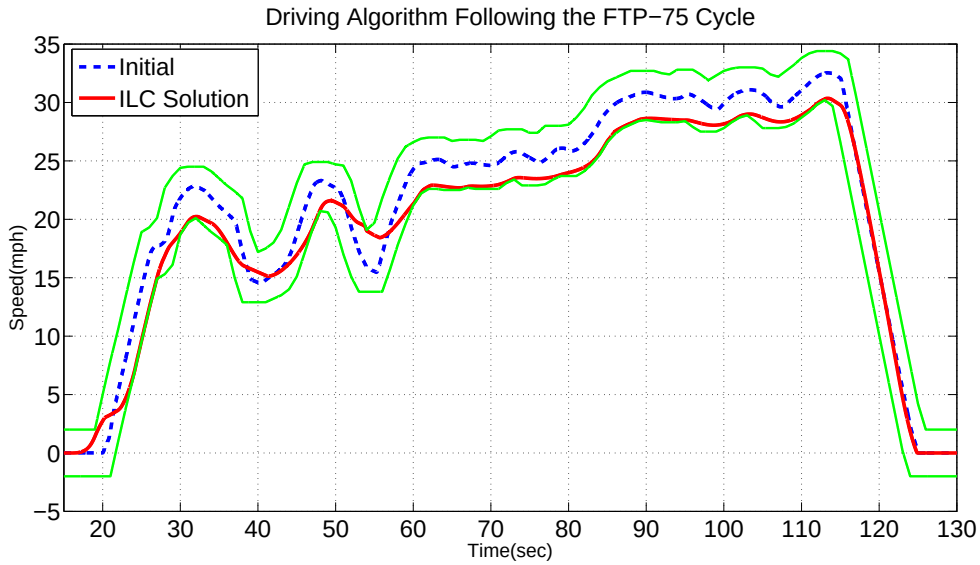

Figure 3.14: Magnified vehicle velocity trace

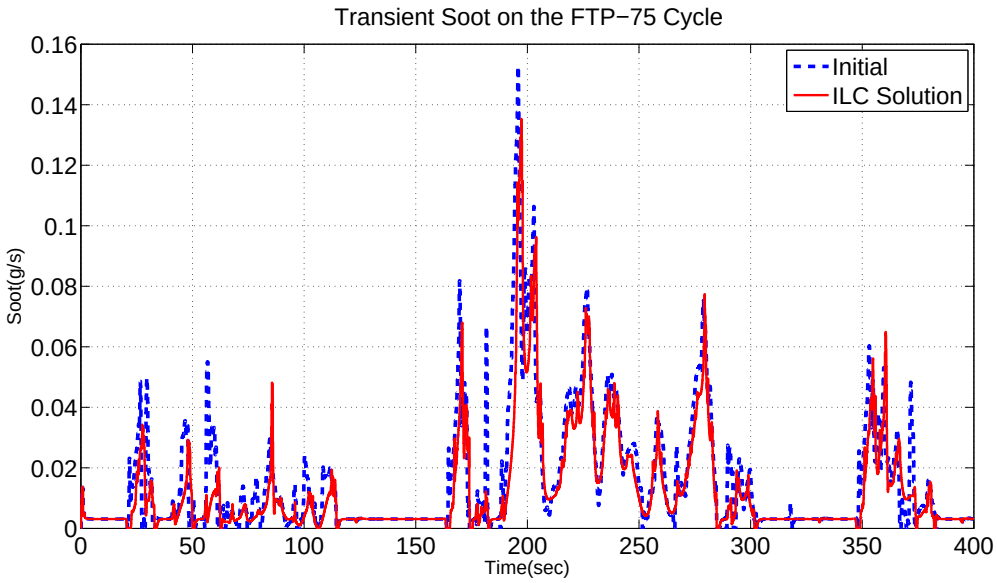

Figure 3.15: Soot trace comparison

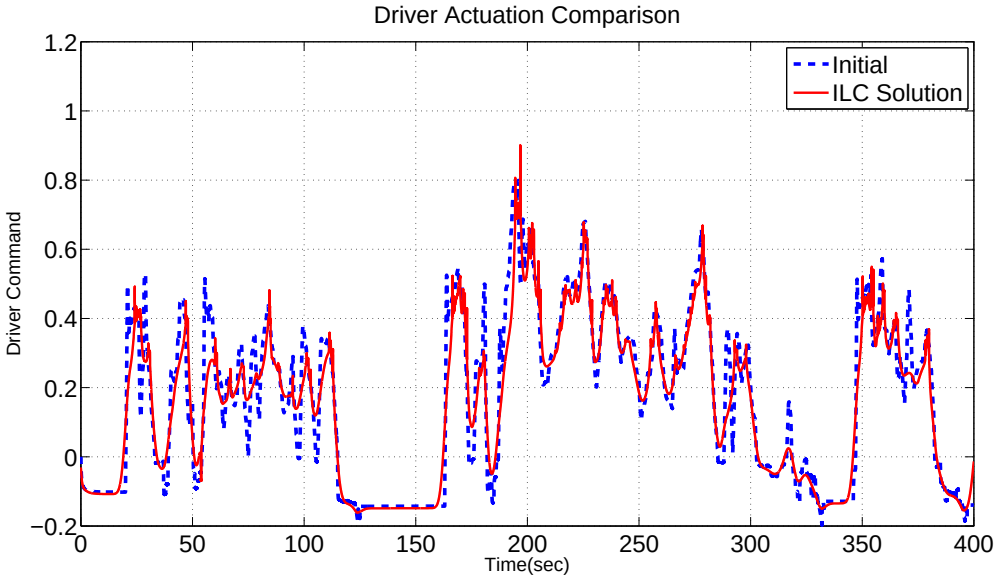

Figure 3.16: Driver actuation comparison

tion problem was defined for the FTP-75 cycle with constraints keeping the vehicle speed within EPA speed limits. The optimal driver trace was first obtained using a linear programming approach. It was shown that an alternate objective function such as the sum of positive vehicle accelerations was able to deliver better performance than an objective function for minimizing soot. The results showed 13.4% reduction in total soot but were still computationally intensive. Then a first-order PD-type ILC scheme was developed to reduce the total soot that resulted in 18.8% improvement, substantially reducing the transient soot spikes, with just 40 simulation runs.

By calculating the driver input trace that reduces soot emissions, this work provides a consistent basis for evaluating the influence of changes in powertrain designs on transient soot emissions. This methodical procedure can be applied to different design candidates for evaluating their soot performances over a drive cycle, and for enabling a fair comparison by eliminating the variability introduced by a fixed driving style. This ILC based algorithm can also be readily applied to a real vehicle operating on a chassis dynamometer as the model is quite robust. Although the driving algorithm

has been developed for reduction in transient soot, the proposed framework is general enough to be applied to other objective functions. Moreover, the use of ILC has been demonstrated in an application where conventional optimization schemes cannot be applied due to the computational load.

CHAPTER IV

Real-Time Transmission Model Development

This chapter presents a real-time powershift transmission model development for engine-in-the-loop experiments for evaluating transient soot. Transient soot emissions produced during EIL experiments are very sensitive to transient loading on the engine and the transmission model plays a key role in dictating transients during gear-shift events. The simulation of a powershift transmission involves representation of slip-stick friction that often results in numerical stiffness affecting the model's RT properties. In this work a framework is presented to model a generic powershift transmission with Margolis friction model for RT simulation using fixed time-step integration solvers. It is shown that a better representation of shift dynamics can be obtained using this method than static blending functions and that these dynamics have a substantial effect on the transient soot from the engine. This model can thus enable transmission calibration and control system development for reducing soot emissions.

4.1 Introduction

This chapter presents the development of a RT powershift transmission model for use in engine-in-the-loop experiments for evaluating transient soot. Powershift transmissions are stepped-ratio transmissions characterized by continued transmission of

power during gear shifts by the use of friction clutches. While these friction elements determine the transmission output torque, they also produce transient load on the engine and can significantly impact engine performance during gear-shift events [117, 118]. Hence the transmission model fidelity is a key enabler for our desired EIL experiments.

The desired transmission model is intended for use in both RT and non-real-time applications for evaluating transient soot emissions by systems-level researchers. Hence, it should fulfill four distinct requirements. First, it must be able to run in real-time without requiring any additional numerical procedures such as multiframing or variable time-step solvers. Secondly, it must accurately represent the transient load incident upon the engine for the purposes of capturing the effect on transient soot, especially during shift events. Thirdly, it should be able to accommodate a variety of commercially available transmission types for studying the impact of various vehicles/powertrains on transient soot. Finally, it must be easy to parameterize and use for systems-level work. Such a model would improve the fidelity of EIL experiments and provide better estimates of transient soot from the vehicles.

Control oriented real-time transmission models available in the literature model the gearsets along with the interconnected shafts as lumped parameter mass-spring-damper systems. Shift dynamics are represented using an empirical blending function [24, 132] or by modeling the physics of slip-stick friction. While the blending functions are easy to simulate without adding any substantial computational load, they can often result in unrealistic shifting behavior leading to the loss of fidelity during shifts. On the other hand, simulating slip-stick friction interfaces for a powershift transmission could be challenging for RT simulation due to numerical stiffness or logical complexity issues. Using static friction models such as Karnopp model results

in high logical complexity that rises exponentially with the number of friction interfaces. Kozaki et al. [129] demonstrated the use this clutch friction by reducing it through surrogation. Others have implemented various numerical schemes to handle this complexity in RT, such as modifying the fixed time-step integration scheme [133], and multiframing [134]. Klages et al. [100] present the use of dynamic reset integrator model with the RT simulation of Ravigneaux geartrain. The numerical stiffness during simulation is avoided by careful selection of PI gains, while hydraulics were not simulated.

The proposed approach in this work uses the dynamic Margolis friction model that does not require any information about the rest of the system. Popular commercial power transmission designs are analyzed and it is shown that the majority of them involve an oncoming friction interface and an offgoing friction interface during a gear-shift event that produces the characteristic shifting dynamics for such transmissions. Hence, a dual-clutch model is proposed that emulates this clutch to clutch shift inherent in powershift transmissions by alternately acting as on-coming and off-going clutches. The different clutch capacities and friction properties of various clutches in the transmission are implemented using gain scheduling. The effective inertia and compliance of the gearset is reflected as a lumped parameter model. Since the primary interest lies in looking at the low frequency aspects of transmission's dynamic system behavior, effects such as friction between gears and backlash are neglected. Though this formulation is general enough to include viscous effects, the work here does not take that into account. One of the advantages of this formulation is that no other information about the system is needed and hence it can be used as a subfunction in any vehicle system model with a powershift transmission. The Volterra series model is then used to capture the effect of gear-shifts from this transmission model on transient soot, and results are compared to the one obtained using a blending function.

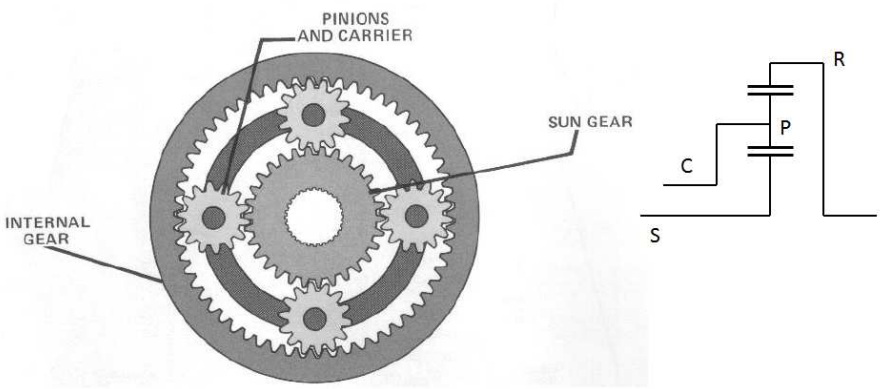

Figure 4.1: Schematic of an epicyclic gear-set

The rest of the chapter is organized such that section 4.2 discusses the dynamics of clutch-to-clutch shift, some popular friction models are presented in section 4.3 and section 4.4 presents the proposed model. Simulation results are presented in section 4.5 and the chapter's summary is outlined in section 4.6.

4.2 Dynamics of a Clutch-to-Clutch Shift

This chapter presents the need for clutches in a transmission and discusses the resulting dynamics from clutch-to-clutch shifts. The schematic of an epicyclic geartrain is shown in Figure 4.1. The common representation of this geartrain is using one-half of the side view, since the system is axisymmetric. The kinematic equations of this gear set are shown in Equations 4.4, where ω_a denotes the angular speed, T_a denotes the torque and N_a denotes the number of gears, where a can be carrier (C), sun (S) or the ring gear(R). It can be seen that in order to uniquely define all the speeds of this gear-set, two out of three speeds should be specified.

$$\omega_C = \left(\frac{N_S}{N_S + N_R}\right)\omega_S + \left(\frac{N_R}{N_S + N_R}\right)\omega_R \tag{4.1}$$

$$T_S = \left(\frac{N_S}{N_S + N_R}\right)T_C \tag{4.2}$$

$$T_R = \left(\frac{N_R}{N_S + N_R}\right)T_C \tag{4.3}$$

$$\tag{4.4}$$

Automatic transmissions use more than one of such gearsets connected to each other, forming a compound planetary geartrain. One of the popular configurations is modified Simpson arrangement shown in Figure 4.2. This is characterized by CR-CR (carrier-ring, carrier-ring) connections. Two of such planetary gearsets would have six speed variables and only two speed equations governing them (Equation 4.4 for each planetary gearset). In order to the number of degrees of freedom, two CR connections are made thus acting as two constraint equations. Therefore the result is two equations in four unknowns. In order to eliminate these two extra variables, friction clutches are used to make gear-specific interconnections with typically one of the clutches specifying the input speed, resulting in a unique speed ratio for every clutch combination. Different gear ratios are obtained by combination of different clutches, with two of them engaged in any given gear. This arrangement is represented using the clutching chart shown in Table 4.1. It should be noted that typically only one clutch is changed from one gear to another in order to have better shift control. As a result of this clutch switching, gear shift events involve oncoming and offgoing clutches.

Typically, the gear shifting process can be divided into two distinct phases, as shown in Figure 4.3 for an upshift. The first phase is called the torque phase. As the hy-

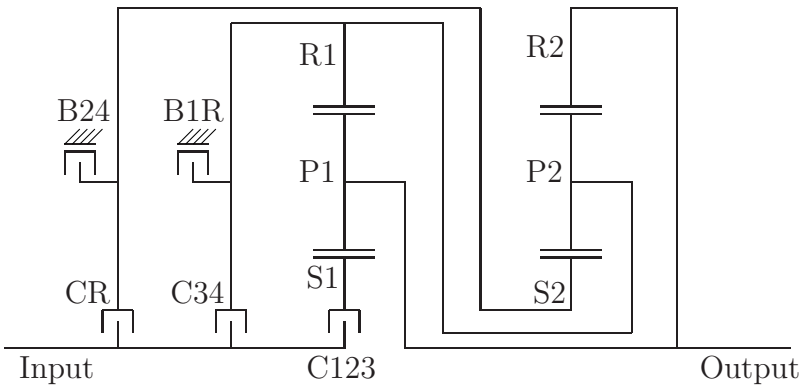

Figure 4.2: Stick diagram of a 4-speed modified Simpson geartrain

Table 4.1: Clutching chart for the 4-speed modified Simpson geartrain

Gear	**C123**	**C3R**	**CR**	**B1R**	**B24**
1	×			×	
2	×				×
3	×	×			
4		×			×
R			×	×	

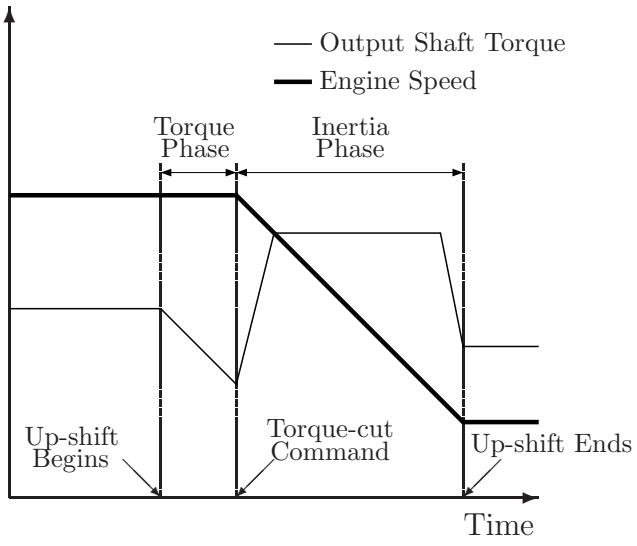

Figure 4.3: Torque and speed variations during up-shift

draulic pressure in the clutch cavity of the offgoing clutch starts decreasing, its torque capacity also decreases, and so does the torque carried by the clutch. In the initial part of this phase, the constraint effect of the control clutches remains unchanged and the corresponding dynamic equations have therefore the same form as the before the shift. The offgoing clutch remains locked at all times, but the torque transmitted through it decreases, first slightly, and towards the end of this phase steeply. Once the pressure starts building up in the oncoming clutch towards the end of the phase, the torque capacity of the oncoming clutch increases, and the increased torque transmitted through the oncoming clutch causes the torque transmitted through the offgoing clutch to decrease steeply. Throughout this phase, the engine speed remains essentially constant and this phase lasts until the offgoing clutch separates.

The next phase starts when the offgoing clutch has disengaged and the oncoming clutch is slipping, as it does not have enough torque capacity to accelerate the inertial load. The speed of the engine decreases as output inertia (vehicle) is much greater than the input inertia. As the pressure builds up in this clutch, the torque capacity

increases and slip speed reduces as both the surfaces try to attain the same speed. After the torque capacity becomes high enough to accelerate the inertial load, the clutch is locked. This phase is called speed or inertia phase and lasts till the torque capacity continues to rise and until the maximum torque capacity is achieved.

The shift quality during this clutch-to-clutch shift is dependent on how well the pressures of the two clutches are controlled. During the torque phase of the lower gear, as the torque capacity of the offgoing clutch decreases and the clutch capacity of the oncoming clutch increases, the output torque decreases significantly. This is caused by the transfer of torque from a higher gear ratio to a lower gear ratio (upshift), and is commonly known as torque hole. Ideally, the offgoing clutch is disengaged at the exact moment when it's transmitted torque transitions from a positive to a negative value. This perfect shift occurs naturally when overrunning or one way clutches are used in the mechanism. However when hydraulically actuated friction clutches are used, a perfect shift is difficult to accomplish, but is closely approximated in many modern automatic transmissions. If the offgoing clutch is disengaged too late, the clutches fight each other and bindup (or tie-up) occurs. Bindup also enlarges the size of the torque hole more than necessary, giving the driver a feeling of reduced power. If the offgoing clutch is disengaged too early, the capacity of the oncoming clutch is not sufficient to balance the engine torque, the engine accelerates noticeably and flare occurs. Bindup and flare are both undesirable, although flare is more noticeable to the driver whereas bindup is more damaging to the transmission. The clutch pressures are thus controlled to ensure satisfactory shift quality.

The shift control is obtained through both, the coordinated control of clutch pressures with fuel injection and throttle commands as well as direct control of clutch pressures. To reduce the torque peak during inertia phase, fuel injection is usually delayed at

the beginning of this phase [114, 171]. Direct control of clutch pressures is extremely difficult due to the lack of reliable pressure sensors inside the transmission. In the absence of these pressure signals, the clutch control is achieved through hydraulic feedback (washout signal) [172], slip-speed control [173], or estimated input/output torques [115]. Watechagit [135] presents online estimation for pressures using non-linear observers. Extensive review of shift control is beyond the scope of this work and interested readers are referred to [135, 174].

4.3 Modeling Slip-Stick Friction for Clutches

This section presents the popular slip-stick friction models from the literature. Since friction opposes the motion and its magnitude is independent of velocity and contact area, it can be described using Coulomb's law as

$$T_f = T_c \, sgn(\omega_s) \tag{4.5}$$

where T_f is the friction torque, and T_c is the Coulomb torque which is proportional to the normal load. This model is represented in Figure 4.4(a). Since it does not specify the value of the friction torque, it can take any value in the interval $[-T_c, T_c]$. Therefore this represents a model with ideal relay or switched causality. In wet clutches hydrodynamic forces also contribute to the friction force caused by the viscosity of lubricants. Such a friction force, T_v, is a function of slip velocity. Another component of static friction model is stiction (static friction), that describes the friction force at rest to be higher than the Coulomb friction level. Static friction counteracts external forces below a certain level and thus keeps an object from moving. The Stribeck effect describes the friction force at low velocities does not decrease discontinuously but that the velocity dependence is continuous. The model including these effects (shown in Figure 4.4(a)), and takes the form

$$T_f = \begin{cases} T(\omega_s) & \text{if } \omega_s \neq 0 \\ T_e & \text{if } \omega_s = 0 \text{ and } |T_e| < T_s \\ T_s \, sgn(T_e) & \text{otherwise} \end{cases} \tag{4.6}$$

where $T(\omega_s)$ is the viscous torque, T_e is the external torque and T_s is the Stribeck friction torque. Although this model is simple to implement, this causal inversion causes problems in model formulation by changing the explicit nature of model equations. To circumvent this problem, various alternate models have been proposed. One approach to overcome the discontinuity is to approximate it by a linear region near zero velocity as shown in Figure 4.4(b), resulting in the so called classical model [96, 122]. Although simple in nature, it allows the body to accelerate even though the forces on the body are less than peak stiction force. It also causes numerical stiffness in the model if the linear approximation around zero velocity has a steep slope. One popular way to remove the discontinuity is by using a hyperbolic tangent function instead, though the problems associated with acceleration and numerical stiffness still persist. Karnopp proposed a fixed causality model [123] to overcome the lack of verisimilitude at low velocities. This was achieved by introducing a narrow stiction region in which the friction torque does not depend on relative speed but rather on equivalent applied torque to the friction element (Figure 4.4(c)). Thus, the order of the system is effectively reduced during stiction while the friction force is calculated by an empirical function of slip speed outside this region. Though this method is quite accurate and easy to simulate [96, 122], it requires the derivation of separate set of equations for each possible combination. Hence the complexity of the friction model increases exponentially with the number of friction elements. For example, if a modified Simpson geartrain has 5 friction surfaces, then there are 2^5 combinations of discrete states. Therefore, when using this model for modeling automatic gearbox there is need for abstraction or numerical algorithms to deal with this logical com-

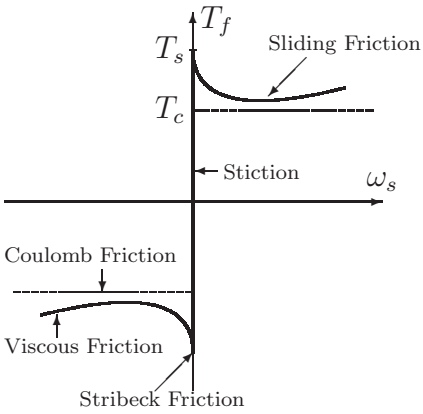

(a) Static Friction Model

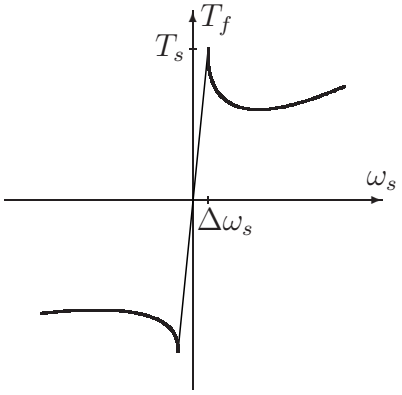

(b) Classical Friction Model

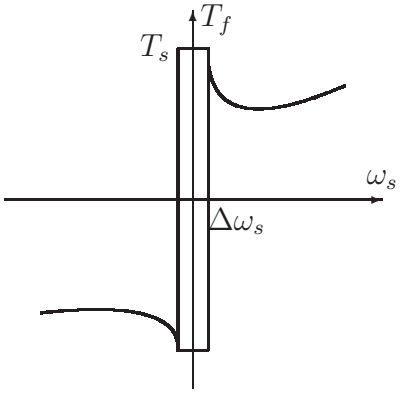

(c) Karnopp Friction Model

Figure 4.4: Comparison of static friction models

plexity in real-time

Dynamic friction models can be used to avoid the need to calculate the constraint force manually. Haessig and Friedland [122] proposed a popular model known as the reset integrator model. It models the friction element as a spring when slipping and as spring-damper when stuck. The switching between the slip and stick states is dictated by the displacement of the spring. Let the spring deflection θ_s be defined such that $\dot{\theta}_s = \omega_s$, the spring stiffness be $k_s(\omega_s)$ and b_s represent the damping coefficient, then the friction torque, T_f is calculated as

$$T_f = (1 + a(\theta_s))k_s(\omega_s)\theta_s + b_s\tilde{\omega}_s \tag{4.7}$$

where the model switching and stiction force when sticking are represented by $\tilde{\omega}_s$ and $a(\theta_s)$ such that

$$\tilde{\omega}_s = \begin{cases} 0 & \text{if } (\omega_s > 0 \,\text{and}\, \theta_s > \theta_{s_0}) \,\text{or}\, (\omega_s < 0 \,\text{and}\, \theta_s < -\theta_{s_0}) \\ \omega_s & \text{otherwise} \end{cases} \tag{4.8}$$

$$a(\theta_s) = \begin{cases} a & \text{if } |\theta_s| < \theta_{s_0} \\ 0 & \text{otherwise} \end{cases} \tag{4.9}$$

Thus, the damping is active only when sticking ($|\theta_s| < \theta_{s_0}$). As the deflection reaches its maximum value θ_{s_0}, only the spring force is active, and its value also drops due to the absence of stiction. With this model the logical complexity does not increase with the number of friction surfaces, like it did with Karnopp model. It was shown that reset-integrator model approaches Karnopp model as spring stiffness and damping rate go to infinity. Margolis [121] proposed a variation of this model where slip velocity was used as the switching criteria between the two discrete states instead of

the spring displacement, and during slipping the friction element acted as damper. While both of these models are physically intuitive, simulating these models in RT could be challenging due to numerical stiffness if high damping coefficient and spring stiffness are used. The exact cause of this reason is elucidated next.

4.3.1 Control Systems Perspective on Numerical Integration

Once the model is formed in the continuous-time domain, it is converted into discrete-time using numerical integration methods for simulation. The integration solver used for real-time simulation also requires the use of explicit, low order causal algorithms such as Euler, Adams-Bashforth and Runge-Kutta methods running fixed time-steps, as the communication between the model and the hardware needs to be synchronized at a predetermined rate [175]. Standard solvers for stiff and constrained systems are implicit or variable time-step based, and cannot be used in real-time without modifications because of their iterative and/or adaptive strategies [176]. Hence, simulating a numerically stiff system in RT using a fixed time step integration solver is a challenging task. Although there exist some alternate methods that can be used for solving stiff ODEs under certain conditions, such as linearly implicit integration methods [176, 177], Jacobian approximation using sparsing techniques [178], multi-framing or time scale decomposition [179, 180], or implementation of stability limit as constraint [181], a large number of models are only limited to the use of fixed time-step solvers in RT due to practical limitations.

While the slow decay rates dictate dominant dynamics of a system, the fast ones control the stability of the numerical method [182]. One of the ways to analyze the stability properties of a (linear) discretized system is to look at the poles of its pulse transfer function. This transfer function is obtained using s-to-z mapping functions to approximate the continuous-time transfer function. When bilinear transformation

(or Tustin's rule), which is an implicit method, is used, any stable continuous-time filter will be converted into a stable discrete-time filter using this mapping function. However, the stability regions of mapping functions from explicit integration methods do not contain the entire left half-plane [183, 184]. To elucidate this point, consider the linear system governed by the equation $\dot{x} = Ax$, where $x \in \mathbb{R}^m$ and $A_{m\times m}$ is a constant matrix with eigenvalues λ_j where $j = 1, 2, 3...m$. Then Euler's forward difference method (explicit fixed time step integration method) can be expressed as

$$x_{n+1} = x_n + h\dot{x} \tag{4.10}$$

where h is the fixed integration time-step. Let $P(hA) = I+hA$, then $x_{n+1} = P(hA)x_n$, and the condition for absolute stability dictates

$$|x_{n+1}| < |x_n| \Rightarrow |I + hA| < 1 \tag{4.11}$$

Since A has eigenvalues λ_j, then $P(hA)$ has eigenvalues $(1+h\lambda_j)$ where $j = 1, 2, 3...m$. Hence absolute stability demands $|1 + h\lambda_j| < 1$, or in the scalar case, $|1 + h\lambda| < 1$. Since h is always a positive real number and λ is a complex number, the region described by $|1 + h\lambda| < 1$ on a complex $h\lambda$ plane is referred to as the region of absolute stability, and the function $P(hA) = I+hA$ is called the stability function. Karim [185] derived stability regions of higher order Runge-Kutta methods, and these regions of stability are shown in Figure 4.5. When the system has more than one eigenvalue, all the eigenvalues must follow the stability condition. It can be seen that as the order of integration algorithm increases, the region of stability also increases, making it possible to integrate a given system (in a stable way) using larger integration time steps. Also note that a purely oscillatory system cannot be integrated using a first or second order integration algorithms, whereas Runge-Kutta 3^{rd} and 4^{th} order methods can integrate an unstable system in a stable fashion. Thus, when simulating a nu-

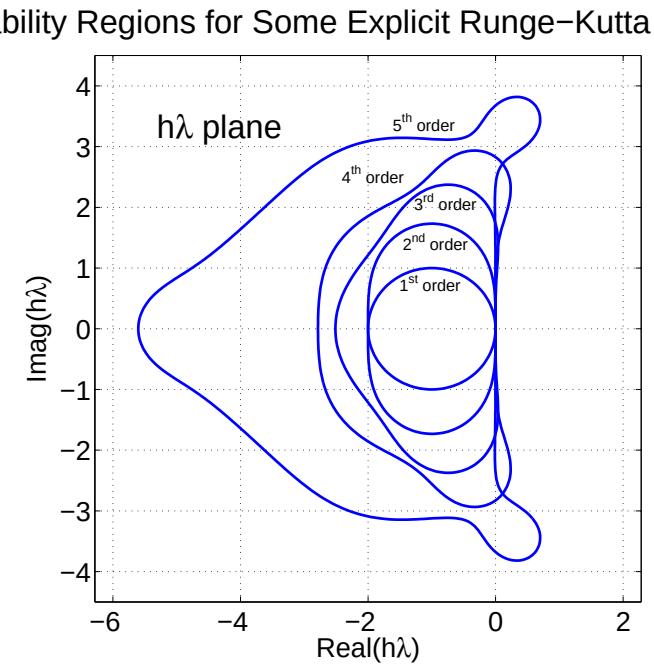

Figure 4.5: Region of stability for different orders of Runge-Kutta methods

merically stiff system using one of these explicit fixed time-step solvers, the highest eigenvalue enforces the use of a much smaller integration time-step than the one that is required to simulate the dominant dynamics, resulting in excessive computations and often the loss of real-time simulation properties.

Thus, model structure, model complexity and the numerical solution have to be adapted to the needs of real-time simulation. While this stability constraint can be implemented directly for linear systems, being cognizant of the underlying causes of numerical stability is still important for nonlinear discontinuous systems [186]. Hence, based on model properties such as the number of states, damping coefficients, etc. and some simulation trials, a decision on the order of integration method and the step-size of the numerical solver can often be obtained.

4.4 Development of Real-Time Transmission Model

This section presents the development of a real-time powershift transmission model for use in EIL experiments. The model is required to possess sufficient fidelity to accurately capture shift transients while being computationally efficient, as well as should be able to accommodate different powershift drivetrain configurations without extensive modifications or parameter identification. Some of the popular automatic transmission designs are 4-speed modified Simpson (e.g. GM Hydramatic 440), 4-speed Ravigneaux (e.g. BMW A4S270R, A5S310Z, A5S325Z), 5-speed extended Simpson (e.g. ZF 5HP24) and 6-speed Lepelletier (e.g. Toyota U660E, Ford 6R60, GM 6L80, ZF 6HP19) shown in Figures 4.2, 4.6, 4.7,and 4.8 respectively. The schedule of clutches for these different designs can be read from their clutching charts and it seen that that almost all the gearshifts (for forward vehicle motion) involve an oncoming clutch and an offgoing clutch. Although there exist a very few exceptions to this rule [109], such a design is favorable from a controls standpoint to achieve a much smoother shift. Figure 4.9 shows the stick diagram of a dual-clutch transmission (DCT) where odd and even gears are mounted on parallel shafts. This specific DCT differs from the automatic transmissions in that it uses the clutch for launching instead of a torque converter and spur gears are used instead of epicyclic gears. However, synchronizers engage before a gear-shift, and gear ratio transfer is achieved by engaging one clutch and disengaging the other. Hence if synchronizers are treated as ideal power switches, the gearshift dynamics are similar to that of an automatic transmission.

Therefore, to develop a generalized framework for modeling a powershift transmission, two separate clutches are required to be modeled: an oncoming and an offgoing clutch. Since the interest lies in predicting the low frequency dynamics, the transmission gears and shaft inertias are lumped as a second order mass-spring-damper system. From a

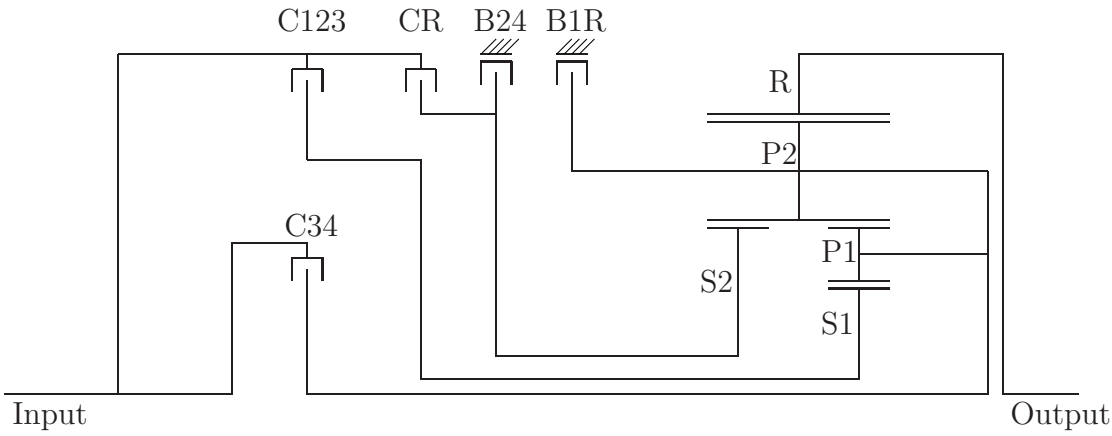

Figure 4.6: Stick diagram of a 4-speed Ravigneaux geartrain

Table 4.2: Clutching chart for the 4-speed Ravigneaux geartrain

Gear	**C34**	**C123**	**CR**	**B1R**	**B24**
1		×		×	
2		×			×
3	×	×			
4	×				×
R			×	×	

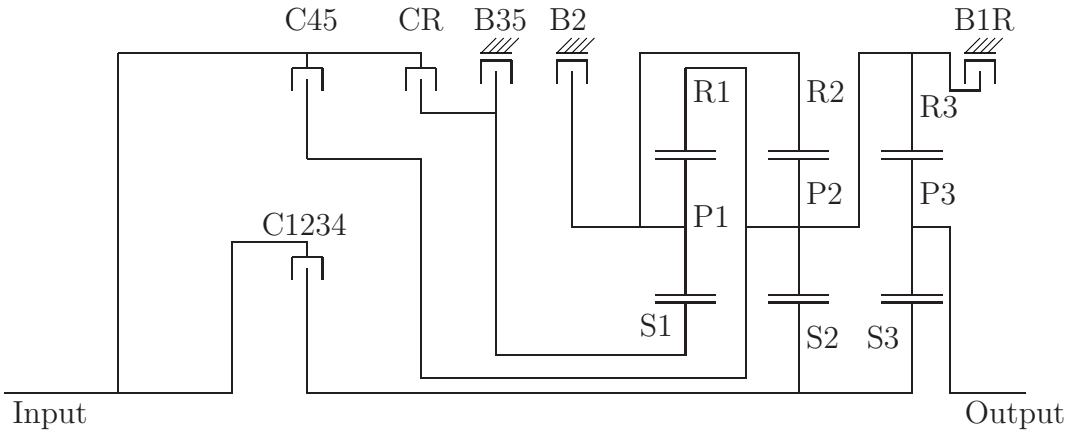

Figure 4.7: Stick diagram of a 5-speed extended Simpson geartrain

Table 4.3: Clutching chart for the 5-speed extended Simpson geartrain

Gear	**C1234**	**C45**	**CR**	**B35**	**B2**	**B1R**
1	×					×
2	×				×	
3	×			×		
4	×	×				
5		×		×		
R			×			×

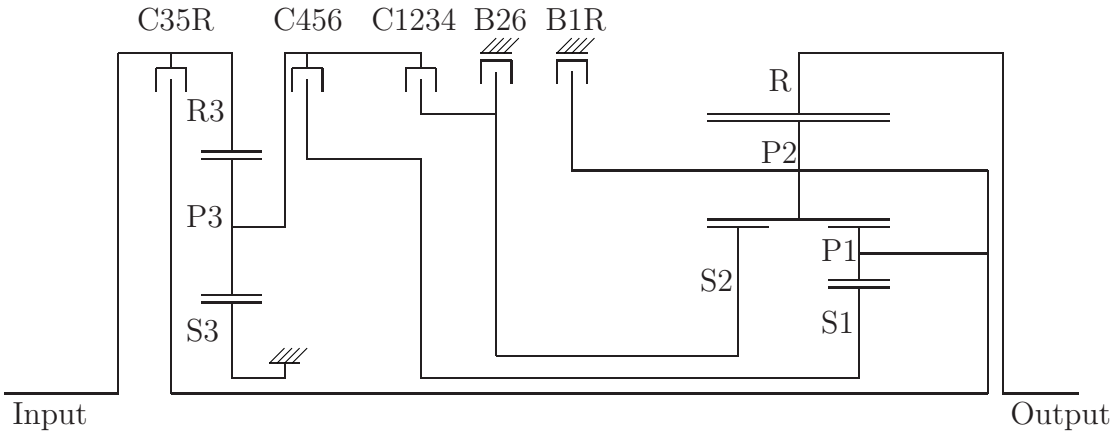

Figure 4.8: Stick diagram of a 6-speed Lepelletier geartrain

Table 4.4: Clutching chart for the 6-speed Lepelletier geartrain

Gear	**C35R**	**C456**	**C1234**	**B1R**	**B26**
1			×	×	
2			×		×
3	×		×		
4		×	×		
5	×	×			
6		×			×
R	×			×	

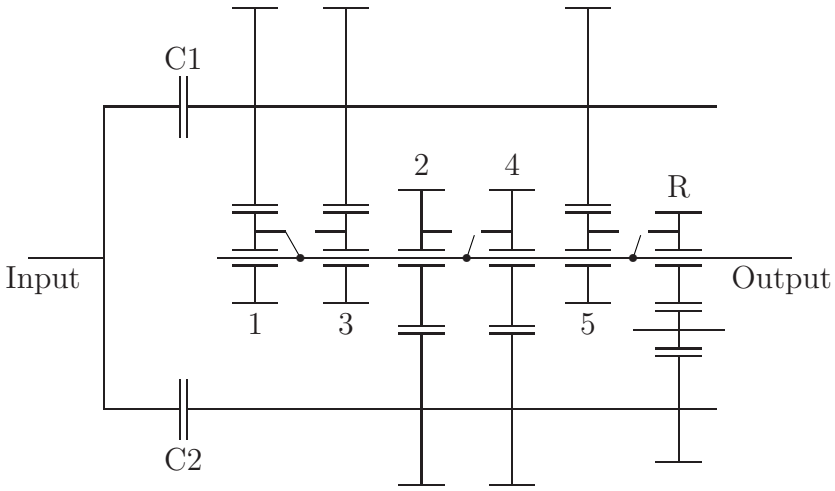

Figure 4.9: Stick diagram of a typical dual-clutch transmission

physical standpoint, not all clutches are alike, and possess different clutch capacities and coefficients of friction, but they operate on the same physical principles. These differences are accounted using gain scheduling, without adding any additional states into the system. The decision for a slip-stick friction model from the literature is dependent on the generalizability of the proposed approach. Since the framework is intended to be used in different drivetrain configurations, a constraint equation is not implemented for the stick-slip friction (Karnopp model). Instead, a dynamic Margolis model is used that models the clutch friction as a damper when slipping and a spring with damping when locked. The solver selection and time-step decision framework presented in the previous section is used to iteratively select spring stiffness, damping coefficient and solver step-size so that acceptable results can be obtained. Let ω_{in} be the clutch input speed (turbine speed for an automatic transmission) and $\omega_{t_{in}}$ the transmission input speed, then the clutch's slip speed, ω_s is defined as $\omega_s = \omega_{in} - \omega_{T_{in}}$. The clutch remains locked as long as the slip speed remains less than some critical slip velocity, ω_s^c and the clutch capacity, T_{cap}, is sufficient to carry the external torque. When the clutch starts slipping, the torque transmitted is a function of this speed.

In this work the slip torque, T_{slip} is calculated as

$$T_{slip} = T_{cap} \cdot \tanh\left(\frac{\omega_s}{k}\right) \tag{4.12}$$

where k is a scaling parameter. The clutch capacity is a function of the clutch inner and outer radii, R_i and R_o, the number of friction interfaces, N, the coefficient of friction, μ, the surface area A and the applied pressure. The governing relationship for clutch capacity can then be calculated using the constant pressure theory as

$$T_{cap} = \frac{4}{3} N \mu(\omega_s) \frac{R_o^3 - R_i^3}{R_o^2 - R_i^2} A \eta P_{max} \tag{4.13}$$

where $\eta \in [0, 1]$ is the clutch modulation signal and P_{max} is the maximum pressure. The clutch modulation signal is calculated offline using a full hydraulics model simulation and specified as a feedforward signal. This proposed model, in combination with the torque converter and the differential model presented in Appendix C, is shown in Figure 4.10 when the clutch is locked. As the gear-shift command is issued, the clutch capacity starts decreasing for the offgoing clutch though it still remains locked, and the oncoming clutch starts slipping (torque phase). This arrangement is depicted in Figure 4.11, and it can be seen that torque is being transmitted through two separate mechanical paths. Later during the torque phase, the offgoing clutch starts slipping (Figure 4.12) and is disengaged ($T_{cap} = 0$) at the beginning of the inertia phase. Therefore, a clutch-to-clutch shift transmission is modeled using just two friction component models, and without requiring any other configuration information about the system.

4.4.1 Obtaining Clutch Pressure Profiles

Most of the clutches used in today's transmissions are hydraulic clutches. The clamping force of the hydraulic clutch is obtained by hydraulic pressure with no me-

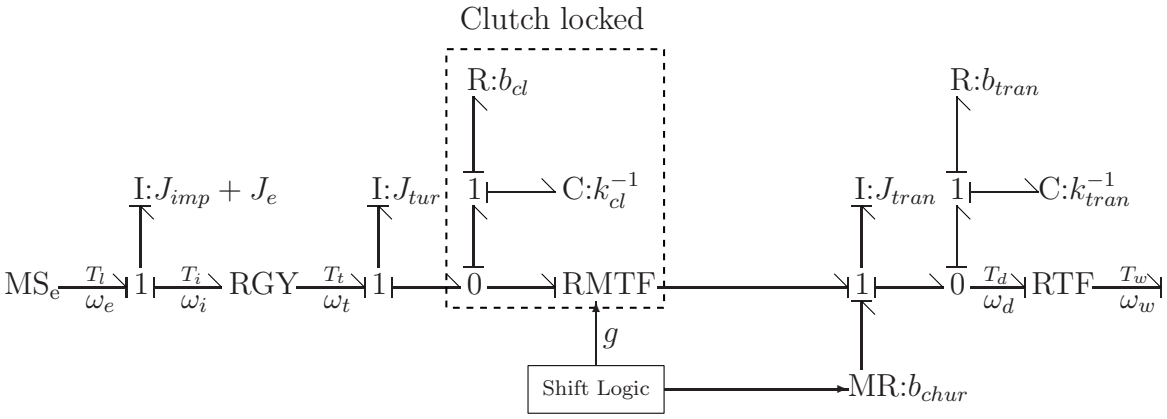

Figure 4.10: Clutch locked before/after the gear-shift

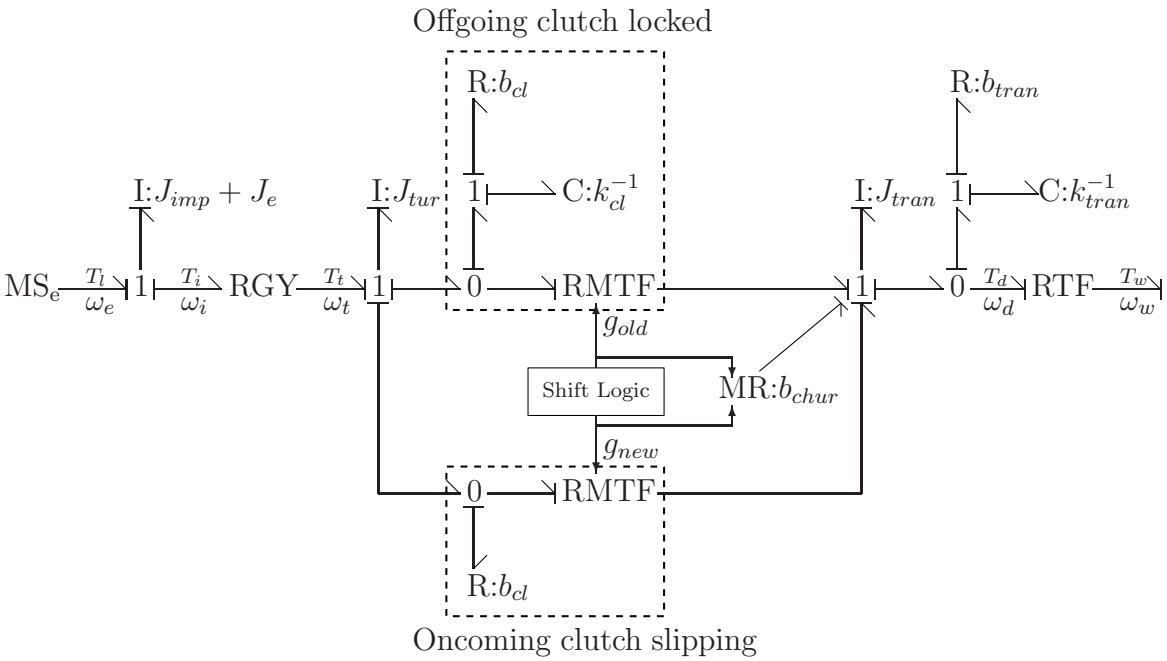

Figure 4.11: Offgoing clutch locked during gear-shift

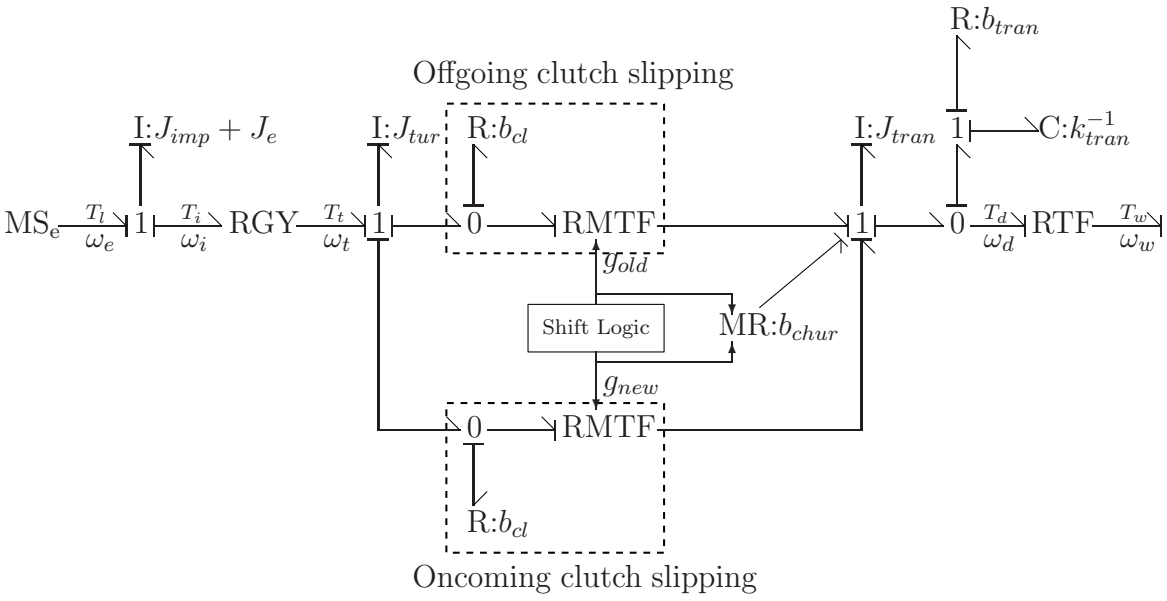

Figure 4.12: Offgoing clutch slipping during gear-shift

chanical linkages connecting the force piston to the operating lever, and hence the clutch engagement rate must be controlled by controlling the pressure buildup in the force cavity of the clutch [187]. The clutch pressures are controlled using pulse-width modulated (PWM) solenoid valves [135]. It converts a current signal into a hydraulic pressure output and the dynamic characteristics are modeled using a second order transfer function, assuming constant line pressure. The output pressure of the solenoid is fed to the pressure control spool valve as the signal pressure. The position of the spool (x_v) is the result of the force balance of signal pressure force, output pressure force and offset spring force. Let p_{out} be the output pressure, p_s the signal pressure, p_{sup} the supply pressure, p_{fb} is the feedback pressure, A_s the area of the signal pressure side, A_{fb} the area of the feedback pressure side, $A_{in}(x_v)$ the intake flow area as a function of the spool position, $A_{out}(x_v)$ the output flow area as a function of the spool position, M_v the mass of the spool, D_v and k_v the damping

coefficient and spring stiffness, β the bulk modulus of the fluid (assumed constant), C_d the discharge coefficient, x_{ov} the spring pre-load, ρ the mass density of oil, V the chamber volume and Q the flow rate, then the dynamic equations can be written as

$$M_v\ddot{x}_v = A_s p_s - A_{fb}p_{fb} - D_v\dot{x}_v - k_v(x_v + x_{ov}) \text{ where } |x_v| < x_{lim} \tag{4.14}$$

$$\dot{p}_{out} = \frac{\beta}{V_{load}}(Q_{in} - Q_{out} - Q_{fb} - Q_{load}) \tag{4.15}$$

$$Q_{in} = sgn(p_{sup} - p_{out})C_d A_{in}(x_v)\sqrt{\frac{2}{\rho}|p_{sup} - p_{out}|} \tag{4.16}$$

$$Q_{out} = sgn(p_{out})C_d A_{out}(x_v)\sqrt{\frac{2}{\rho}|p_{out}|} \tag{4.17}$$

$$Q_{fb} = sgn(p_{out} - p_{fb})C_d \pi r_{fbo}^2(x_v)\sqrt{\frac{2}{\rho}|p_{out} - p_{fb}|} \tag{4.18}$$

$$\dot{p}_{fb} = \frac{\beta}{V_{fb}}(Q_{fb} + A_{vb}\dot{x}_v) \tag{4.19}$$

The hydraulic fluid that is output of the pressure control spool valve is fed to the piston chamber through an orifice with pressure p_s such that the piston is pushed forward. The free travel h needs to be cleared before the clutch force can be established. In the absence of sufficient pressure the return spring pushes the piston back. Let x_p be the displacement of the piston, A_p the area of the piston, p_p the hydraulic pressure in the piston chamber, M_p the mass of the piston, D_s and k_s the damping coefficient and spring constant of the clutch return spring, x_o the spring pre-load, A_{or} the area of the orifice, and V_o the chamber volume when $x = 0$, then the governing equations can be written as

$$M_p\ddot{x}_p = A_p p_p - D_s\dot{x} - k_s(x + x_o) \text{ where } 0 < x < h_p \tag{4.20}$$

$$\dot{p}_p = \frac{\beta}{V_o + xA_p}\left(sgn(p_s - p_p)C_d A_{or}\sqrt{\frac{2}{\rho}|p_s - p_p|} - \dot{x}A_p\right) \tag{4.21}$$

These transmission hydraulic components are modeled for both the clutches and the pressures are controlled to obtain smooth shifts. In the absence of closed-loop control, the release timing of the off-going clutch is based on the estimation of the oncoming clutch fill. The fill time of the oncoming clutch varies due to many factors, and therefore the release timing of the offgoing clutch can be early or late, causing flare or tie-up, respectively. Thus, the use of feedback control is desirable for controlling clutch pressures during a shift. However, clutch pressure sensors are usually not present in production vehicles. In the absence of this information, pressure control is a challenging task, especially during the torque phase when the engine speed remains essentially constant. Proposed methods in the literature include model based estimation of pressures [135], estimation of output shaft accelerations [173], estimation of output shaft torque [188], controlling slip-speeds [115, 189], and mechanical control using washout [172]. Due to the simplicity of implementation, the washout signal based pressure control is implemented in this work. The on-coming clutch pressure is used as a reducing signal ('washout' signal) to control the valve pressurizing the off-going clutch. The complete vehicle and transmission model, along with the hydraulics model is simulated for vehicle tip-in and braking operations, while the numerical integration is carried out with a variable time-step solver. The clutch modulation signal, η, is defined as the ratio of clutch pressure to the maximum clutch pressure, and is recorded for different gear-shifts. A sample clutch modulation profile for the off-going clutch is shown in Figure 4.13.

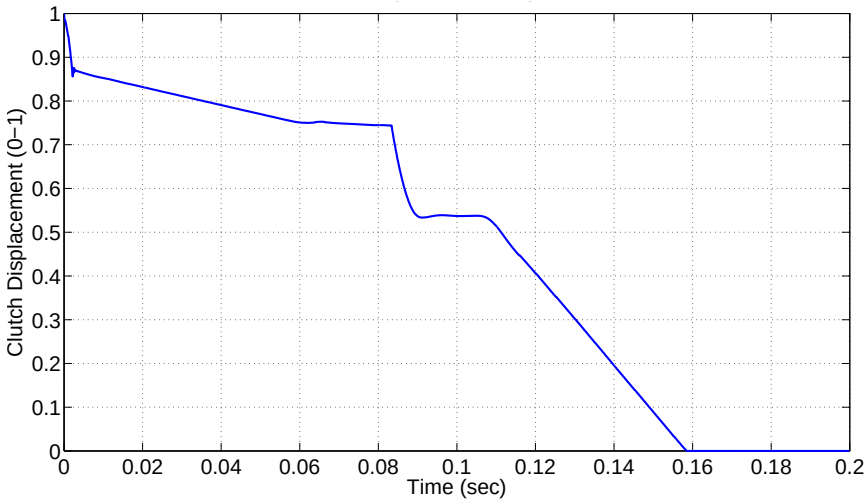

Figure 4.13: Off-going clutch modulation profile

4.4.2 Simulation Results

The proposed transmission model is integrated with the other vehicle system models presented in Appendix C and the Volterra series based transient soot model presented in Chapter 2. The numerical stiffness problems associated with simulating transmission hydraulics is avoided by getting pressure signals from offline simulation and using them as feedforward signals, while those associated with simulating slip-stick friction are dealt by a careful selection of solver step-size with spring stiffness and damping coefficient of the clutches. Transition from slip to stick state was implemented to take place when the slip speed dropped below 5 rad/sec. The model was able to run in RT with an integration time-step of 0.5ms. Simulation results for a tip-in operation (throttle command going from $0-100\%$ in 5sec) are presented here. Results are compared with the blending function based model presented in Appendix C. Figure 4.14 shows the upshifts taking place during this operation; different shift dynamics in the two models caused a change in transmission output speed leading to slightly different shift points. The change in engine speed due to different transmission gear-shift models is shown in Figure 4.15, and the resulting change in transient soot is shown in Figure 4.16. Since the blending function is a static map, some ar-

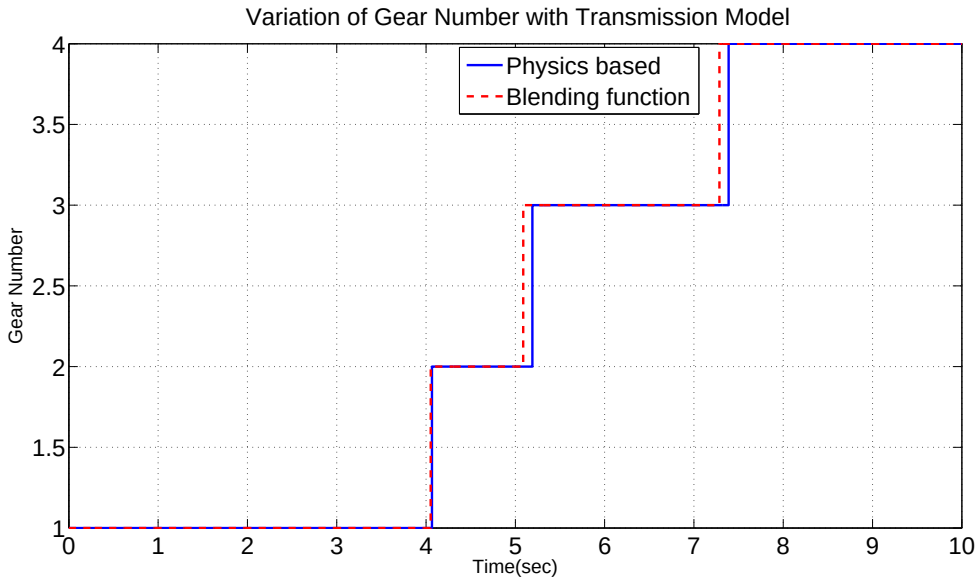

Figure 4.14: Comparison of gear numbers

tificial oscillations are seen in the engine speed. The differences in the engine speed profiles result in different transient soot profiles, with some values being over 30% different. The output torque profiles are shown in Figure 4.17. The same blending function is unable to produce smooth shifts for all conditions, whereas the proposed physics based transmission model results in much smoother shifts.

4.5 Summary

Transient soot emissions produced during EIL experiments are a strong function of transient loading on the engine and the transmission model plays a key role in dictating transients during gear-shift events. The simulation of a powershift transmission involves modeling slip-stick friction that results in numerical stiffness affecting the model's RT properties. In this work a framework was presented to model a generic powershift transmission with Margolis friction model for RT simulation using fixed time-step integration solvers. Popular commercial power transmission designs were analyzed and it was shown that a large majority of them involve an oncoming friction

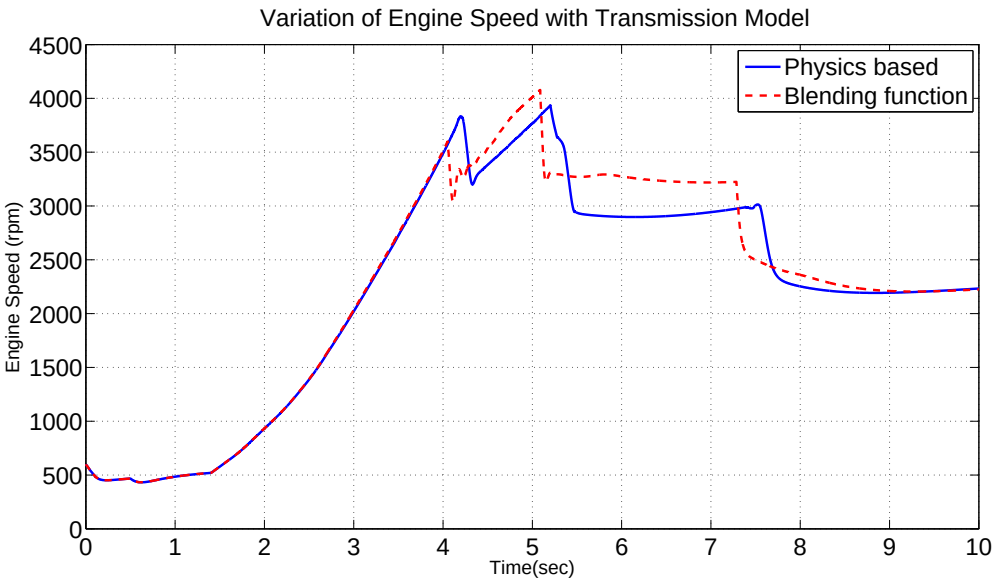

Figure 4.15: Comparison of engine speeds

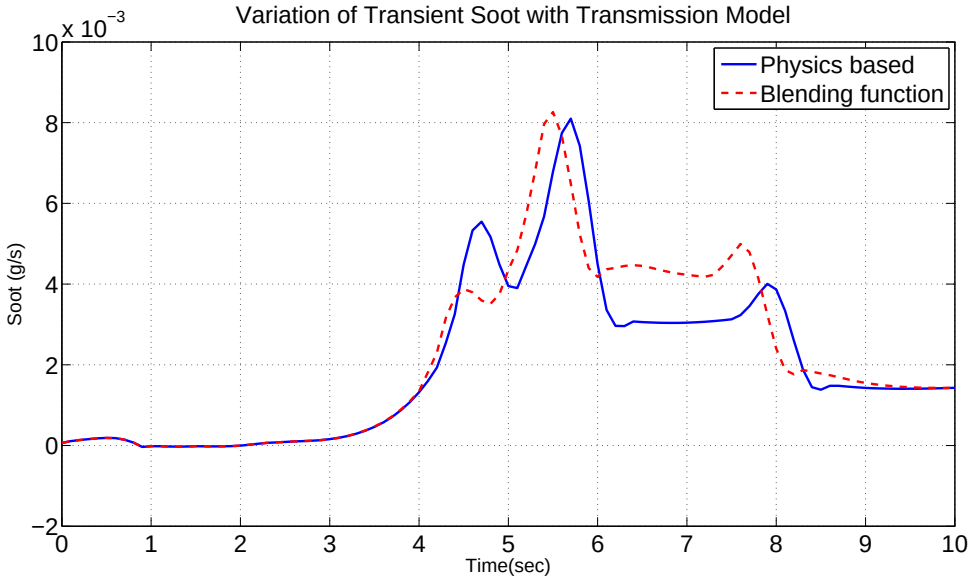

Figure 4.16: Comparison of transient soot

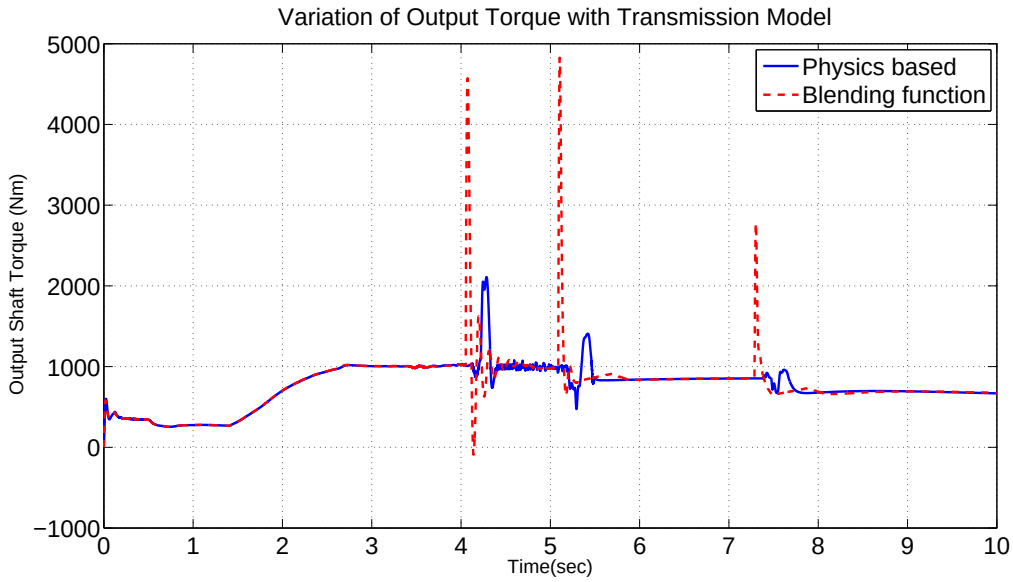

Figure 4.17: Comparison of output shaft torques

interface and an offgoing friction interface during a gear-shift event that produces the characteristic shifting dynamics for such transmissions. Hence, a dual-clutch model was proposed that emulated this clutch-to-clutch shift inherent in powershift transmissions by alternately acting as on-coming and off-going clutches. The different clutch capacities and friction properties were implemented using gain scheduling. The effective inertia and compliance of the transmission gears and shafts were reflected using a lumped parameter model. It was shown that this formulation does not require any other information about the system and hence can be used as a subfunction in any vehicle system model with a powershift transmission. The Volterra series model was then used to capture the effect of gear-shifts from this transmission model on transient soot, and results were compared to the soot obtained using blending function based transmission models. It was seen that a better representation of shift dynamics can be obtained using the proposed method than static blending functions and that these dynamics can have a substantial effect on transient soot from the engine.

CHAPTER V

Conclusions

This dissertation presented a modeling and simulation framework for diesel engine vehicles to enable soot emissions as a constraint in powertrain design and control. To this end, this work made the following contributions:

1. Enable recording of transient soot data using EIL experiments
    - Real time vehicle level models were developed and integrated with test cell hardware.
    - Temporally resolved transient soot data were obtained and correlated with other control and input signals such as fuel flow rate and throttle pedal position.
2. Provide computationally efficient low order transient soot models for systems-level work
    - A third order Volterra series with just two inputs, fuel flow rate and throttle pedal position, was used to model the transient soot emission and significant improvements over steady-state maps were presented.
    - The number of parameters to be estimated for the Volterra series were reduced by Principal Component Analysis (PCA) using energy considerations.

3. Provide a consistent basis for comparison of powertrain design changes by synthesizing driver inputs

    - Iterative learning based algorithm was used to drive the vehicle in a manner that reduces transient soot emissions.
    - ILC based algorithm produced substantial improvement in soot with much less computational load than linear programming based solution.

4. Provide a generalized modeling framework for real-time simulation of powershift transmissions with fixed time-step integration solver

    - Various slip-stick friction models were studied and their numerical properties were analyzed for RT simulation.
    - The Margolis model was selected and implemented in the modeling framework. The effects of gear-shifts from this transmission model on transient soot were shown, and the results were compared to blending function based model.

5.1 Future Work

The framework presented in this dissertation provides a methodical procedure for considering the influence of design changes on transient soot. In this context, the importance of transmission design and control is highlighted here. Heavy-duty trucks and freight-liners use automated-manual transmissions (AT) with over 18 gear-ratios to maintain engine operation around high efficiency range as much as possible. Frequent changes in vehicle loading, such as those caused by changes in road-grade on the freeway, can result in frequent gear-shift events. The Volterra series based soot model, and physics based transmission model developed in this work, enable transmission sizing and control system design to implement soot sensitive gear-shift

control. The use of ILC based algorithm to synthesize driver input traces provides a fair comparison to evaluate these design decisions. Such systematic evaluations can greatly reduce the calibration time as well as provide a consistent basis for making sizing decisions on gear-ratios and designing gear-shift logic for such transmission systems.

APPENDICES

APPENDIX A

A Brief Overview of Diesel Soot Formation Modes

Diesel particulate matter formation exhibits dual mode formation: nucleation mode and accumulation mode. Particle formation is initiated with the pyrolysis of the fuel in the absence of oxygen into soot nucleation sites. Once the particles are formed, they undergo surface growth which adds considerable mass. When two particles collide, they may form a new particle either through coagulation or agglomeration. Coagulation (surface growth) results when two small, relatively young spherical particles collide with a large number of active sites. When the collision particles are old, there are much fewer active sites resulting in an aggregate structure (agglomeration). Surface growth and particle aggregation both contribute to the particle growth process in the accumulation mode [4, 11]. These various soot formation modes are shown in Figure A.1.

The sequences of particle size-number distributions obtained during an interval of the FTP-75 cycle with DMS is shown in Figure A.2. The particle size at the beginning of the transient is shown in Figure A.2(a). The near-idle operation is characterized by relatively large numbers of very small particles, while the profiles show greater particle diameter size at the on set of a transient load. This shift in particle size

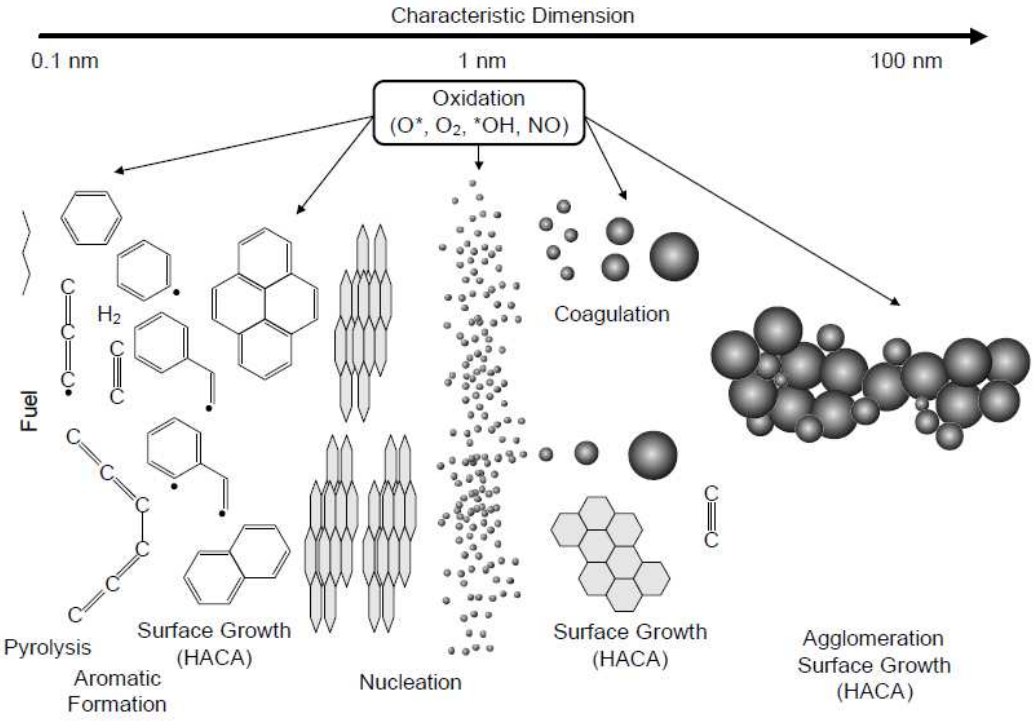

Figure A.1: Modes of soot formation [11]

distribution represents a puff of smoke emanating from the exhaust manifold of a diesel vehicle. The features of the particulate size distributions change as the engine stabilizes during high load conditions resulting in the typical dual-mode shape (Figure A.2(b)). In summary, particle formation due to nucleation is predominant at low-load steady-state operations resulting in smaller spectral diameter of the particles. At transient loads, accumulation mode also contributes to the particle formation of bigger diameters and high load steady-state operation displays the dual model behavior [23].

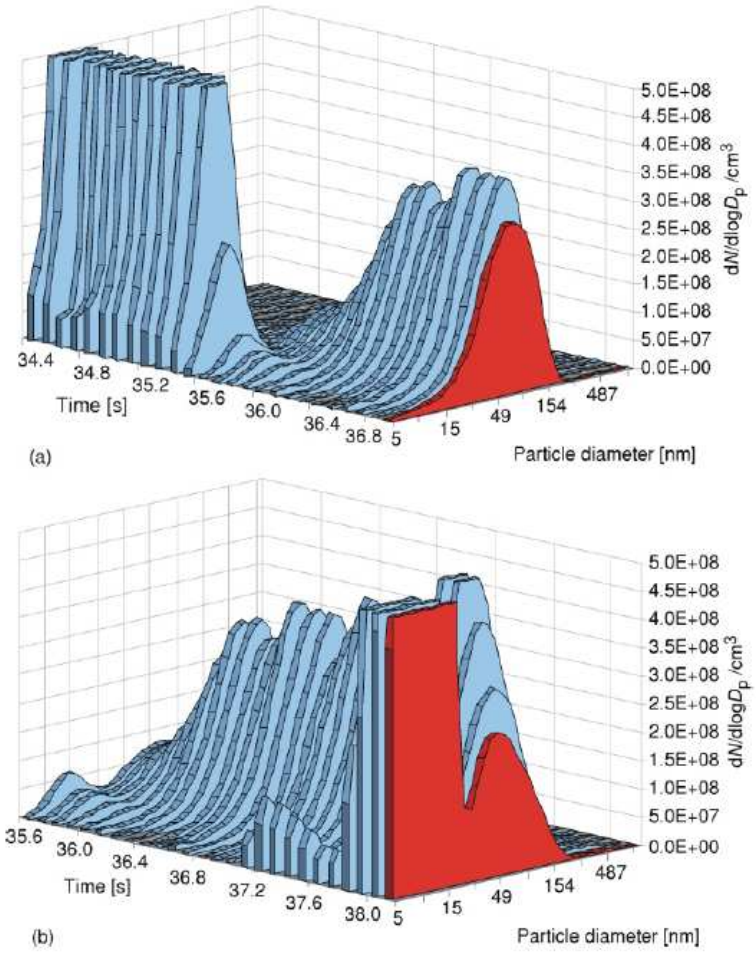

Figure A.2: Particle size distributions during transient operation on FTP-75 [23]

APPENDIX B

Hardware Specifications for Engine-in-the-loop Experiments

Engine-in-the-loop (EIL) experiments integrates a real engine with virtual vehicle level models running on a real-time (RT) platform to enable engine testing under transient conditions [190]. Driver, transmission, and vehicle models are simulated on the real-time (RT) platform and used to control an AC dynamometer coupled to a 6.0L V-8 direct-injection diesel engine. These models accurately capture the desired dynamics while being numerically efficient to run in real-time [24]. The vehicle level models are forward-looking, hence the driver model issues throttle (α) and brake commands (β) to follow the vehicle velocity on the FTP-75 city cycle. Model causality is selected such that the torque converter model commands speed to the engine, as speed is easier to control than the engine torque. The measured engine torque is fed to the torque-converter model to enable closed-loop drive-cycle simulation. The transient soot data are recorded using a differential mobility spectrometer (DMS).

The engine used in this investigation is an International 6.0L V-8 direct-injection diesel engine. The engine is equipped with exhaust gas recirculation (EGR) to introduce cooled exhaust gases into the intake manifold. EGR flow rate is controlled

Table B.1: Engine Specifications

Engine Type	4-stroke diesel, V-8 configuration, Direct injection
Displacement	6.0L
Aspiration	Variable geometry turbocharger
Rated Power	242kW @3300rpm
Rated Torque	760Nm @2000rpm

through the modulation of the EGR valve and the setting of the variable geometry turbocharger (VGT). The VGT is also used to enhance engine performance as it reduces turbocharger lag and allows control of intake manifold pressure. The engine control is achieved using INCA software and hardware provided by ETAS Inc., and allows for monitoring and control of all electronically controlled quantities including EGR flow rate, VGT setting, and injection characteristics [4]. Complete engine specifications are presented in Table B.1.

Dynamometer

The engine speed is controlled using an AC dynamometer. The dynamometer used in this investigation is a 330kW AVL ELIN series 100 asynchronous dynamometer. This dynamometer is especially suited for transient testing as it has a 5ms torque response time and a -100% to $+100\%$ torque reversal time of 10 ms. The complete specifications of the dynamometer are presented in Table B.2.

Control of the dynamometer, engine, measurement, and auxiliary devices is facilitated through PUMA open software by AVL. Part of this software is the EMCON 400 controller used for engine and dynamometer control using tunable PID controllers. Control over the engine is exercised through pedal position; a throttle controller inputs $0 - 5$V signal in the engine wiring harness that corresponds to $0 - 100\%$ of pedal position.

Table B.2: Dynamometer Specifications

Speed Range	$\pm$8000 rpm
Torque Range	-1273 Nm to $+1400$ Nm
Power(absorbing)	330kW
Power(motoring)	330kW
Rotational Inertia	2.91kgm^2
Torque Response	5 ms
Torque Reversal	10 ms(-100% to $+100\%$)

Engine and Dynamometer Instrumentation

Engine speed is measure using a HEIDENHAIN ROD 426 type optical rotary encoder. It has a scanning frequency of 300kHz and a system accuracy of $1/20^{th}$ of the grating period. An HBM Z6 bending beam (load cell) is used for the torque measurement at the dynamometer. Intake manifold is instrumented with a pressure transducer to measure intake manifold pressure. The sensor is placed close to the cylinder to give an accurate reading of the conditions in the intake manifold. The sensor used is a piezoelectric pressure transducer (Kistler 4618A0) with a functional range of $0-2$ bar and a nonlinearity and hysteresis of $< \pm 0.3\%$ of full scale operation. It is connected to a charge amplifier that produces $0-10$ Volt DC signal proportional to the measured pressure.

A coriolis flow meter is used to measure the fuel mass flow rate. The sensor capacity is 377.8 g/s with an error resolution of $\pm 0.5\%$ of flow rate. It outputs a $4-20$ mA that is linear to the mass flow rate.

Differential Mobility Spectrometer

Temporally resolved particulate concentrations are recorded by a differential mobility spectrometer (DMS) 500 by Cambustion. This instrument measures the number of particles and their spectral weighting in the 5nm to 1000nm size range with a time response of 200ms [19], and the data are provided at 10Hz. The instrument provided aerosol size spectral data by using corona discharge to place a prescribed charge on each particle. The charged particles are then introduced into a strong electrical field inside a classifier column. This field deflects the particles away from the electrode through a sheath flow toward the electrometer detectors. Particles with lower aerodynamic drag-to-charge ratio are deflected more quickly and are attracted towards the electrode rings closer to the beginning of the classifier column, and vice versa. As the particles land on the grounded rings, and give up their charge, the outputs from the electrometers are processed in real time to provide spectral data and other desired parameters [4, 23].

These aerosol size spectral data are then converted into particulate mass. Agglomerates formed during diesel combustion are non-spherical and therefore their mass does not correlate with the cube of the particle diameter. Similarly, the constituents of the particles change as the diameter varies and consequently there is a non-linear relationship between particle density and diameter. To convert particle spectral density to mass, a relationship has been suggested by the manufacturer [23]. The spectral diameter (D_p) in nanometers is divided into bins, density of the particles within each bin is assumed to be constant and then the mass of the particles in each bin is determined by

$$\text{Particle Mass} = 6.95 \times 10^{-3} \cdot D_p^{2.34} \cdot \text{Number of particles} \tag{B.1}$$

APPENDIX C

Real-Time Models for Engine-in-the-loop Experiments

The accuracy of HIL simulations is dependent on the quality of real-time models. Estimating and improving the model quality is thus a key enabler in a successful HIL simulation [191]. While many limitations exist on the hardware, such as the fidelity of sensors and actuators, network/control bandwidth, and signal conditioning and processing, model fidelity is often the limiting factor during HIL experiments [190]. This appendix provides the details of drivetrain and vehicle dynamics models used for EIL experiments. These models are executed on a dSPACE real time board, and require a fixed integration time step. As these models subject the engine to transient loads, it is important that they accurately represent vehicle transient loads along with the capability to run in RT. The driver model is responsible for the closed-loop following of the vehicle on the prescribed drive cycle and is discussed in the next section.

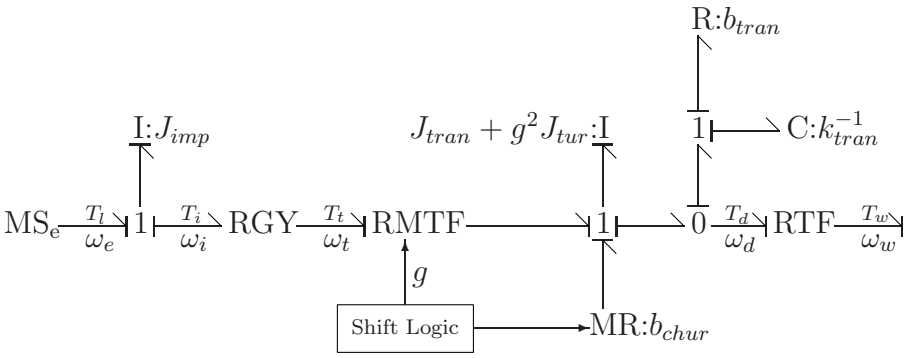

Figure C.1: Bond Graph Model of the Drivetrain

Drivetrain Model

Models of the drivetrain include torque converter, automatic transmission, and open differential. The bond graph model of the complete drivetrain is shown in Figure C.1. The measure engine load torque (T_l) is an input to the drivetrain model and is represented as a modulated effort source in the bond graph. This torque is then used to accelerate the torque converter impeller inertia, J_{imp}, and calculate the impeller (or engine speed), which is commanded to the engine by the dynamometer.

The inputs to the torque converter model are the impeller (ω_i) and turbine speed (ω_t), and the outputs are impeller (T_i) and turbine torques (T_t) calculated from steady-state characteristic curves. The characteristic curves represent the relationship between the torque ratio (TR), speed ratio (SR), and input capacity factor (K) defined as

$$SR = \frac{\omega_t}{\omega_i} \tag{C.1}$$

$$TR = \frac{T_t}{T_i} \tag{C.2}$$

$$K = \frac{\omega_i}{\sqrt{T_i}} \tag{C.3}$$

The K-factor and torque ratio curves [2, 24] used in this work are shown in Figure C.2.

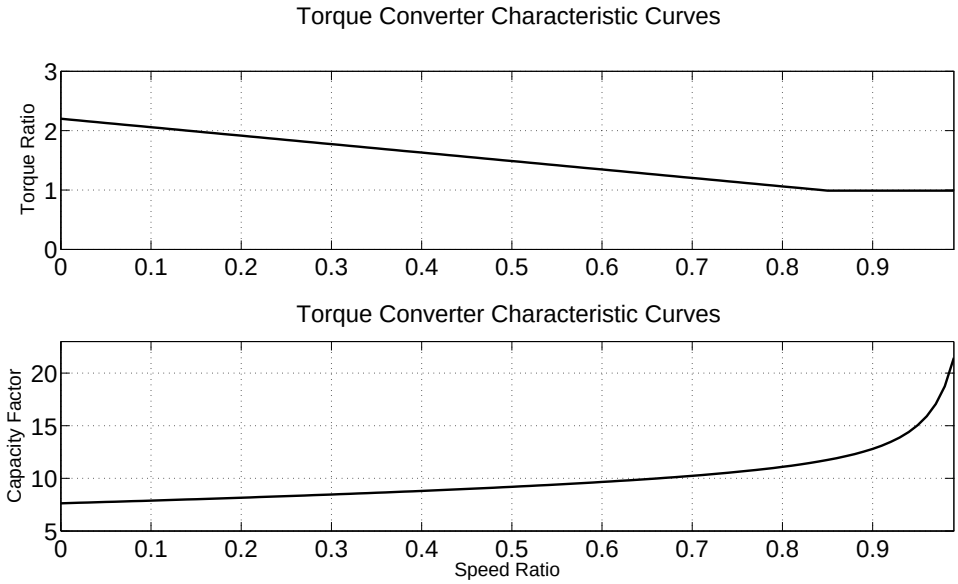

Figure C.2: Torque Converter Characteristic Curves

In the bond graph model, this relationship is represented in the form of a resistive gyrator (RGY), as the flow motion in a physics-based torque converter model exhibits gyrator action [192]. Kozaki et al. [129] show that torque converter dynamics typically become pronounced at frequencies of approximately $30 - 50$ Hz. In this work, the EIL setup is required to have a bandwidth of $15 - 25$ Hz, therefore, modeling the torque converter as a static set of characteristic curves is acceptable for this work.

The output torque of the torque converter is an input to the transmission model. Part of the torque imparted by the torque converter on the transmission is lost as a result of oil churning. This churning loss depends on the speeds of the different transmission gears, and therefore depends on the transmissions instantaneous gear ratio. Thus churning losses are modeled as a modulated resistor incorporating the relationship

$$T_{chur} = b^g_{chur,1}\,\omega_t + b^g_{chur,2}\,\omega_t^2 \tag{C.4}$$

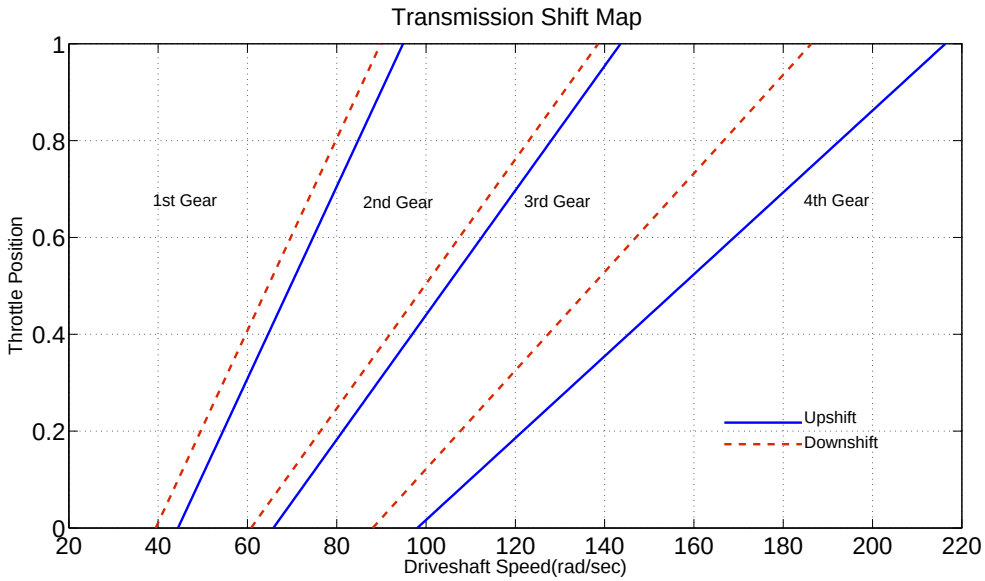

Figure C.3: Shift Map

The remaining torque excites the dynamics of the transmission and drive shaft, which can be captured using a lumped parameter mass-spring-damper model. The kinematic relationship of the gear-box are incorporated in the form of a resistive modulated transformer element, RMTF, with the transformer coefficient modulated by the instantaneous effective gear ratio. Based on the driver throttle position (α) and the transmission output shaft speed (ω_d), a shift map is incorporated to decide the gear of operation. The shift map is developed to keep the engine in the desired operating range while meeting the grade and top speed requirements for the vehicle. The upshift and downshift speeds are differed to prevent gear hunting. The shift map used in this work is shown in Figure C.3.

The transients introduced during the process of gear-shift are captured using the effective gear ratio. This gear ratio is constant when a particular gear is fully engaged, but it varies with time during gear shifting. This variation is represented by blending function [24, 132] as shown in Figure C.4 for a well controlled up-shift event. A smooth shift controls the pressure profiles in the clutches to reduces flare or tie-up

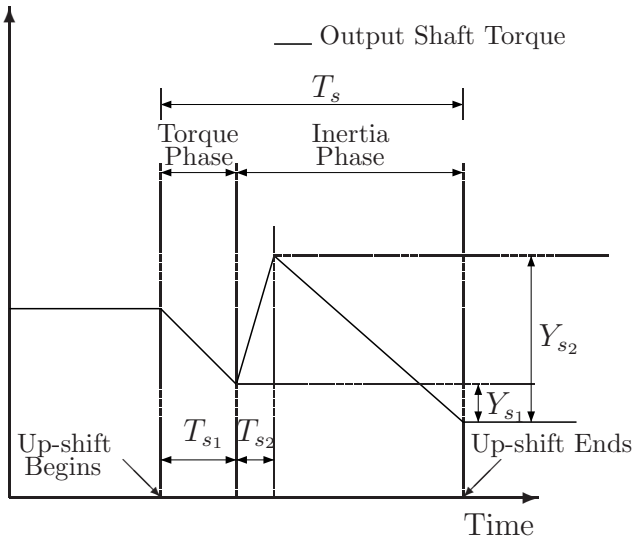

Figure C.4: Torque variation during up-shift

Table C.1: Blending Function Parameters

Parameter	Value
T_s	0.8 sec
T_{s_1}	0.2 sec
T_{s_2}	0.4 sec
Y_{s_1}	0
Y_{s_2}	0.3

in the transmission and hence controls the variation of torque ratio. This blending function is implemented in the RMTF element along with the shift map to capture the variation in torque and speed during the gear-shift. The numerical parameters of the blending function are listed in Table C.1.

The open differential is modeled as a resistive transformer to incorporate the kinematic relationships for the final gear reduction with some losses. The complete list of parameters for the drivetrain model is presented in Table C.2.

Table C.2: Drivetrain Model Parameters

Parameter	Description	Value
J_{imp}	Impeller inertia	0.18 kgm^2
J_{tran}	Transmission inertia	0.2 kgm^2
J_{tur}	Turbine inertia	0.12 kgm^2
k_{tran}	Transmission shaft stiffness	6250 N/m
b_{tran}	Transmission shaft damping coefficient	0.000079709 Ns/m
$b^1_{chur,1}$	First coefficient of churning loss for gear 1	0.0192 Ns/m
$b^2_{chur,1}$	First coefficient of churning loss for gear 2	0.015 Ns/m
$b^3_{chur,1}$	First coefficient of churning loss for gear 3	0.031 Ns/m
$b^4_{chur,1}$	First coefficient of churning loss for gear 4	0.0367 Ns/m
$b^1_{chur,2}$	Second coefficient of churning loss for gear 1	0.00001361 Ns^2/m^2
$b^2_{chur,2}$	Second coefficient of churning loss for gear 2	0.000005719 Ns^2/m^2
$b^3_{chur,2}$	Second coefficient of churning loss for gear 3	-0.00003189 Ns^2/m^2
$b^4_{chur,2}$	Second coefficient of churning loss for gear 4	-0.00004177 Ns^2/m^2
g_1	1^{st} gear ratio	3.42
g_2	2^{nd} gear ratio	2.26
g_3	3^{rd} gear ratio	1.50
g_4	4^{th} gear ratio	1.00
g_{fd}	Final drive gear ratio	3.56
η_{tran}	Transmission gear efficiency	0.97
η_{fd}	Differential gear efficiency	0.94

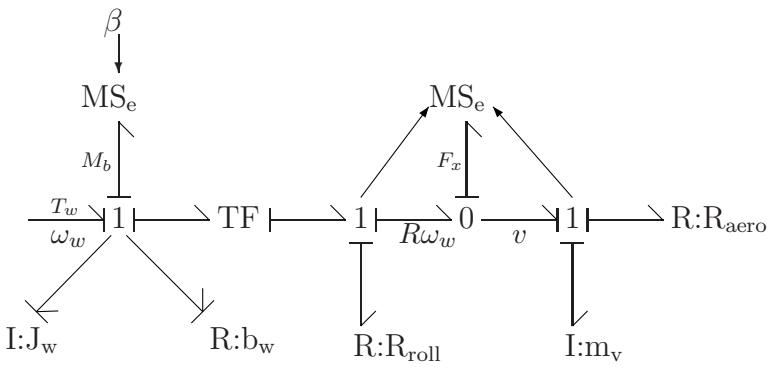

Figure C.5: Bond Graph Model of Vehicle Dynamics

Vehicle Dynamics Model

The dynamics captured in the vehicle model is the longitudinal motion of a point-mass vehicle. The bond graph model of vehicle dynamics is shown in Figure C.5. The brake pedal position command (β) is converted into brake torque using Karnopp's model of stick-slip friction [123, 160]. Rolling resistance is also modeled as an empirical function of wheel speed. The braking moment, bearing loss and rolling resistance losses are subtracted from the wheel hub torque and net torque is used to accelerate the wheel [193]. Let ω_w be the wheel's rotational velocity, T_w, the output torque of the drivetrain, J_w, the wheel's rotational inertia, M_b, the braking moment, F_x, the friction force from the tire in the longitudinal direction, R, the effective rolling radius of the tire, M_r, the moment due to rolling resistance, and b_w, the coefficient of bearing damping, then the wheel dynamics are modeled as

$$J_w \frac{d\omega_w}{dt} = T_w - M_b - F_x R - M_r - b_w \omega_w \tag{C.5}$$

The resulting wheel hub velocity is multiplied by the effective wheel radius in a transformer (TF) to obtain the wheel's longitudinal velocity, $R\omega_w$. This velocity along with the vehicle's longitudinal velocity, v, is used to calculate the longitudi-

nal tractive/braking effort. The longitudinal tractive/braking effort is modeled as a modulated effort source and depends on the slip ratio, $i \in [-1, 1]$, defined as

$$i = 1 - \frac{|v|}{|R\omega_w|}, \quad i > 0, R\omega_w \neq 0 \tag{C.6}$$

$$i = 1 - \frac{|R\omega_w|}{|v|}, \quad i < 0, v \neq 0 \tag{C.7}$$

$$\tag{C.8}$$

The negative values of slip are used to represent skid. Numerical measures are taken to calculate i for low velocities. Once slip is calculated, tractive/braking effort is calculated as

$$F_x = \frac{i\mu m_v g}{i_c} \quad \forall i < i_c \tag{C.9}$$

$$F_x = sgn(i)\mu m_v g \quad \forall i \geq i_c \tag{C.10}$$

where i_c represents a critical slip. Note that $v = R\omega_w$ represents the condition for pure rolling ($i = 0$), and in that case no braking or tracking effort can be produced. Road load such as aerodynamic drag is subtracted from the longitudinal friction force to get the net tractive effort. It is then divided by vehicle mass and numerically integrated to obtain the vehicle velocity.

$$m_v \frac{dv}{dt} = F_x - \frac{1}{2}\rho c_d A \cdot sgn(v) \cdot v^2 - mg\sin(\theta_i) \tag{C.11}$$

The numerical parameters for the vehicle dynamics model are presented in Tab. C.3. A dynamic RT wheel slip model is also developed as an improvement of this model, and is presented in Appendix D.

Table C.3: Vehicle Dynamics Model Parameters

Parameter	Description	Value
m_v	Vehicle inertia	5100 kg
J_w	Wheel inertia	32 kgm^2
R	Wheel radius	0.4412 m
b_w	Wheel bearing damping coefficient	4 Ns/m
μ	Coefficient of friction	0.7
i_c	Critical slip	0.3
A	Frontal area	3.58 m^3
c_d	Coefficient of aerodynamic drag	0.7 m^{-1}
ρ	Air density	1.00 kg/m^3

Driver Model

The vehicle-level models are implemented on the RT platform and the model is integrated using 4^{th} order Runge-Kutta solver with a fixed time-step of 5ms. To enable closed loop simulation for following a prescribed drive cycle, the driver is modeled as a reference-tracking PI controller. The driver model produces the input trace, $u \in [-1, 1]$, where positive commands reflect accelerator pedal position (α) and negative commands reflect the brake pedal position (β). An anti-windup loop is implemented to prevent the windup of driver input due to saturation. The block diagram of the driver model is shown in Figure C.6.

To compensate for the communication lag in the system, a lead filter, $F(s) = \frac{(4.8s + 12)}{(s + 12)}$, was implemented with the PI controller. The lead filter was designed using loop shaping by operating the engine at steady-state, and then superimposing sinusoidal engine speed and pedal position profiles onto the steady-state [23]. Previews of $1, 2$ and 3 seconds was also enabled as a feedforward controller with preview gains for better following of the drive cycle. This driver model structure, along with

the chosen causality of vehicle component models resulting in speed control of the dynamometer, and low inertia of the dynamometer motor resulted in the desired closed loop system bandwidth of $15 - 25$Hz. Overruns were limited to $< 1\%$ of integration time steps, and were mostly concentrated during model initialization.

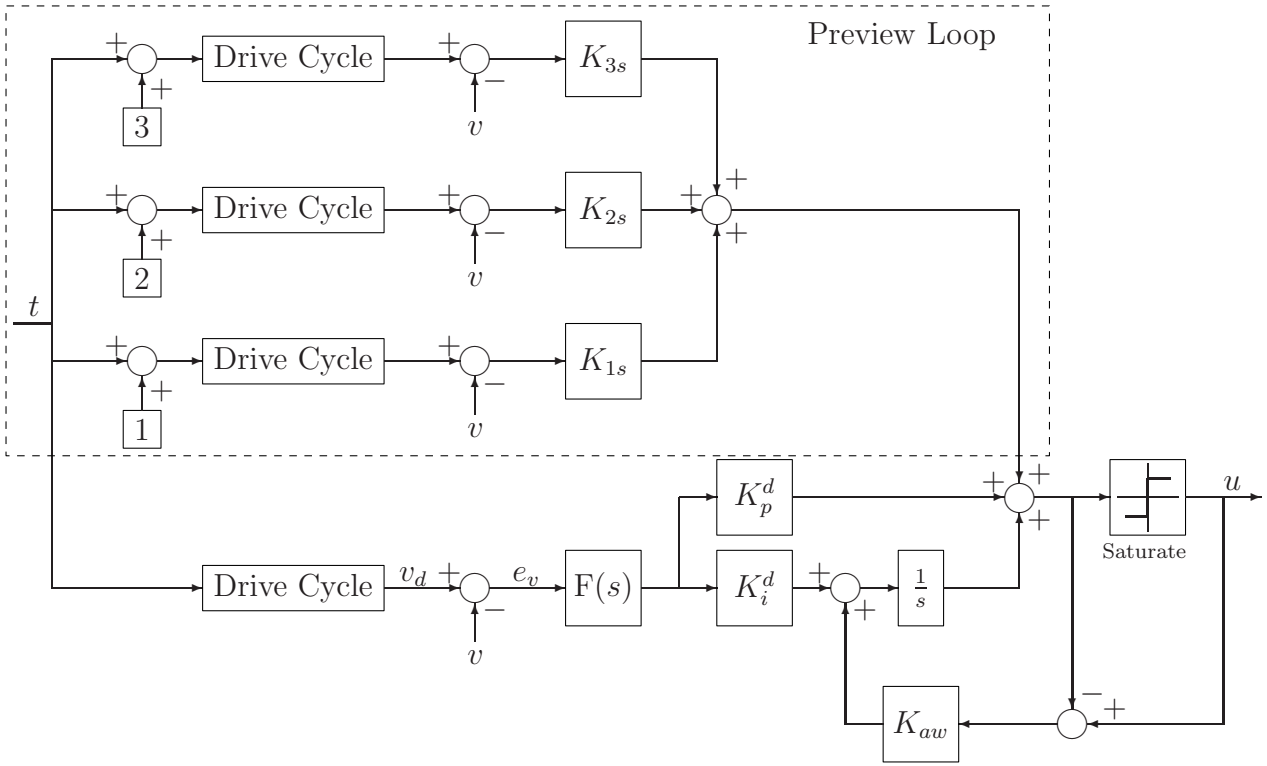

Figure C.6: Driver Model for EIL Experiments

APPENDIX D

Dynamic Wheel Slip Model for RT Simulation

This appendix presents a dynamic wheel slip model that can be used for RT simulation using fixed integration time step solvers. Since most hysteresis-based friction models found in the literature [194, 195] are not very conducive to RT-simulation, a simpler tire friction model is used to demonstrate this dynamic slip model in which the tire is modeled as an elastic band in the longitudinal direction [196]. The friction force of the tire, contributing to traction during acceleration, and braking force during deceleration, is dependent upon both the vehicle's longitudinal velocity, v, and tire's rotational velocity, ω. This effect is captured in the quantity, i, the slip coefficient. During acceleration, when $|v| < R|\omega|$, i can be calculated as

$$\frac{di}{dt} + \frac{R|\omega|}{l_r} i = \frac{R|\omega| - |v|}{l_r} \tag{D.1}$$

where l_r is the longitudinal relaxation length of the tire. This model captures the first-order longitudinal dynamics of the tire. Let T_w be the output torque of the half-shaft, J_w be the wheel's rotational inertia, M_b be the braking moment, F_x be the friction force from the tire in the longitudinal direction, R be the effective rolling radius of the tire, and M_r be the moment due to rolling resistance, then the wheel

dynamics are modeled as

$$J_w \frac{d\omega}{dt} = T_w - M_b - F_x R - M_r \tag{D.2}$$

It can be shown [197, 198] that the eigenvalues contributed by Equations (D.2) & (D.1), λ_{s_1,s_2}, are given by

$$\lambda_{s_1,s_2} = \frac{\frac{-|v|}{l_r} \pm \sqrt{\left(\frac{v}{l_r}\right)^2 + \frac{\partial F_x}{\partial i}\frac{4R^2 sgn(v)}{l_r}}}{2} \tag{D.3}$$

Hence, as the longitudinal velocity of the vehicle increases, the model becomes numerically stiff, and requires a smaller integration time-step (Section 4.3.1). This model cannot be used at all times, since for real-time simulation a fixed integration time-step is required. This problem is tackled by using the kinematic relationships for slip once a threshold velocity, V_{min}, is achieved. The complete slip model is shown in Figure D.1 in the form of a hybrid automaton. Please note that slip-coefficient $i \in [-1, 1]$, where negative values of i correspond to skid. When $i = 0$, then condition for pure rolling is satisfied, and $|v| = R|\omega|$; no braking or traction force can be produced by the tire in this case.

The traction/braking force is calculated assuming pure adhesion for low slips ($i < i_c$). After a critical slip, i_c is exceeded, the friction force is produced by both adhesion and sliding [196]. Let the longitudinal stiffness of the tire be C_i, the peak coefficient of friction be μ_p, and the coefficient of friction between the road and the tire be μ, then

$$F_x = iC_i \cdot sgn(v - R\omega) \quad \forall i < i_c \tag{D.4}$$

$$F_x = \mu(\mu_p, i)xmg(1 - \frac{\mu(\mu_p, i)xmg}{4iC_i})sgn(v - R\omega)\forall i \geq i_c \tag{D.5}$$

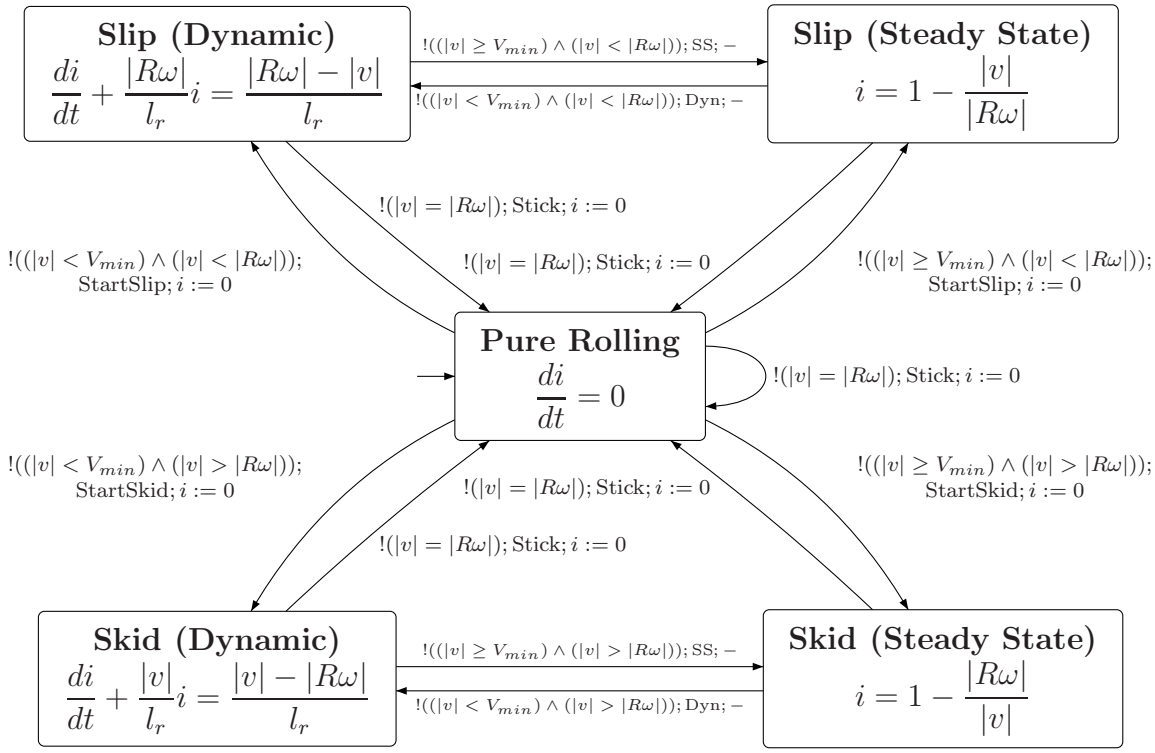

Figure D.1: Hybrid automaton representation of the slip model

This performance of this slip model is tested in simulation. One such testing scenario is presented in Figure D.2. The vehicle is given a full throttle step-input on a surface with high coefficient of friction. The slip increases instantaneously, but stabilizes to low values when higher vehicle velocities are reached. After 15 seconds of acceleration, the vehicle is suddenly braked. This results in wheel lockup, as represented by -100% slip before the vehicle comes to a complete rest.

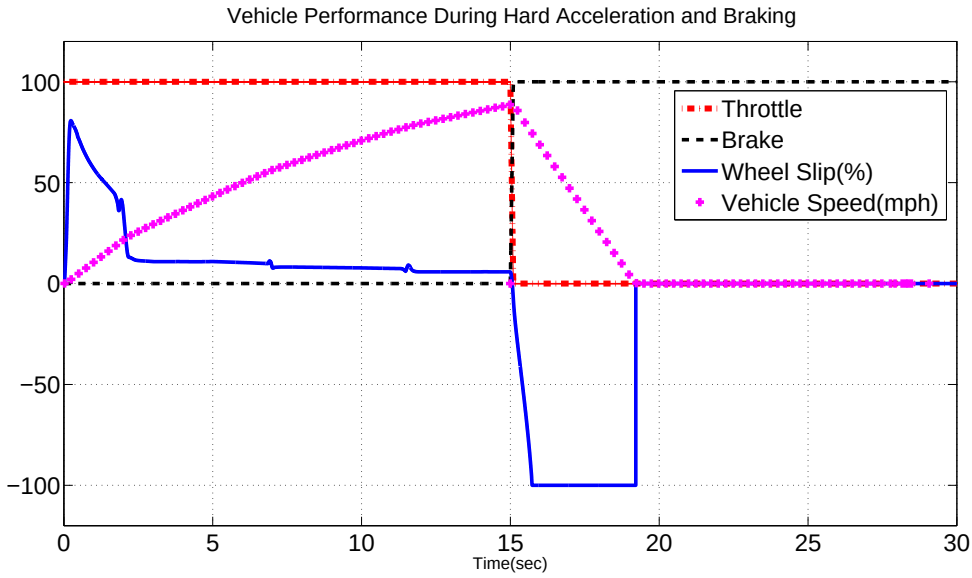

Figure D.2: Hard acceleration and braking test

APPENDIX E

Data Processing

The data used in this dissertation were obtained by the Engine-in-the-loop experiments conducted by Hagena [4]. The engine speed was recorded using the optical encoder and saved using PUMA, and the fuel flow rate was measured using a coriolis flow meter (see Appendix B). These data was exported at 10Hz and used without any processing. The particulates were recorded using Differential Mobility Spectrometer (DMS). Raw data from DMS contained the number of particles and their spectral weighting. A sample particulate spectral density curve is shown in Figure E.1. After the experiment, the total particle mass was calculated by discretizing the x-axis of the curve into particle diameter bins and then using the relationship

$$\text{Particle Mass} = 6.95 \times 10^{-3} \cdot D_p^{2.34} \cdot \text{Number of particles} \tag{E.1}$$

Here, D_p is the spectral diameter in nanometers. After the particle mass was calculated for each bin, the total mass was found by summing the masses in each bin and dividing by the number of bins per decade as an approximation for integration over a logarithmic scale.

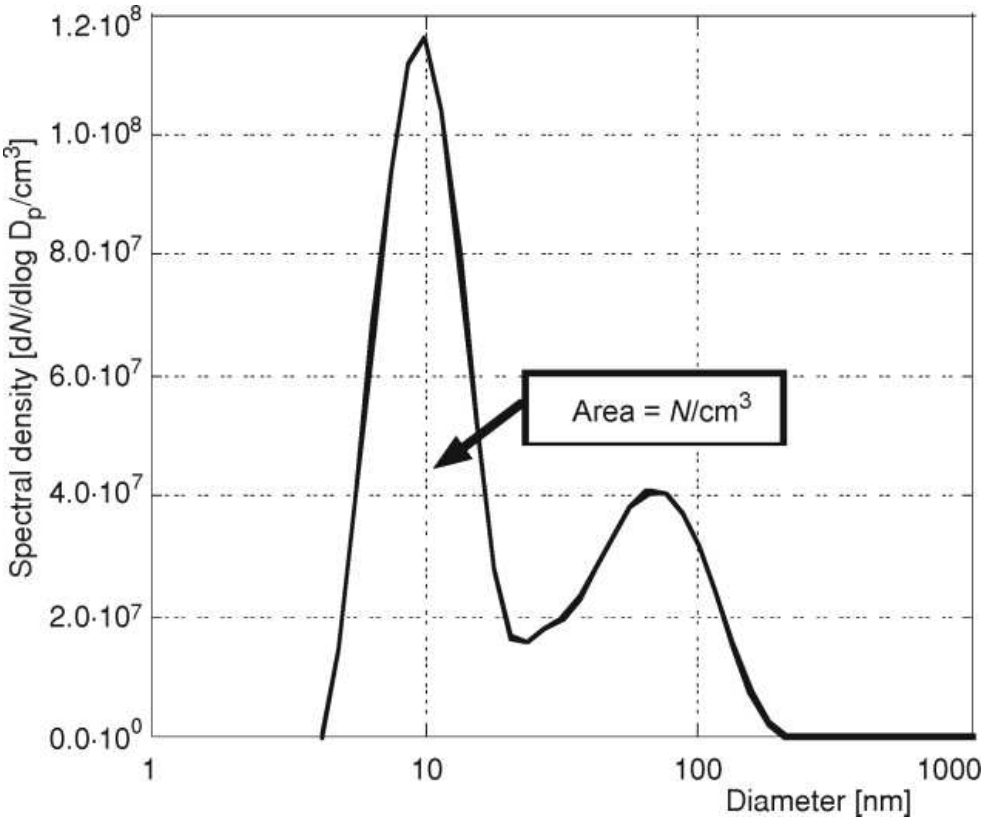

Figure E.1: Sample particulate spectral density curve [23]

Table E.1: Description of the datasets

Number	Description
1	Conventional vehicle
2	Conventional vehicle
3	Conventional vehicle with downsized engine
4	SDP parallel electric hybrid
5	SDP parallel electric hybrid with rate limit
6	SDP parallel electric hybrid with rate limit and compensation
7	SDP parallel electric hybrid
8	SDP parallel electric hybrid with rate limit and compensation
9	SDP parallel electric hybrid
10	SDP parallel electric hybrid with rate limit and compensation
11	SDP parallel electric hybrid
12	Smoothed SDP parallel electric hybrid
13	Series hydraulic hybrid
14	Series hydraulic hybrid
15	Series hydraulic hybrid
16	Low-idle series hydraulic hybrid
17	Optimized series hydraulic hybrid

$$\text{Total Mass} = \frac{\sum_{\text{Bins}} \text{Mass}}{\text{Bins/Decade}} [kg/m^3] \tag{E.2}$$

Time-resolved soot emissions were then obtained by multiplying this mass per unit volume with the volume flow rate. Separate computers were used to initialize DMS and PUMA recordings, and the differences in clock pulse synchronization were accounted by aligning the soot trace with the change in engine throttle command. After this processing, the datasets were saved at 10 Hz provided for this work. Interested readers are referred to [4] for further details.

There were 17 different datasets provided for this work. The description of the datasets is given in Table E.1. The inputs and output time traces for these datasets are shown in Figures E.2-E.18.

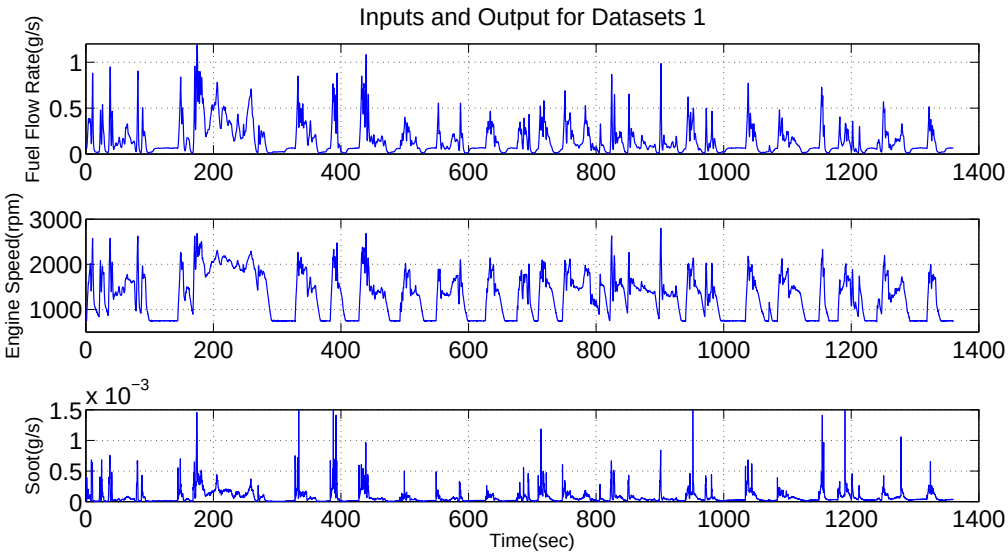

Figure E.2: Inputs and output for dataset 1

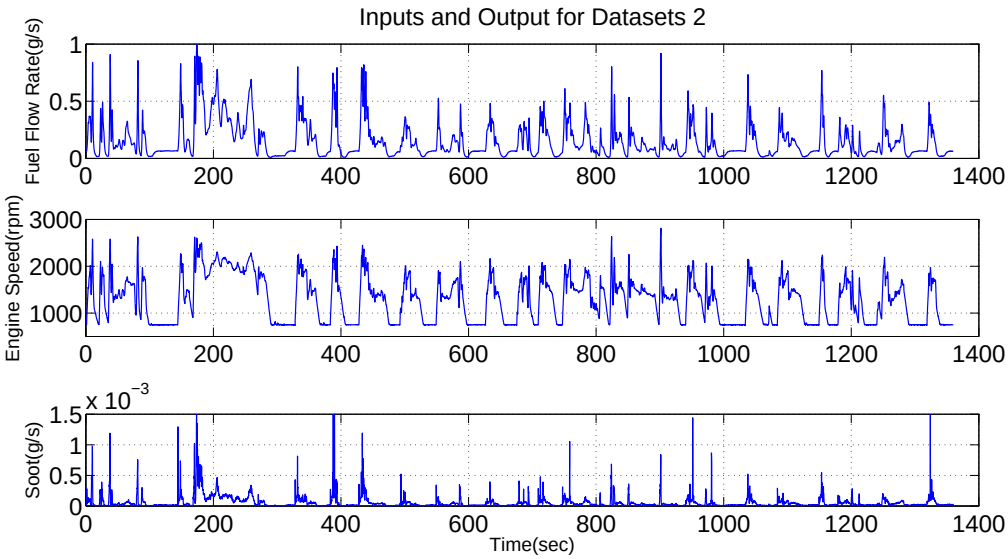

Figure E.3: Inputs and output for dataset 2

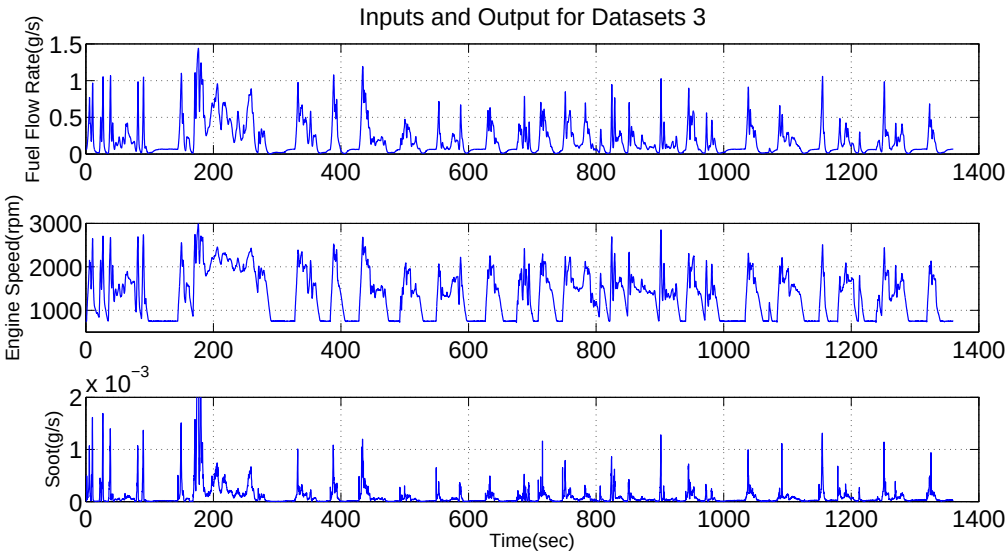

Figure E.4: Inputs and output for dataset 3

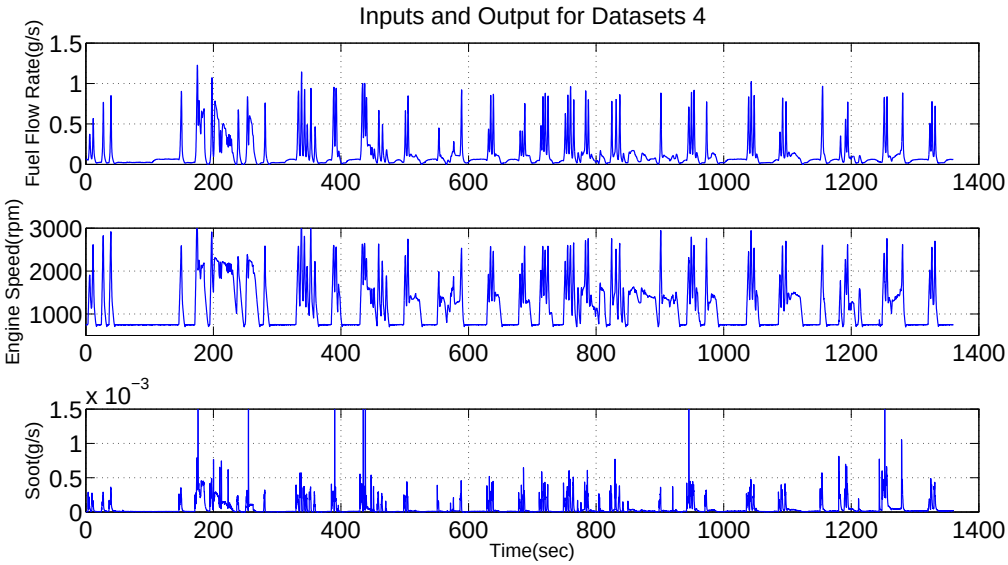

Figure E.5: Inputs and output for dataset 4

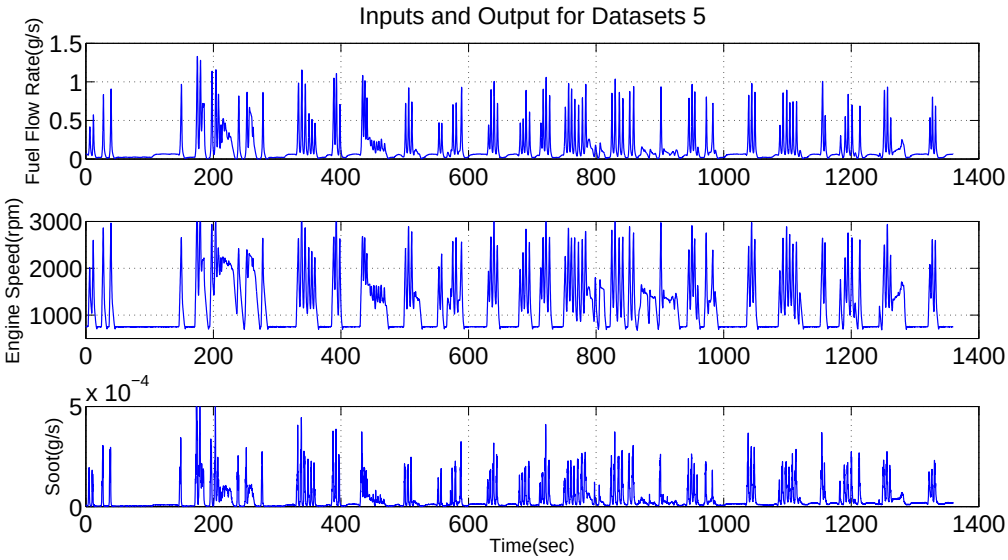

Figure E.6: Inputs and output for dataset 5

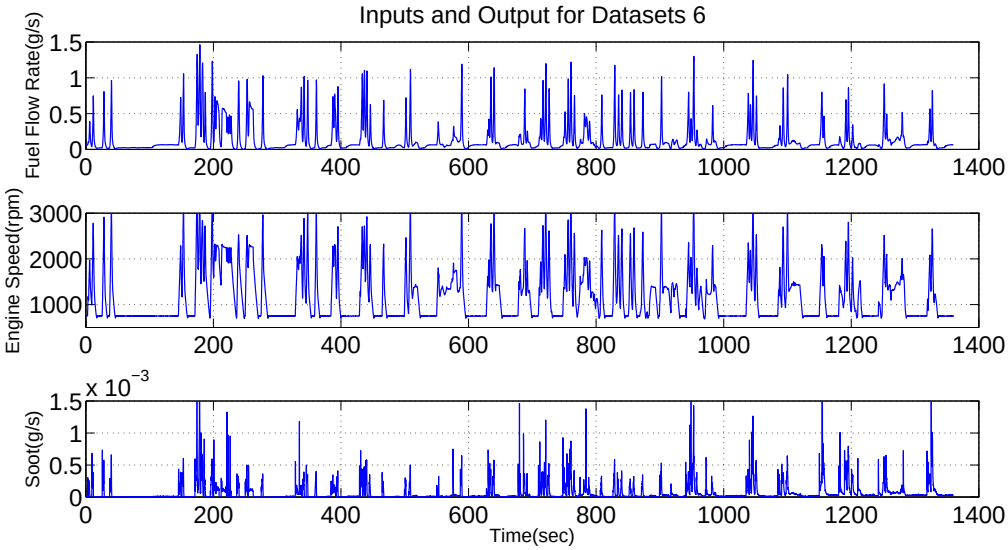

Figure E.7: Inputs and output for dataset 6

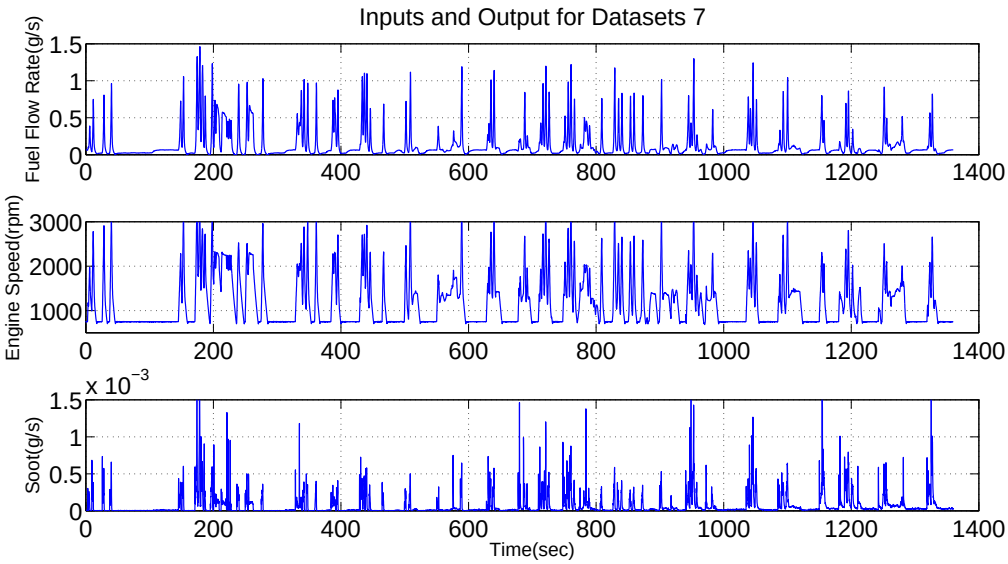

Figure E.8: Inputs and output for dataset 7

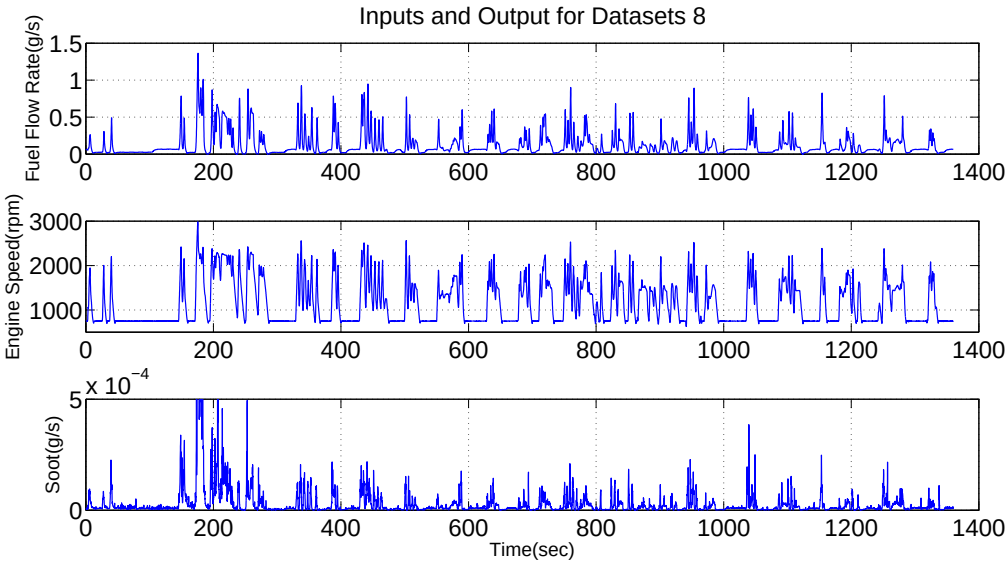

Figure E.9: Inputs and output for dataset 8

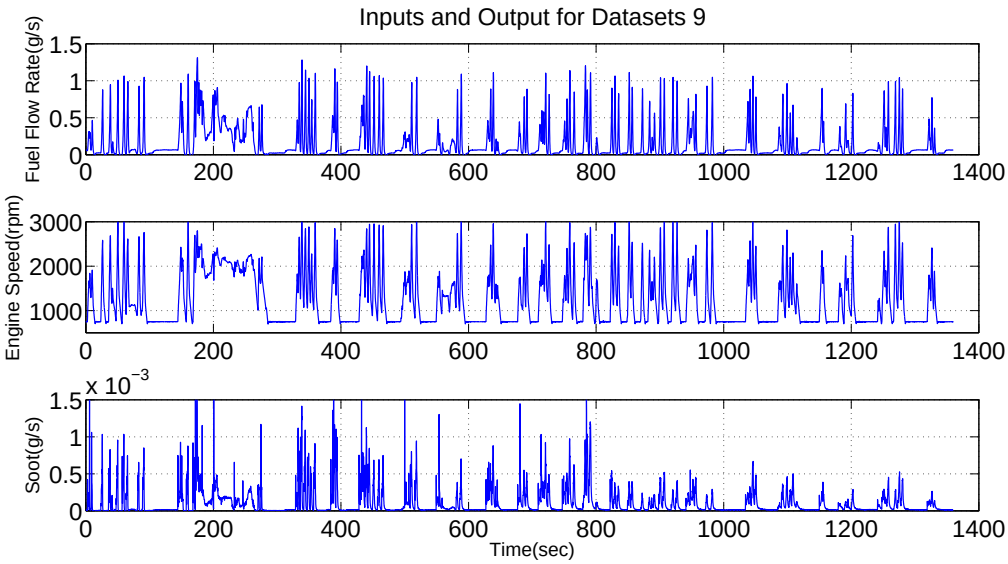

Figure E.10: Inputs and output for dataset 9

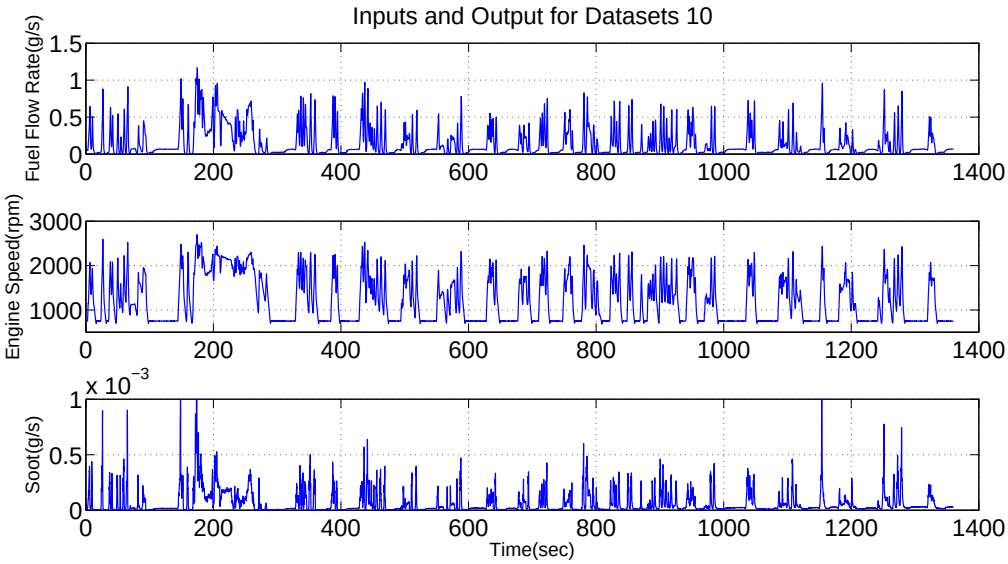

Figure E.11: Inputs and output for dataset 10

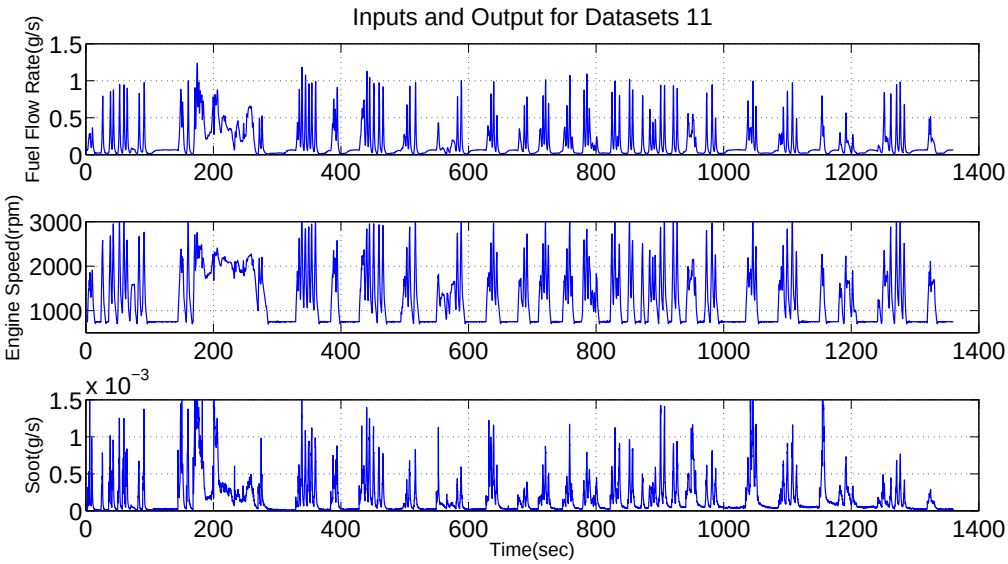

Figure E.12: Inputs and output for dataset 11

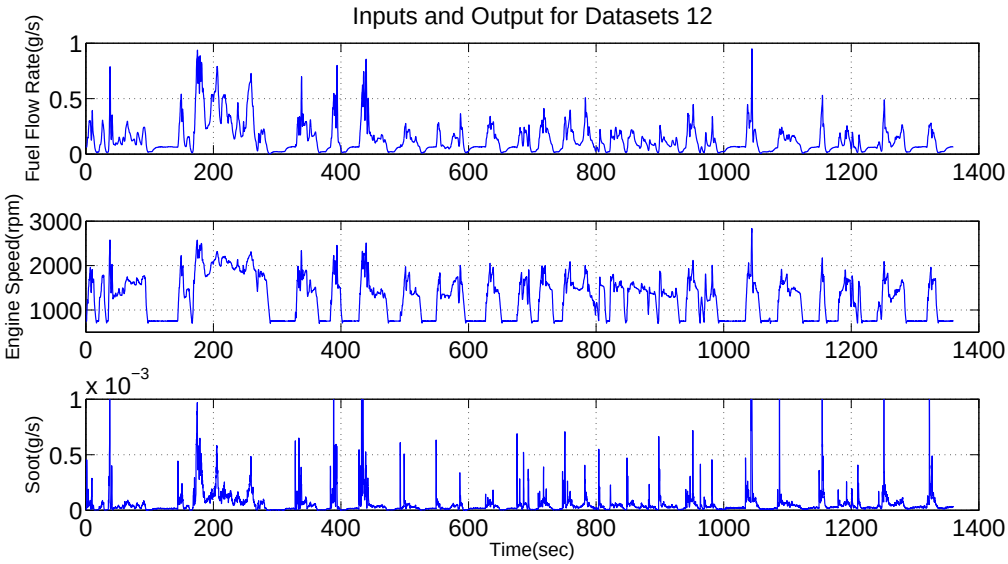

Figure E.13: Inputs and output for dataset 12

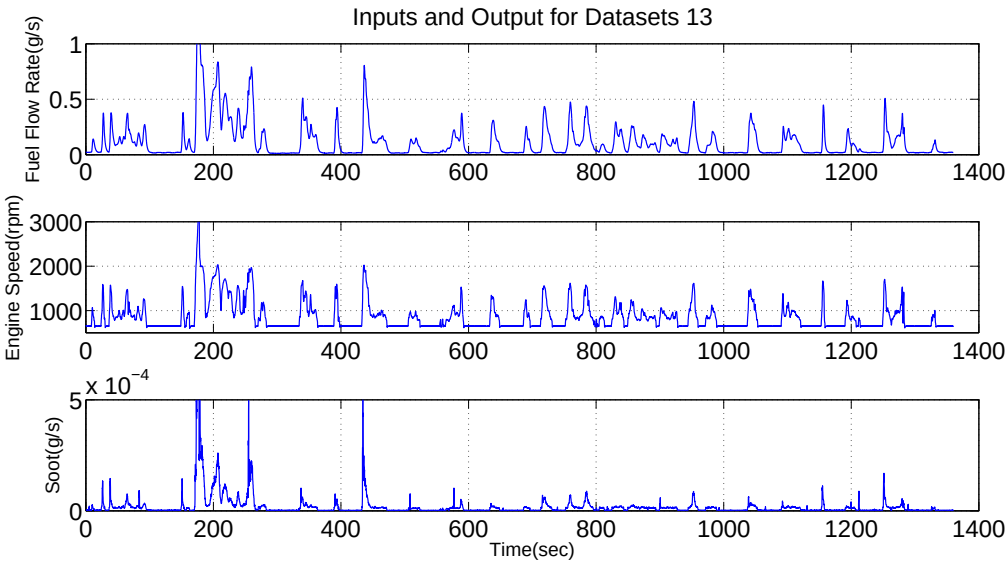

Figure E.14: Inputs and output for dataset 13

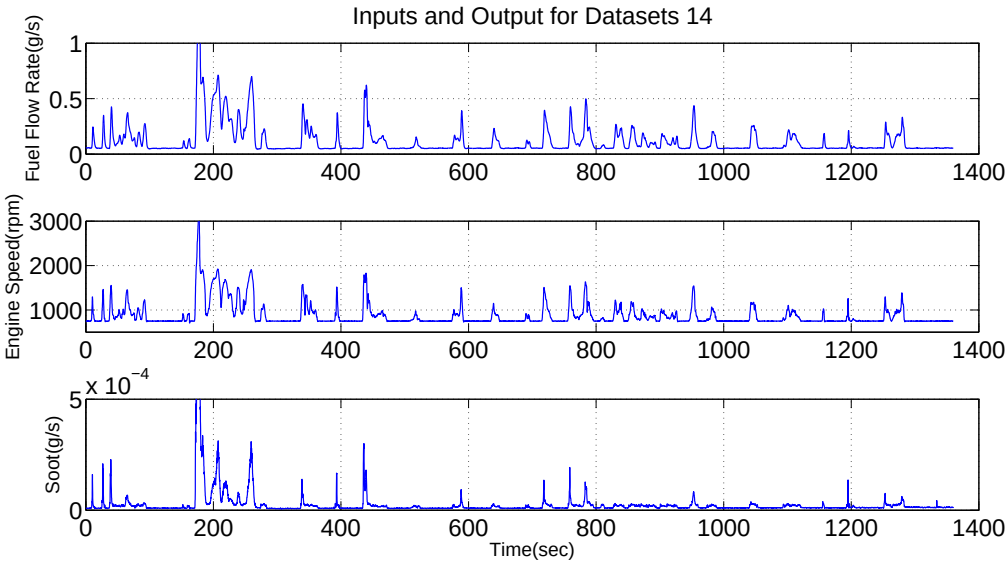

Figure E.15: Inputs and output for dataset 14

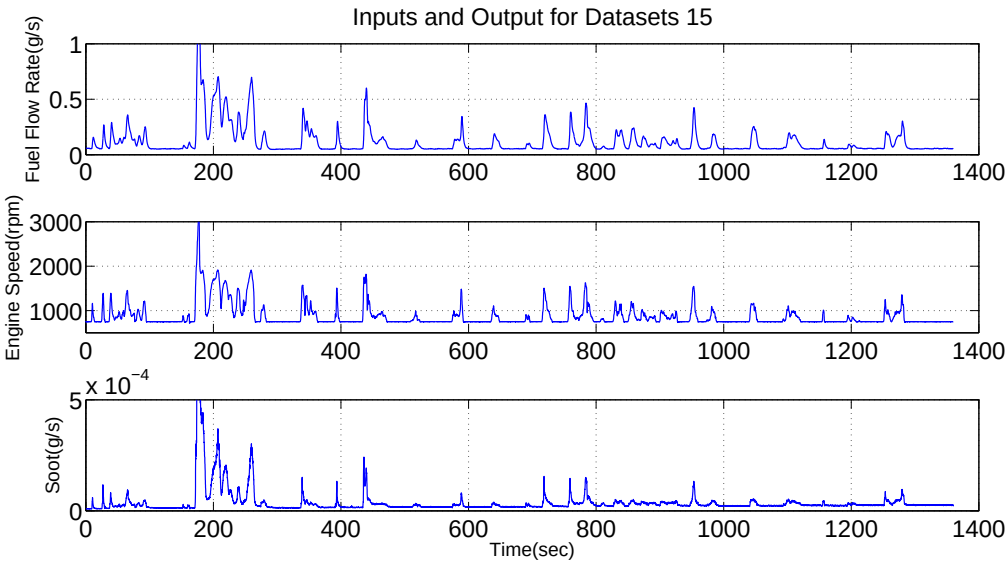

Figure E.16: Inputs and output for dataset 15

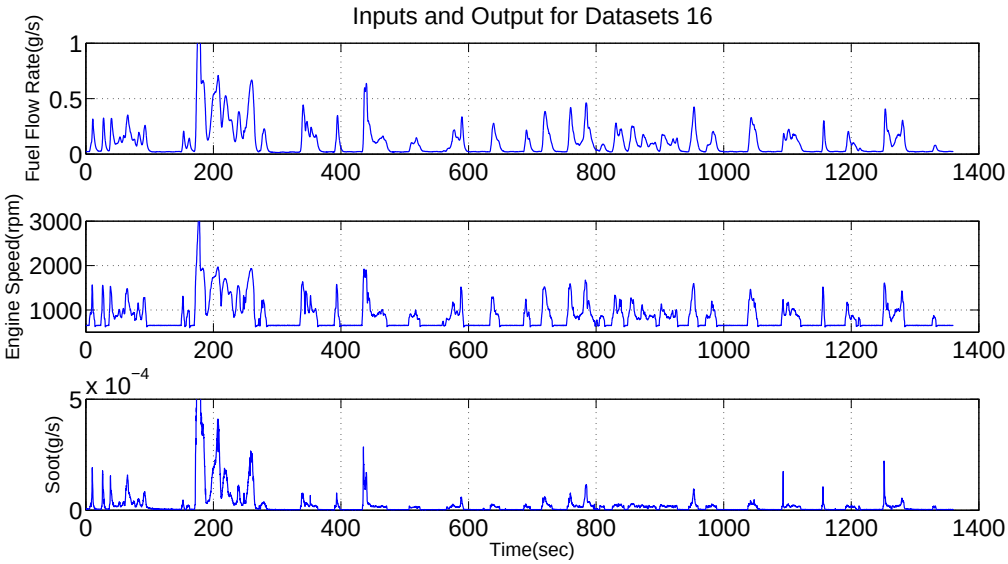

Figure E.17: Inputs and output for dataset 16

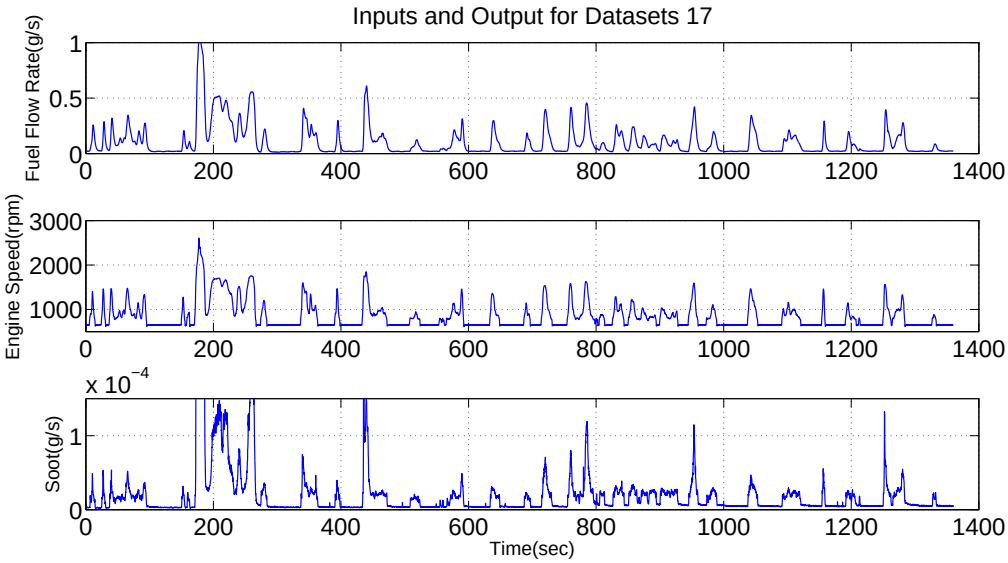

Figure E.18: Inputs and output for dataset 17

REFERENCES

REFERENCES

[1] J.A. Cook, Jing Sun, J.H. Buckland, I.V. Kolmanovsky, Huei Peng, and J.W. Grizzle. Automotive powertrain control - a survey. *Asian Journal of Control*, 8(3):237 – 60, September 2006.

[2] Zoran Filipi, Hosam Fathy, Jonathan Hagena, Alexander Knafl, Rahul Ahlawat, Jinming Liu, Dohoy Jung, Dennis Assanis, Huei Peng, and Jeffrey Stein. Engine-in-the-loop testing for evaluating hybrid propulsion concepts and transient emissions-HMMWV case study. *SAE Transactions, Journal of Commercial Vehicles*, 115, 2006.

[3] J. Boulanger, Fengshan Liu, W. S. Neill, and G. J. Smallwood. An improved soot formation model for 3D diesel engine simulations. *Transactions of the ASME: Journal of Engineering for Gas Turbines and Power*, 129(3):877–84, July 2007.

[4] Jonathan R. Hagena. *An experimental technique for determining cycle-resolved pre-combustion in-cylinder composition and its application towards the understanding of diesel engine emissions during transient operation.* PhD Dissertation (Mechanical Engineering), University of Michigan, Ann Arbor, 2008.

[5] A.C. Lloyd and T.A. Cackette. Diesel engines: Environmental impact and control. *Journal of the Air and Waste Management Association*, 51(6):809 – 847, 2001.

[6] Peter Eastwood. *Particulate Emissions from Vehicles.* John Wiley and Sons, Ltd., 2008.

[7] John B. Heywood. *Internal Conbustion Engine Fundamentals.* McGraw Hill, 1988.

[8] P.Q. Tan, Z.Y. Hu, K.Y. Deng, J.X. Lu, D.M. Lou, and G. Wan. Particulate matter emission modelling based on soot and SOF from direct injection diesel engines. *Energy Conversion and Management*, 48(2):510 – 18, 2007.

[9] John P.A. Neeft, Michiel Makkee, and Jacob A. Moulijn. Diesel particulate emission control. *Fuel processing technology*, 47(1):1 – 69, 1996.

[10] Jonathan Ray Hagena, Zoran S. Filipi, and Dennis N. Assanis. Transient diesel emissions: Analysis of engine operation during a tip-in. In *SAE World Congress and Exhibition*, Detroit, MI, April 2006.

[11] Kirchen Patrick Nicolas. *Steady-State and Transient Diesel Soot Emissions: Development of a Mean Value Soot Model and Exhaust-Stream and In-Cylinder Measurements*. Thesis (Doctor of Sciences), ETH Zurich, 2009.

[12] P.E. Schwarze, J. Ovrevik, M. Lag, M. Refsnes, P. Nafstad, R.B. Hetland, and E. Dybing. Particulate matter properties and health effects: consistency of epidemiological and toxicological studies. *Human and Experimental Toxicology*, 25(10):559–579, 2006.

[13] Timothy V. Johnson. Review of diesel emissions and control. *SAE International Journal of Fuels and Lubricants*, 3(1):16 – 29, 2010.

[14] Danish National Environmental Research Institute and the Center for Clean Air Policy. *Comparison of EU and US approaches towards the control of particulate matter*. Assessment of the Effectiveness of the European Air Quality Policies and Measures, 2004.

[15] Robert Bosch GmbH. *Diesel-Engine Management*. John Wiley & Sons, 4^{th} edition, 2005.

[16] Anders Westlund. *Measuring and Predicting Transient Diesel Engine Emissions*. Licentiate (Master's) thesis, KTH CICERO, Royal Institute of Technology, Stockholm, 2009.

[17] C. D. Rakopoulos, A. M. Dimaratos, E. G. Giakoumis, and D. C. Rakopoulos. Evaluation of the effect of engine, load and turbocharger parameters on transient emissions of diesel engine. *Energy Conversion and Management*, 50(9):2381–2393, 2009.

[18] Chintan Dilip Shah. *Particulate Matter Load Estimation in Diesel Particulate Filters*. Master's thesis (Mechanical Engineering), Purdue University, 2008.

[19] Kingsley S. Reavell, Tim Hands, and Nick Collings. A fast response particulate spectrometer for combustion aerosols. In *SAE Powertrain & Fluid Systems Conference & Exhibition*, number 2002-01-2714, San Diego, CA, October 2002.

[20] J. Keskinen, K. Pietarinen, and M. Lehtimaeki. Electrical low pressure impactor. *Journal of Aerosol Science*, 23(4):353 – 360, 1992.

[21] U. Lehmann, V. Niemela, and M. Mohr. New method for time-resolved diesel engine exhaust particie mass measurement. *Environmental Science & Technology*, 38(21):5704–5711, 2004.

[22] W. Schindler, C. Haisch, H.A. Beck, R. Niessner, E. Jacob, and D. Rothe. A photoacoustic sensor system for time resolved quantification of diesel soot emissions. In *SAE World Congress & Exhibition*, number 2002-01-2714, Detroit, MI, March 2004.

[23] Z. Filipi, J. Hagena, and H Fathy. Investigating the impact of in-vehicle transients on diesel soot emissions. *Thermal Science*, 12(1):53–72, 2008.

[24] Hosam K. Fathy, Rahul Ahlawat, and Jeffrey L. Stein. Proper powertrain modeling for engine-in-the-loop simulation. In *ASME International Mechanical Engineering Congress and Exposition*, volume 74 DSC, pages 1195–1201, Orlando, FL, United States, November 2005.

[25] N.N. Clark, M. Gautam, B.L. Rapp, D.W. Lyons, M.S. Graboski, R.L. McCormick, T.L. Alleman, and P. Norton. Diesel and CNG transit bus emissions characterization by two chassis dynamometer laboratories: Results and issues. *SAE transactions*, 108(4):801–812, 1999.

[26] I. Kolmanovsky, P. Morall, M. Van Nieuwstadt, and A. Stefanopoulou. Issues in modelling and control of intake flow in variable geometry turbocharged engines. *Chapman and Hall CRC research notes in mathematics*, pages 436–445, 1999.

[27] Dennis N. Assanis and John B. Heywood. Development and use of a computer simulation of the turbocompounded diesel system for engine performance and component heat transfer studies. *SAE Special Publications*, 860329:95 – 120, 1986.

[28] David E. Foster. An overview of zero-dimensional thermodynamic models for IC engine data analysis. *SAE Special Publications*, 852070, 1985.

[29] Dohoy Jung and D. N. Assanis. Quasidimensional modeling of direct injection diesel engine nitric oxide, soot, and unburned hydrocarbon emissions. *Transactions of the ASME: Journal of Engineering for Gas Turbines and Power*, 128(2):388–96, 04 2006.

[30] Hiroyuki Hiroyasu, Toshikazu Kadota, and Masataka Arai. Development and use of a spray combustion modeling to predict diesel engine efficiency and pollutant emissions: Part 2 computational procedure and parametric study. *Bulletin of the JSME*, 26(214):576 – 583, 1983.

[31] Joseph Bayer and David E. Foster. Zero-dimensional soot modeling. In *SAE World Congress & Exhibition*, number 2003-01-1070, Detroit, MI, March 2003.

[32] I.M. Khan, G. Greeves, and C.H.T. Wang. Factors affecting smoke and gaseous emissions from direct injection engines and a method of calculation. *SAE Preprints*, 730169, 1973.

[33] R. Farmer, R. Edelman, and E. Wong. Modeling soot emissions in combustion systems. *Particulate Carbon*, pages 229–320, 1981.

[34] A. Fusco, A. Knox-Kelecy, and D.E. Foster. Application of a phenomenological soot model to diesel engine combustion. In *International Symposium COMODIA*, volume 94, pages 571–576, 1994.

[35] P. Belardini, C. Bertoli, A. Ciajolo, A. D'Anna, and N. Del Giacomo. Three dimensional calculations of DI diesel engine combustion and comparison with in cylinder sampling valve data. In *SAE International Fuels & Lubricants Meeting & Exposition*, number 922225, San Francisco, CA, October 1992.

[36] A. Kazakov and D.E. Foster. Modeling of soot formation during DI diesel combustion using a multi-step phenomenological model. In *SAE International Fuels & Lubricants Meeting & Exposition*, number 982463, San Francisco, CA, October 1998.

[37] F. Tao, Y. Liu, B. Rempelewert, D.E. Foster, R.D. Reitz, D. Choi, and P. Miles. Modeling the effects of EGR and injection pressure on soot formation in a high-speed direct injection diesel engine using a multi-step phenomenological soot model. In *SAE World Congress & Exhibition*, number 2005-01-0121, Detroit, MI, April 2005.

[38] K.M. Leung, R.P. Lindstedt, and W.P. Jones. A simplified reaction mechanism for soot formation in nonpremixed flames. *Combustion And Flame*, 87(3-4):289–305, 1991.

[39] J. Nagle and R.F. Strickland-Constable. Oxidation of carbon between 1000 – 2000°C. In *Proceedings of the Fifth Conference on Carbon*, volume 1, pages 154–164, 1962.

[40] K. Akihama, Y. Takatori, K. Inagaki, S. Sasaki, and A. Dean. Mechanism of the smokeless rich diesel combustion by reducing temperature. In *SAE World Congress & Exhibition*, number 2001-01-0655, Detroit, MI, March 2001.

[41] O. Kaario, E. Antila, and M. Larmi. Applying soot phi-T maps for engineering CFD applications in diesel engines. In *SAE Powertrain & Fluid Systems Conference & Exhibition*, number 2005-01-3856, San Antonio, TX, October 2005.

[42] Haiyan Wang and Jundong Zhang. Control oriented dynamic modeling of a turbocharged diesel engine. In *Sixth International Conference on Intelligent Systems Design and Applications*, volume 2, pages 142 – 145, Jinan, China, 2006.

[43] A.G. Stefanopoulou, I. Kolmanovsky, and J.S. Freudenberg. Control of variable geometry turbocharged diesel engines for reduced emissions. *IEEE Transactions on Control Systems Technology*, 8(4):733 – 45, July 2000.

[44] R. Omran, R. Younes, and J.-C. Champoussin. Neural networks for real-time nonlinear control of a variable geometry turbocharged diesel engine. *International Journal of Robust and Nonlinear Control*, 18(12):1209 – 29, August 2008.

[45] R. Omran, R. Younes, and J.-C. Champoussin. Optimal control of a variable geometry turbocharged diesel engine using neural networks: applications on the etc test cycle. *IEEE Transactions on Control Systems Technology*, 17(2):380 – 93, March 2009.

[46] Patrick Kirchen, Konstantinos Boulouchos, and Peter Obrecht. Soot emission measurements and validation of a mean value soot model for common-rail diesel engines during transient operation. In *SAE Powertrains, Fuels and Lubricants Meeting*, Florence, Italy, June 2009.

[47] M. Warth, P. Obrecht, A. Bertola, and K. Boulouchos. Predictive phenomenological c. combustion modeling optimization on the basis of bio-inspired algorithms. In *SAE World Congress & Exhibition*, number 2005-01-1119, Detroit, MI, April 2005.

[48] X. Li and J. Wallace. A phenomenological model for soot formation and oxidation in direct-injection diesel engines. *SAE Publications*, 952428, 1995.

[49] M. Patterson, S.C. Kong, G. Hampson, and R.D. Reitz. Effects of fuel injection characteristics on diesel engine soot and NOx emissions. In *SAE World Congress & Exhibition*, number 940523, Detroit, MI, February 1994.

[50] M. Chan, D. Sudhakar, and R.D. Reitz. Modeling multiple injection and EGR effects on diesel engine emissions. In *SAE International Fuels & Lubricants Meeting & Exposition*, number 972864, Tulsa, OK, October 1997.

[51] Y. Liu, F. Tao, D.E. Foster, and R.D. Reitz. Application of a multiplestep phenomenological soot model to HSDI diesel multiple injection modeling. In *SAE World Congress & Exhibition*, number 2005-01-0924, Detroit, MI, April 2005.

[52] Chan-Chiao Lin, Huei Peng, Jessy W. Grizzle, and Jun-Mo Kang. Power management strategy for a parallel hybrid electric truck. *IEEE Transactions on Control Systems Technology*, 11(6):839–849, 2003.

[53] Khizer Tufail, P. Eastwood, T. Winstanley, S. Karagiogis, A. Darlington, Yannis Hardalupas, and Alexander Taylor. Deviations in emissions of NO and soot from steady-state, during transient operation of a common-rail diesel engine. In *9th International Conference on Engines and Vehicles*, Naples, Italy, 2009.

[54] Evangelos G. Giakoumis and Alexios I. Alafouzos. Comparative study of turbocharged diesel engine emissions during three different transient cycles. *International Journal of Energy Research*, 34(11):1002 – 1015, 2010.

[55] E. G. Giakoumis and A. I. Alafouzos. Study of diesel engine performance and emissions during a transient cycle applying an engine mapping-based methodology. *Applied Energy*, 87(4):1358–65, 04 2010.

[56] Stefan Hausberger, Johannes Rodler, Peter Sturm, and Martin Rexeis. Emission factors for heavy-duty vehicles and validation by tunnel measurements. *Atmospheric Environment*, 37(37):5237 – 5245, 2003.

[57] Rudolf Pischinger. *Emission functions for heavy duty vehicles.* Update of the Emission Functions for Heavy Duty Vehicles in the Handbook Emission Factors for Road Traffic, Federal Environmental Agency, Austria, 2003.

[58] Claes Ericson, Björn Westerberg, and Rolf Egnel. Transient emission predictions with quasi stationary models. In *SAE Powertrain & Fluid Systems Conference & Exhibition*, number 2005-01-3852, San Antonio, TX, October 2005.

[59] Michael Benz, Christopher H. Onder, and Lino Guzzella. Engine emission modeling using a mixed physics and regression approach. *Journal of Engineering for Gas Turbines and Power*, 132(4), 2010.

[60] M. Benz, M. Hehn, C.H. Onder, and L. Guzzella. Model-based actuator trajectories optimization for a diesel engine using a direct method. *Journal of Engineering for Gas Turbines and Power*, 133(3):032806–032815, March 2011.

[61] P.G. Eastwood, K. Tufail, T. Winstanley, A. Darlington, S. Karagiorgis, Y. Hardalupas, and A.M.K.P. Taylor. Estimation of deviations in NO and soot emissions between steady-state and EUDC transient operation of a common-rail diesel engine. *SAE International Journal of Engines*, 2(2):648 – 659, 2010.

[62] I.M Khan and G. Greeves. *A method for calculating the formation and combustion of soot in diesel engines.* Heat transfer in flames, Chapter 25, Washington, Scripta Book Co., 1974.

[63] N. Watson. Dynamic turbocharged diesel engine simulator for electronic control system development. *Transactions of the ASME. Journal of Dynamic Systems, Measurement and Control*, 106(1):27 – 45, March 1984.

[64] Dhananjay Anand. Transient soot emission modeling using linear siso model identification techniques. Technical Report ME590, University of Michigan, Ann Arbor, 2008.

[65] I. Arsie, C. Pianese, and G. Rizzoni. Enhancement of control oriented engine models using neural network. In *Proceedings of the 6th IEEE Mediterranean Conference on Theory and Practice of Control and Systems*, pages 465 – 71, Singapore, Singapore, 1998.

[66] Michael L. Traver and Christopher M. Atkinson, Richard J.and Atkinson. Neural network-based diesel engine emissions prediction using in-cylinder combustion pressure. In *SAE International Fuels & Lubricants Meeting & Exposition*, number 1999-01-1532, Dearborn, MI, May 1999.

[67] M. Ouladsine, G. Bloch, and X. Dovifaaz. Neural modelling and control of a diesel engine with pollution constraints. *Journal of Intelligent and Robotic Systems: Theory and Applications*, 41(2-3):157 – 71, September 2004.

[68] Yongsheng He. *Development of a Diesel Engine Simulation Tool Using Artificial Neural Networks*. Doctoral Thesis (Mechanical Engineering), University of Wisconsin, Madison, 2002.

[69] I. Brahma, C.J. Rutland, D.E. Foster, and Y. He. A new approach to system level soot modeling. In *SAE World Congress & Exhibition*, number 2005-01-1122, Detroit, MI, April 2005.

[70] Indranil Brahma. *Data Driven System Level Modeling for Diesel Engines*. Doctoral Thesis (Mechanical Engineering), University of Wisconsin, Madison, 2005.

[71] R. Johri, A. Salvi, and Z. Filipi. Virtual sensors for transient diesel soot and NOx emissions: Neuro-fuzzy model tree with automatic relevance determination. In *IEEE Conference on Decision and Control*, December 2011.

[72] Eva Ericsson. Independent driving pattern factors and their influence on fuel-use and exhaust emission factors. *Transportation Research Part D: Transport and Environment*, 6(5):325 – 345, 2001.

[73] Marc Ross. Automobile fuel consumption and emissions. effects of vehicle and driving characteristics. *Annual Review of Energy and the Environment*, 19:75 – 75, 1994.

[74] B.A. Holmén and D.A. Niemeier. Characterizing the effects of driver variability on real-world vehicle emissions. *Transportation Research Part D: Transport and Environment*, 3(2):117 – 128, 1998.

[75] Stefano Cassani, Davide Mercuri, Simone Barbero, and Pierluigi Rellecati. *Method for regenerating a diesel particulate filter*. US Patent 20110066354, March, 2011.

[76] Stefano Cassani, Simone Barbero, Davide Mercuri, and Pierluigi Rellecati. *Estimation of the soot load of a particulate filter*. European Patent EP2090767, August, 2009.

[77] M. Van Nieuwstadt, D. Upadhyay, M. Goebelbecker, and W. Ruona. Experiments in active diesel particulate filter regeneration. *SAE Transactions*, 112(2):48–55, 2003.

[78] S. Jain and P. Tsiotras. Trajectory optimization using multiresolution techniques. *Journal of Guidance, Control, and Dynamics*, 31(5):1424 – 1436, 2008.

[79] J.T. Betts. Survey of numerical methods for trajectory optimization. *Journal of Guidance, Control, and Dynamics*, 21(2):193 – 207, March 1998.

[80] J.P.M. Hendrikx, T.J.J. Meijlink, and R.F.C. Kriens. Application of optimal control theory to inverse simulation of car handling. *Vehicle System Dynamics*, 26(6):449 – 461, 1996.

[81] G. Prokop. Modeling human vehicle driving by model predictive online optimization. *Vehicle System Dynamics*, 35(1):19–53, 01 2001.

[82] Chan-Chiao Lin, Soonil Jeon, Huei Peng, and Jang Moo Lee. Driving pattern recognition for control of hybrid electric trucks. *Vehicle System Dynamics*, 42(1-2):41–58, 2004.

[83] Efstathios Velenis, Panagiotis Tsiotras, and Jianbo Lu. Optimality properties and driver input parameterization for trail-braking cornering. *European Journal of Control*, 14(4):308 – 320, 2008.

[84] T.J. Gordon and M.C. Best. On the synthesis of driver inputs for the simulation of closed-loop handling manoeuvres. *International Journal of Vehicle Design*, 40(1-3):52 – 76, 2006.

[85] E.D. Tate, J.W. Grizzle, and Huei Peng. SP-SDP for fuel consumption and tailpipe emissions minimization in an EVT hybrid. *IEEE Transactions on Control Systems Technology*, 18(3):673 – 87, May 2010.

[86] Kai Cao, Jin Jun Tang, and Lu Lu Zhou. Driving behavior control based on an on-line learning algorithm. In *4th International Conference on Natural Computation*, volume 4, pages 368–372, 2008.

[87] Xiaobing Chen and Weigong Zhang. Robot driver for vehicle durability emission test on chassis dynamometer. *Journal of Southeast University (English Edition)*, 21(1):33–38, 2005.

[88] A. Carlsson and H.-C. Reuss. A learning vehicle for forward-looking driving. *VDI Berichte*, (1931):109 – 119, 2006.

[89] A. Carlsson, G. Baumann, and H.C. Reuss. Implementation of a self-learning route memory as an electronic co-driver for reduced emissions. In *FISITA world automotive congress*, Munich, Germany, September 2008.

[90] T.J. Gordon, M.C. Best, and P.J. Dixon. An automated driver based on convergent vector fields. *Proceedings of the Institution of Mechanical Engineers, Part D: Journal of Automobile Engineering*, 216(4):329 – 347, 2002.

[91] MC van der Voort and M. van Maarseveen. Reducing fuel consumption and emissions in urban areas by using a new fuel-efficiency support tool. *Urban Transport VI: Urban transport and the environment in the* 21^{st} *century*, 8(8):631–640, 2001.

[92] Andreas A. Malikopoulos, Dennis N. Assanis, and Panos Y. Papalambros. Real-time self-learning optimization of diesel engine calibration. *Journal of Engineering for Gas Turbines and Power*, 131(2), 2009.

[93] Modeling and analysis of automatic transmission engagement dynamics-nonlinear case including validation. *Journal of Dynamic Systems, Measurement and Control, Transactions of the ASME*, 128(2):251 – 262, 2006.

[94] Jeffrey K. Runde. *Modeling and Control of an Automatic Transmission*. Masters Thesis (Mechanical Engineering), Massachusetts Institute of Technology, 1986.

[95] Scott A. Munns. *Computer Simulation of Powertrain Components with Methodologies for Generalized System Modeling*. Masters Thesis (Mechanical Engineering), University of Wisconsin, Madison, 1996.

[96] J. Deur, J. Asgari, D. Hrovat, and P. Kovač. Modeling and analysis of automatic transmission engagement dynamics-linear case. *Transactions of the ASME. Journal of Dynamic Systems, Measurement and Control*, 128(2):263 – 277, June 2006.

[97] Quan Zheng, Woowon Chung, Ken Defore, and Andrew Herman. A hardware-in-the-loop test bench for production transmission controls software quality validation. In *SAE World Congress & Exhibition*, number 2007-01-0502, Detroit, MI, April 2007.

[98] Heribert Scherer and Georg Gierer. ZF 5-speed transmissions for passenger cars. *SAE Special Publications*, 1241:89 – 97, 1997.

[99] D. Cho and J.K. Hedrick. Automotive powertrain modeling for control. *Journal of Dynamic Systems, Measurement and Control, Transactions of the ASME*, 111(4):568 – 576, 1989.

[100] B. Klages, R.J. Woermann, and H.J. Theuerkauf. Improved real-time model of a planetary gear train. *SAE Special Publications*, 1241(970970):113 – 120, 1997.

[101] Chung-Hung Pan and John J. Moskwa. Dynamic modeling and simulation of the ford AOD automobile transmission. In *SAE World Congress & Exhibition*, number 950899, Detroit, MI, February 1995.

[102] A. Hosl, J. Post, and F. Pfeiffer. Simulation of a Ravigneaux planetary gear of an automatic transmission. *VDI Berichte*, 1(1665):491 – 506, 2002.

[103] M. Otter, C. Schlegel, and H. Elmqvist. Modeling and realtime simulation of an automatic gearbox using modelica. In *Simulation in Industry: 9th European Simulation Symposium*, pages 115 – 21, Passau, Germany, 1997.

[104] Gerhard Wagner and P. Lepelletier. The Lepelletier 6-speed planetary geartype system. *VDI Berichte*, (1704):329 – 348, 2002.

[105] D. Kusamoto, Y. Yasuda, K. Watanabe, H. Kimura, and A. Hoshino. Toyota's new six-speed automatic transaxle U660E for FWD vehicles. In *SAE World Congress & Exhibition*, number 2006-01-0847, Detroit, MI, April 2006.

[106] Howard L. Benford and Maurice B. Leising. Lever analogy: A new tool in transmission analysis. *SAE Preprints*, (810102), 1981.

[107] A.K. Tugcu, K.V. Hebbale, A.A. Alexandridis, and A.M. Karmel. Modeling and simulation of the powertrain dynamics of vehicles equipped with automatic transmission. In *Proceedings of the American Society of Mechanical Engineers, Applied Mechanics Division*, volume 80, pages 39 – 61, Anaheim, CA, 1986.

[108] A.M. Karmel. A methodology for modeling the dynamics of the mechanical paths of automotive drivetrains with automatic step-transmissions. In *Proceedings of the American Control Conference*, pages 279 – 284, Seattle, WA, 1986.

[109] Je-Kee Lee, Huei Peng, and Yeong-Il Park. Modeling of a 5-speed automatic transmission for shift-quality control. In *Proceedings of the ASME Dynamic Systems and Control Division*, pages 661 – 669, 1997.

[110] Jinming Liu and Huei Peng. Modeling and control of a power-split hybrid vehicle. *IEEE Transactions on Control Systems Technology*, 16(6):1242 – 51, November 2008.

[111] Jung-Ho Kim and Dong-Il Dan Cho. An automatic transmission model for vehicle control. In *IEEE Conference on Intelligent Transportation Systems*, pages 759 – 764, 1997.

[112] John Patrick Absmeier. *Automatic Transmission Modeling and Controller Development*. Masters Thesis (Mechanical Engineering), University of California, Berkeley, 1999.

[113] Y. Zhang, Z. Zou, X. Chen, X. Zhang, and W. Tobler. Modeling and analysis of vehicle transmissions in modelica/dymola environment. In *Proceedings of the ASME Design Engineering Technical Conference*, volume 1, pages 843 – 850, Montreal, Canada, 2002.

[114] Woosung Han and Seung-Jong Yi. A study of shift control using the clutch pressure pattern in automatic transmission. volume 217, pages 289 – 298, 2003.

[115] Kyung-Jinn Yang, Keum-Shik Hong, and Dong-Il Cho. A robust control for engine and transmission systems: Enhancement of shift quality. *JSME International Journal, Series C: Mechanical Systems, Machine Elements and Manufacturing*, 44(3):697 – 707, 2001.

[116] Bengt Jacobson. *Gear Shifting with Retained Power Transfer*. Doctoral Dissertation (Machine and Vehicle Design), Chalmers University of Technology, Sweden, 1993.

[117] S. Orzelowski and J. Wicher. On the influence of friction clutch design on its ability to transmit torque. *International Journal of Vehicle Design*, 24(2):171 – 181, 2000.

[118] Yuji Fujii, William E. Tobler, Gregory M. Pietron, Ming Cao, and K. W. Wang. Review of wet friction component models for automatic transmission shift analysis. In *SAE Noise & Vibration Conference & Exhibition*, number 2003-01-1665, Traverse City, MI, May 2003.

[119] B. Armstrong-Helouvry, P. Dupont, and C. Canudas De Wit. A survey of models, analysis tools and compensation methods for the control of machines with friction. *Automatica*, 30(7):1083 – 138, July 1994.

[120] Levine. *The control handbook*. CRC & IEEE press, 1996.

[121] D. Margolis. Fixed causality slip-stick friction models for use in simulation of non-linear systems. *Proceedings of the Institution of Mechanical Engineers.Part I: Journal of Systems and Control Engineering*, 219(3):199–206, 2005.

[122] D.A. Haessig Jr. and B. Friedland. On the modeling and simulation of friction. *Journal of Dynamic Systems, Measurement and Control, Transactions of the ASME*, 113(3):354 – 362, 1991.

[123] Dean Karnopp. Computer simulation of stick-slip friction in mechanical dynamic systems. *Journal of Dynamic Systems, Measurement and Control, Transactions ASME*, 107(1):100–103, 1985.

[124] H. Olsson, K.J. Åström, C. Canudas de Wit, M. Gafvert, and P. Lischinsky. Friction models and friction compensation. *European Journal of Control*, 4(3):176 – 95, 1998.

[125] A. Padthe, B. Drincic, Jinhyoung Oh, D. Rizos, S. Fassois, and D. Bernstein. Duhem modeling of friction-induced hysteresis: experimental determination of gearbox stiction. *IEEE Control Systems Magazine*, 28(5):90 – 107, October 2008.

[126] C.Canudas de Wit, H. Olsson, K.J. Åström, and P. Lischinsky. New model for control of systems with friction. *IEEE Transactions on Automatic Control*, 40(3):419 – 425, 1995.

[127] M. Cao, K.W. Wang, Y. Fujii, and W.E. Tobler. Advanced hybrid neural network automotive friction component model for powertrain system dynamic analysis. part 1: Model development. *Proceedings of the Institution of Mechanical Engineers, Part D: Journal of Automobile Engineering*, 218(8):831 – 843, 2004.

[128] J. Awrejcewicz and P. Olejnik. Analysis of dynamic systems with various friction laws. *Applied Mechanics Review*, 58(6):389 – 411, 2005/11/.

[129] Tetsuji Kozaki, Hiroshi Moro, Hosam K. Fathy, and Swaminathan Gopalswamy. Balancing the speed and fidelity of automotive powertrain models through surrogation. In *American Society of Mechanical Engineers, Dynamic Systems and Control Division*, volume 73, pages 249 – 258, Anaheim, CA, 2004.

[130] F. Jamzadeh, T.M. Hsieh, and K. Struthers. Dynamic simulation modeling for heavy duty automatic transmission control development. In *SAE International Truck & Bus Meeting & Exposition*, number 922441, Toledo, OH, November 1992.

[131] N. Zhang, D.K. Liu, J.M. Jeyakumaran, and L. Villanueva. Modelling of dynamic characteristics of an automatic transmission during shift changes. *Proceedings of the Institution of Mechanical Engineers, Part I (Journal of Systems and Control Engineering)*, 216(I4):331 – 41, 2002.

[132] Dennis Assanis, Zoran Filipi, Steve Gravante, Dan Grohnke, Xinqun Gui, Loucas Louca, Geoff Rideout, Jeffrey Stein, and Yongsheng Wang. Validation and use of SIMULINK integrated, high fidelity, engine-in-vehicle simulation of the international class VI truck. In *SAE World Congress and Exhibition, Detroit, MI*, number 2000-01-0288, Detroit, MI, April 2000.

[133] J.R.P. Kusters. *Modelling and Coordinated Control of Advanced Automatic Transmission*. Masters Thesis (Mechanical Engineering), Eindhoven University of Technology, Netherlands, 2005.

[134] Kenji Hagiwara, Satoshi Terayama, Youhei Takeda, Ko Yoda, and Shoichi Suzuki. Development of automatic transmission control system using hardware-in-the-loop simulation system. *JSAE Review*, 23(1):55 – 59, 2002.

[135] Sarawoot Watechagit. *Modeling and Estimation of Stepped Automatic Transmission with Clutch-to-clutch Shift Technology*. Doctoral Dissertation (Mechanical Engineering), The Ohio State University, 2004.

[136] T. Ersal, H.K. Fathy, D.G. Rideout, L.S. Louca, and J.L. Stein. A review of proper modeling techniques. *Journal of Dynamic Systems, Measurement and Control*, 130(6):6100801–6100813, 2008.

[137] Douglas A. Bristow, Marina Tharayil, and Andrew G. Alleyne. A survey of iterative learning control: A learning-based method for high-performance tracking control. *IEEE Control Systems Magazine*, 26(3):96–114, 2006.

[138] Sangjin Hong, Margaret S. Wooldridge, Hong G. Im, Dennis N. Assanis, and Heinz Pitsch. Development and application of a comprehensive soot model for 3D CFD reacting flow studies in a diesel engine. *Combustion and Flame*, 143(1-2):11 – 26, 2005.

[139] Xander Seykens, Rik Baert, Bart Somers, and Frank Willems. Experimental validation of extended NO and soot model for advanced HD diesel engine combustion. In *SAE World Congress & Exhibition*, number 2009-01-0683, Detroit, MI, April 2009.

[140] Jincai Zheng and Qianfan Xin. Theoretical analysis of diesel engine NOx and soot with heuristic macro-parameter-dependent approach and virtual multi-zone real-time models. In *SAE Commercial Vehicle Engineering Congress & Exhibition*, number 2009-01-2836, Rosemont, IL, October 2009.

[141] Y. He and C.J. Rutland. Application of artificial neural networks in engine modelling. *International Journal of Engine Research*, 5(4):281 – 296, 2004.

[142] Jinming Liu, J. Hagena, Huei Peng, and Z.S. Filipi. Engine-in-the-loop study of the stochastic dynamic programming optimal control design for a hybrid electric HMMWV. *International Journal of Heavy Vehicle Systems*, 15(2-4):309 – 26, 2008.

[143] Z. Filipi and Y. Kim. Hydraulic hybrid propulsion for heavy vehicles: Combining the simulation and engine-in-the-loop techniques to maximize the fuel economy and emission benefits. *Oil & Gas Science and Technology - Revue de l'Institut Français du Pétrole*, 65(1):155–178, 2010.

[144] Rolf Johansson. *System modeling and identification*. Prentice Hall information and system sciences series, 1993.

[145] K Yacoub. Relationship between multiple and partial coherence functions. *IEEE Transactions on Information Theory*, IT-16(6):668 – 672, 1970.

[146] E.J. Perreault, R.F. Kirsch, and A.M. Acosta. Multiple-input, multiple-output system identification for characterization of limb stiffness dynamics. *Biological Cybernetics*, 80(5):327–37, 1999.

[147] E. Bedrosian and S.O. Rice. The output properties of volterra systems (nonlinear systems with memory) driven by harmonic and gaussian inputs. *Proceedings of the IEEE*, 59(12):1688 – 708, 1971.

[148] B. Angerer, C. Hintz, and D. Schroder. Online identification of a nonlinear mechatronic system. *Control Engineering Practice*, 12(11):1465 – 78, 2004.

[149] Valerie Pommier, Jocelyn Sabatier, Patrick Lanusse, and Alain Oustaloup. Crone control of a nonlinear hydraulic actuator. *Control Engineering Practice*, 10(4):391 – 402, 2002.

[150] S. Boyd and L. O. Chua. Fading memory and the problem of approximating nonlinear operators with volterra series. *IEEE Transactions on Circuits and Systems*, CAS-32(11):1150–61, November 1985.

[151] L. M. Li and S. A. Billings. Discrete time subharmonic modelling and analysis. *International Journal of Control*, 78(16):1265–84, November 2005.

[152] C. Seretis and E. Zafiriou. Nonlinear dynamical system identification using reduced volterra models with generalised orthonormal basis functions. In *Proceedings of the IEEE American Control Conference*, volume 5, pages 3042–6, Evanston, IL, June 1997.

[153] A. da Rosa, R. Campello, and W. Amaral. An optimal expansion of volterra models using independent kautz bases for each kernel dimension. *International Journal of Control*, 81(6):962–75, June 2008.

[154] R.J.G.B. Campello, G. Favier, and W.C. do Amaral. Optimal expansions of discrete-time volterra models using laguerre functions. *Automatica*, 40(5):815–22, 2004.

[155] Dong Song, R. H. M. Chan, V. Z. Marmarelis, R. E. Hampson, S. A. Deadwyler, and T. W. Berger. Nonlinear dynamic modeling of spike train transformations for hippocampal-cortical prostheses. *IEEE Transactions on Biomedical Engineering*, 54(6):1053–66, 06 2007.

[156] Qingsheng Zheng and Evanghelos Zafiriou. Volterra-laguerre models for nonlinear process identification with application to a fluid catalytic cracking unit. *Industrial and Engineering Chemistry Research*, 43(2):340–348, 2004.

[157] P.S.C. Heuberger, P.M.J. Van den Hof, and O.H. Bosgra. A generalized orthonormal basis for linear dynamical systems. *IEEE Transactions on Automatic Control*, 40(3):451 – 65, 1995.

[158] M. Plöchl and J. Edelmann. Driver models in automobile dynamics application. *Vehicle System Dynamics*, 45(7-8):699–741, 07 2007.

[159] C.C. MacAdam. Application of an optimal preview control for simulation of closed-loop automobile driving. *IEEE Transactions on Systems, Man and Cybernetics*, SMC-11(6):393 – 9, 1981.

[160] R. Ahlawat, H.K. Fathy, B. Lee, J.L. Stein, and D. Jung. Modelling and simulation of a dual-clutch transmission vehicle to analyse the effect of pump selection on fuel economy. *Vehicle System Dynamics*, 48(7):851 – 868, 2010.

[161] Rahul Ahlawat, Jonathan R. Hagena, Zoran S. Filipi, Jeffrey L. Stein, and Hosam K. Fathy. Volterra series estimation of transient soot emissions from a diesel engine. In *IEEE Vehicle Power and Propulsion Conference*, Lille, France, September 2010.

[162] Constantine D. Rakopoulos, Athanasios M. Dimaratos, Evangelos G. Giakoumis, and Dimitrios C. Rakopoulos. Investigating the emissions during acceleration of a turbocharged diesel engine operating with bio-diesel or n-butanol diesel fuel blends. *Energy*, 35(12):5173–5184, 2010.

[163] B. G. Dijkstra. *Iterative learning control, with applications to a wafer-stage.* Ph.D. Dissertation (Mechanical Engineering) Technische Universiteit Delft, 2004.

[164] M. Volckaert, A. Van Mulders, J. Schoukens, M. Diehl, and J. Swevers. Model based nonlinear iterative learning control: a constrained gauss-newton approach. In *17th IEEE Mediterranean Conference on Control and Automation*, pages 718–23, Thessaloniki, Greece, June 2009.

[165] D.H. Owens and J. Hätönen. Iterative learning control - an optimization paradigm. *Annual Reviews in Control*, 29(1):57 – 70, 2005.

[166] Sandipan Mishra, Ufuk Topcu, and Masayoshi Tomizuka. Optimization-based constrained iterative learning control. *IEEE Transactions on Control Systems Technology*, 2010.

[167] Kevin L. Moore. *Iterative learning control: An Expository Overview*. Applied and Computational Control, Signals and Circuits: Volume 1, Birkhäuser Boston, 1999.

[168] W. Hoffmann, K. Peterson, and A. G. Stefanopoulou. Iterative learning control for soft landing of electromechanical valve actuator in camless engines. *IEEE Transactions on Control Systems Technology*, 11(2):174–84, 03 2003.

[169] R. Horowitz. Learning control of robot manipulators. *Transactions of the ASME: Journal of Dynamic Systems, Measurement and Control*, 115(2):402–11, 06 1993.

[170] H. Havlicsek and A. Alleyne. Nonlinear control of an electrohydraulic injection molding machine via iterative adaptive learning. *IEEE/ASME Transactions on Mechatronics*, 4(3):312–23, 1999.

[171] Y. Fujii, W. E. Tobler, E. M. Clausing, T. W. Megli, and M. Haghgooie. Application of dynamic band brake model for enhanced drivetrain simulation. *Proceedings of the Institution of Mechanical Engineers, Part D: Journal of Automobile Engineering*, 216(11):873–881, 2002.

[172] Shushan Bai, Robert L. Moses, Todd Schanz, and Michael J. Gorman. Development of a new clutch-to-clutch shift control technology. In *SAE World Congress & Exhibition*, number 2002-01-1252, March 2002.

[173] K.V. Hebbale and Y.A. Ghoneim. A speed and acceleration estimation algorithm for powertrain control. In *Proceedings of the IEEE American Control Conference*, volume 1, pages 415 – 420, 1991.

[174] Quan Zheng. *Modeling and Control of Powertrains with Stepped Automatic Transmissions*. Doctoral Dissertation (Mechanical Engineering), The Ohio State University, 1999.

[175] C. M. Krishna and Kang G. Shin. *Real-time systems*. McGraw-Hill, 1997.

[176] M. Arnold, B. Burgermeister, and A. Eichberger. Linearly implicit time integration methods in real-time applications: DAEs and stiff ODEs. *Multibody System Dynamics*, 17(2-3):99–117, 04 2007.

[177] G. Rill. A modified implicit euler algorithm for solving vehicle dynamic equations. *Multibody System Dynamics*, 15(1):1–24, 02 2006.

[178] A. Schiela and F. Bornemann. Sparsing in real time simulation. *Zeitschrift fur Angewandte Mathematik und Mechanik*, 83(10):637 – 47, 2003.

[179] R. M. Howe. Real-time multi-rate asynchronous simulation with single and multiple processors. In *Enabling Technology for Simulation Science II*, volume 3369, pages 331–342, Orlando, FL, April 1998. SPIE.

[180] R. M. Howe. Real-time simulation of dynamic systems using a variable integration step size. In *Proceedings of the Simulation Multiconference on the International Simulators Conference*, March 1993.

[181] R.E. McFarland. *Stability of Discrete Integration Algorithms for a Real-time, Second-order System.* Technical Report, NASA Ames Research Center, 1997.

[182] T. D. Bui. Solving stiff differential equations for simulation. *Mathematics and Computers in Simulation*, 23(2):149–56, 07 1981.

[183] A. M. Schneider, J. A. Anuskiewicz, and I. S. Barghouti. Accuracy and stability of discrete-time filters generated by higher-order s-to-z mapping functions. *IEEE Transactions on Automatic Control*, 39(2):435–41, February 1994.

[184] A. M. Schneider, J. T. Kaneshige, and F. D. Groutage. Higher order s-to-z mapping functions and their application in digitizing continuous-time filters. *Proceedings of the IEEE*, 79(11):1661–74, November 1991.

[185] A. I. A. Karim. Stability of the fourth order runge-kutta method for the solution of systems of differential equations. *Computer journal*, 9(3):308–311, 11 1966.

[186] Peter Bunus. A simulation and decision framework for selection of numerical solvers in scientific computing. In *39th Annual Simulation Symposium*, Apr 2-6 2006.

[187] G. R. Harting. Design and application of heavy-duty clutches. *The Ninth L.Ray Buckendale Lecture, SAE Transactions*, (SP-239):405–432, 1963.

[188] T. Minowa, T. Ochi, H. Kuroiwa, and K. Liu. Smooth gear shift control technology for clutch-to-clutch shifting. In *SAE World Congress & Exhibition*, number 1999-01-1054, Detroit, MI, March 1999.

[189] Heon-Sul Jeong and Kyo-Ill Lee. Shift characteristics analysis and smooth shift for an automatic power transmission. *Journal of Mechanical Science and Technology*, 14:499–507, 2000.

[190] H. K. Fathy, Z. S. Filipi, J. Hagena, and J. L. Stein. Review of hardware-in-the-loop simulation and its prospects in the automotive area. In *Modeling and Simulation for Military Applications*, volume 6228, pages 62280–1, April 2006.

[191] B. Ninness and G.C. Goodwins. Estimation of model quality. *Automatica*, 31(12):1771 – 97, 1995.

[192] D. Hrovat and W.E. Tobler. Bond graph modeling and computer simulation of automotive torque convertors. *Journal of the Franklin Institute*, 319(1-2):93 – 114, 1985.

[193] Rahul Ahlawat, Shugang Jiang, Dharshan Medonza, James Kitchen, and Michael H. Smith. Engine torque pulse and wheel slip emulation for transmission-in-the-loop experiments. In IEEE/ASME *International Conference on Advanced Intelligent Mechatronics*, pages 688 – 695, Montreal, QC, Canada, 2010.

[194] Wei Liang, J. Medanic, and R. Ruhl. Analytical dynamic tire model. *Vehicle System Dynamics*, 46(3):197–227, 03 2008.

[195] Carlos Canudas de Wit, Panagiotis Tsiotras, Efstathios Velenis, Michel Basset, and Gerard Gissinger. Dynamic friction models for road/tire longitudinal interaction. *Vehicle System Dynamics*, 39(3):189–226, 2003.

[196] J. Y. Wong. *Theory of ground vehicles*. Wiley-Interscience, 2001.

[197] Jim E. Bernard and Chris L. Clover. Tire modeling for low-speed and high-speed calculations. In *SAE International Congress & Exposition*, number 950311, February 1995.

[198] C. L. Clover and J. E. Bernard. Longitudinal tire dynamics. *Vehicle System Dynamics*, 29(4):231–259, 1998.